CHARACTERIZATION AND MEASUREMENTS OF ADVANCED VERTICALLY ALIGNED CARBON NANOTUBE BASED THERMAL INTERFACE MATERIALS

A Thesis
Presented to
the Academic Faculty

by

Andrew McNamara

In Partial Fulfillment
of the Requirements for the Degree of
Doctor of Philosophy in the
George W. Woodruff School of Mechanical Engineering

Georgia Institute of Technology
December 2013

CHARACTERIZATION AND MEASUREMENTS OF ADVANCED VERTICALLY ALIGNED CARBON NANOTUBE BASED THERMAL INTERFACE MATERIALS

Approved by:

Dr. Yogendra Joshi, Advisor
School of Mechanical School
Georgia Institute of Technology

Dr. Zhuomin Zhang, Advisor
School of Mechanical School
Georgia Institute of Technology

Dr. Baratunde Cola
School of Mechanical School
Georgia Institute of Technology

Dr. Zhiqun Lin
School of Material Science and Engineering
Georgia Institute of Technology

Dr. Satish Kumar
School of Material Science and Engineering
Georgia Institute of Technology

Dr. Matthew Yao
GE Energy

Date Approved: November 15, 2013

To

My Loving Parents, Bernard and Brenda McNamara

and Brother Ryan

ACKNOWLEDGMENTS

First and foremost I like to thank my advisors, Dr. Zhuomin M. Zhang and Dr. Yogendra Joshi who have guided me through my work and have trained me to be capable of performing successful independent research.

I would also like to thank my PhD reading committee, Dr. Baratunde Cola, Drs. Satish Kumar and Zhiqun Lin of the School of Material Science and Engineering and Dr. Matthew Yao of GE Energy for their valuable participation and input in reviewing the proposal and dissertation.

I would also like to acknowledge the Defense Advanced Research Projects Agency for providing financial support for this work. Furthermore feedback and equipment provided by Dr. Suresh Sitaraman's and his group members Mr. Kevin Klein and Mr. Nick Ginga have been particular helpful. Also the assistance of technical staff of Rockwell Collins in Cedar Rapids Iowa for providing practical insight into advanced material needs as well providing materials needed for the completion of this work. I would in particular like to express my appreciation to Dr. C.P. Wong's group in the School of Material Science and Engineering, Dr. Jack Moon, Dr. Yagang Yao, Dr. Wei Lin, and Mr. Ziyin Lin for providing CNT samples used to complete this work and their daily valuable discussions whom without this work could not be completed.

I will also like to note my appreciation for the group members of Microelectronics and Emerging Technology Thermal Laboratory, and Multiscale Integrated Thermofluidics Laboratory for their suggestions and feedback on my work, and for training me on various equipments which I used for fabrication and measurements. I

would also like to express my gratitude to members of the Micro/Nanoscale Thermal Radiation group for their discussion and more importantly friendship during my studies.

I would in particular like to express my gratitude to my family, Bernard, Brenda and Ryan McNamara for their continued encouragement and support. Also I would like to acknowledge members of the Embry Hills Church of Christ who have assisted greatly in my spiritual growth and have been very kind during my studies.

TABLE OF CONTENTS

Page

LIST OF SYMBOLS AND ABBREVIATIONS

A	Cross-sectional area
a	Effective interface thermal resistance
B	Depolarization factor
b	Basal plane direction
C	Specific heat
$\vec{C}$	Chiral vector
c_0	Speed of light
D	Density of states
d	Diameter of the tube
E	Young's modulus
f	Bose Einstein distribution function
g_T	Quantum thermal conductance
G_{ep}	Electron-phonon coupling rate
H	Internal intensity
h	Thermal conductance
$\hbar$	Reduced Planck's constant
IR	Infrared
J	Sensitivity coefficient matrix
k	Thermal conductivity
k_B	Boltzmann constant
l	Length of nanotube

L	Length of layer
M	Molar mass
N	Number of allowed mode
N_1	product of the density of states of free electrons the Fermi-Dirac distribution function
n	Number of layers
n_e	Number density
p	Aspect ratio
p	Set of parameters
q	Wavevector
q''	Heat flux
Q	Heat rate
R	Ideal gas constant
R''_{tot}	Total thermal resistance across interface (per unit area)
R''_{C}	Contact resistance (per unit area)
R''_{d}	Diffusive constriction resistance resistance (per unit area)
t	Thickness
T	Temperature
$\mathbf{T}$	Measured temperature matrix
V	Volume
v	Velocity
$\mathbf{Y}$	Model temperature matrix

Subscripts

1	Medium 1
2	Medium 2
a	Average
c	Cross-section
e	Electron contribution
eff	Effective
F	Fermi
f	Filler
g	Group
hm	Harmonic mean
High	High temperature side
Low	Low temperature side
m	Matrix
sub	Substrate
t	Target
tot	Total

Greek Symbols

α	Thermal diffusivity
α_{12}	Phonon transmissivity between mediums 1 and 2
δ	Interlayer spacing
ε	Emittance

Λ	Mean free path
λ	Eigenvalue
ρ	Density
τ	Relaxation time
μ	Damping parameter
μ_F	Fermi Velocity
θ	Time variable
ω	Angular velocity
φ	Filler volume fraction
Ω	Solid angle

Abbreviations

AFM	Atomic force microscope
AMM	Acoustic mismatch model
ASTM	American Society for Testing and Materials
CNT	Carbon nanotube
CTE	Coefficient of thermal expansion
CVD	Chemical vapor deposition
DMM	Diffuse mismatch model
MD	Molecular dynamics
MWCNT	Multiwall carbon nanotube
NREL	National Renewable Energy Laboratory
PA	Photoacoustic
PCM	Phase change material

TCA	Thermal conductive adhesive
TIM	Thermal interface material
SEM	Scanning electron microscope
SWCNT	Single-Wall carbon nanotube
VACNT	Vertically aligned carbon nanotube

LIST OF TABLES

Page

LIST OF FIGURES

SUMMARY

A significant portion of the thermal resistance of an electronic package is due to the thermal interface material (TIM) used to join different materials. With continued demands of device's performance and size, improvements of TIM selection and characterization are of increased importance. Due to the reported high axial thermal conductivity and robust mechanical properties, CNTs have attracted much attention as future TIMs. Due to their high processing temperatures (over 700 ^{o}C), transfer of the CNT array to a separate processed substrate has been of interest. The thesis focuses on the characterization and analysis of novel TIMs based on vertically aligned multiwall carbon nanotubes.

The first part of the thesis describes the development of a microscopic infrared (IR) steady-state measurement of the total TIM thermal resistance. The technique is demonstrated to be effective in evaluation of commercial TIMs and is extended to the measurement of CNT-based TIM. Measurements are compared to measurements made through a laser flash technique. The performance of these materials after additional thermal reliability is also examined.

The second part of the thesis theoretically analyzes the role of different interface structures for CNT based TIM, with particular emphasis on a metal based thermal conductive adhesive used to anchor a CNT array to an active die. A control volume approach which includes intrinsic thermal conductivity of the components and boundary thermal resistances expected in anchoring of the array is used to estimate the lowest potential thermal resistance through a parametric study. The results are then compared to the VACNT TIM measurements made through the steady-state IR measurement.

Finally, a novel transient IR imaging technique is demonstrated for experimentally evaluating the thermophysical properties of a multilayer sample. This

transient technique can provide additional insight into the individual thermal resistances which contribute to the total resistance, as measured through the steady-state IR technique and thus can be used as an effective tool in the characterization of TIMs. Future studies regarding further development and improvement of this method are outlined for its potential application in measuring next generation TIMs.

CHAPTER 1

INTRODUCTION

One of the major issues for thermal management of semiconductor devices is the excessive thermal resistance between two dissimilar materials due to contact resistance, primarily related to surface roughness. To lessen the contact resistance, thermal interface materials (TIMs) are used to fill in the gaps within the chip package. For most high performance chip packages, TIMs are used between an active die and heat spreader and between a heat spreader and a heat sink as shown in Fig 1.1. According to the International Technology Roadmap for Semiconductors the large thermal resistance of current interface materials not only limits performance and reliability of the device, due to excessive junction temperatures, but also affects the chip packaging density which contributes to longer interconnect wire lengths leading to lower bandwidth and higher interconnect losses.[1] Current state-of-the-art TIM materials have

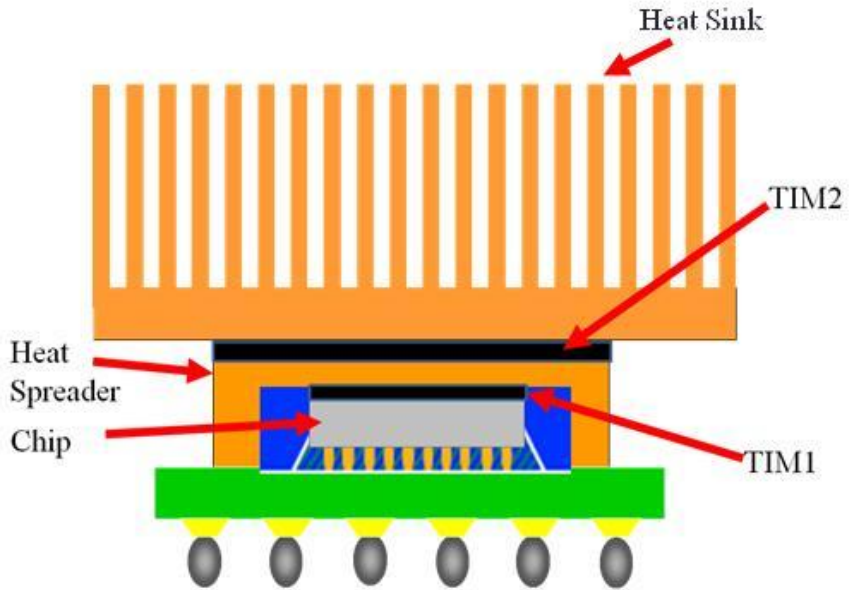

Figure 1.1 Microelectronic chip packages with 2 TIM layers between chip and heat spreader and heat spreader and heat sink.

produced thermal resistances in the range $5-10\,\mathrm{mm^2\ K\ W^{-1}}$.[2] Continuing research efforts aim at reducing the thermal interface resistances through improved conductive materials including nano-fillers into current thermal adhesives, phase change materials and carbon nanotubes.[3]

Due to the high reported thermal axial conductivity, k, both measured and simulated, the inclusions of CNT fillers for TIM have garnered significant attention. However, for randomly dispersed CNT in a polymer matrix, the thermal enhancement has been lower than expected though effective medium approximations. This is a result of not all tubes fully participating in thermal conduction and contact thermal resistance between neighboring tubes [4] and/or resistance with the matrix material.[5] Furthermore, the use of vertically aligned carbon nanotubes arrays (VACNT) have received attention, not only due to high k, but also their ability to mechanically comply to materials which have different coefficients of thermal expansion, CTE, in a device package.

The primary objective of this thesis is to describe the theoretical and experimental investigation the use of vertically aligned carbon nanotubes (VACNT) arrays as next generation interface materials. This will be done by describing the roles of different interface structures for use with aligned CNT arrays with particular emphasis on a metal based thermal conductive adhesive (TCA) used to anchor a VACNT array to a separate substrate. This unique contribution will assist in the future design of VACNT based thermal interface materials. This study will further include the description of a steady-state infrared (IR) measurement technique capable of measuring the cross plane total thermal resistance per unit area, R''_{tot}. Furthermore the thesis will describe the development of a novel measurement system which will characterize the thermal properties of multilayer samples using IR imaging. Based on solution for a transient 1-D nonhomogeneous multilayer problem the relevant thermal properties of the material can be determined. Two different transient IR measurement techniques, including the use of a

high-speed IR detector and full thermal mapping movie mode, will be described and compared in the development of this metrology process.

This thesis is organized as follows: an extensive literature review is provided in Chapter 2 to describe modern commercially available TIM, potential TIM components including CNT arrays and state-of-the-art metrology techniques to characterize thermal properties of TIM. Chapter 3 describes the development of a steady-state IR microscopy technique and its use in characterizing VACNT-based TIM. Results are presented for VACNT TIM anchored using TCA and solder attachments. Chapter 4 describes a steady-state numerical model used to analyze the total thermal resistance of a TCA anchored VACNT TIM demonstrating its promise as a future TIM candidate. Chapter 5 presents a novel transient IR imaging technique for use in characterizing the thermal properties of multilayer materials through the use of a high-speed detector and a lower-speed movie mode. Finally, Chapter 6 summarizes the major findings and discusses the impact of this thesis. Future studies are also outlined in Chapter 6, particularly on methods to improve the transient IR technique for use in the characterization of the next generation TIMs.

CHAPTER 2

LITERATURE REVIEW

With increasing power densities in many modern microdevices and microprocessor packages attention has been given to improved methods of heat removal. One area of interest in thermal packaging is advanced TIMs used to join materials in the overall heat flow path. Commercially available TIMs include greases, solders, and phase change materials (PCMs). Each of these materials has associated advantages and disadvantages depending on the application as described in Table 2.1.[2, 6] Micro and nanoscale research is enabling new nanostructured materials, which can be used either in conjunction with modern TIMs, or as stand-alone materials which possess improved thermal and mechanical properties. These materials include nanoparticle laden TIMs, dispersed CNTs in a polymer matrix, and VACNT arrays.[2, 3, 7, 8] Detailed modeling of properties of nanostructured TIMs have been made through various analytical models and computational simulations in addition to characterization through different experimental techniques. Potential improvements, including mechanical and thermal properties, in TIM materials been demonstrated.

Arrays of VACNT as TIMs have been of particular interest, due to the high intrinsic *k* of the nanotubes along the axial direction. The k of single multi-walled CNTs (MWCNTs) has been reported experimentally to be near at $3,000\ \mathrm{W\,m^{-1}\,K^{-1}}$ at room temperature.[9] However, when employed in VACNT array structures, the observed effective conductivity has been much lower.[10] Furthermore interface resistances between the arrays and mating substrates remains a significant barrier to future use. Additionally, due to high growth temperature associated with CNT synthesis ($> 750\ ^{o}\mathrm{C}$) it is evident that such a process would not be compatible with processed CMOS dies.

Table 2.1 Commercial TIM Materials [2]

TIM Type	R''_{tot} mm^2 K W^{-1}	General Description	Advantages	Disadvantages
Greases	~ 10	Silicone matrix loaded with particles to enhance *k*	Thin BLT, Low viscosity, No curing required, No delamination	Grease pump out, Messy
PCM	~ 10	Polyolefin, epoxies	Less susceptible to pump-out, easy to handle	Lower k, requires attachment pressure
Adhesives	< 10	Ag particles in cured matrix	No pump out, conform to surface before curing	Need to cure, Delamination, High CTE
Solder	< 5	Metallic Alloys	high *k*	Void formation, low melting points

The following will describe the emerging materials used in TIM with particular emphasis into CNT analysis. Also different measurement techniques which have been used to characterize the thermal properties of TIM will be discussed. The various benefits and drawbacks of the methods will be presented.

2.1 Emerging TIMs for Microsystems

Several materials which have been studied and have shown promise as potential candidates for future TIMs for microelectronics and other systems. Current TCAs use randomly dispersed metals or ceramic powders including silver, alumina, and boron nitride. These additives are used to improve not only the effective thermal conductivity of the composite material, k_{eff} , but also the mechanical stability of the package. Nanocomposite TIMs can be described as materials consisting of embedded nanoparticles in a matrix material. Generally, for the same type of filler particles, larger average additive sizes lead to higher k_{eff} , for a fixed volume fraction.[11, 12] Alternatively,

through the infusion of nanoparticles, there is a greater likelihood of a fully percolating network for heat flow, thereby increasing k_{eff} .[12, 13] Figure 2.1 demonstrates the concept of percolation using a hybrid nanostructured TIM with a combination of larger and nano-sized fillers. Table 2.2 describes recent measurements of nanoparticle laden TIM in the literature. The observed enhancement is given as the ratio of the k_{eff} vs. the matrix thermal conductivity, k_{m} . As seen the higher k_{eff} can be observed with the hybrid type fillers.

Since their introduction in 1991, CNTs have received considerable interest in research for their electrical, mechanical, and thermal properties, making them candidates for numerous applications.[17] CNTs are hollow cylindrical structures which possess a high length to diameter ratio, up to 10^7.[18] CNT can generally be grouped as either single-wall (SWCNTs) or multiwall (MWCNT). A SWCNT has only one ring of carbon

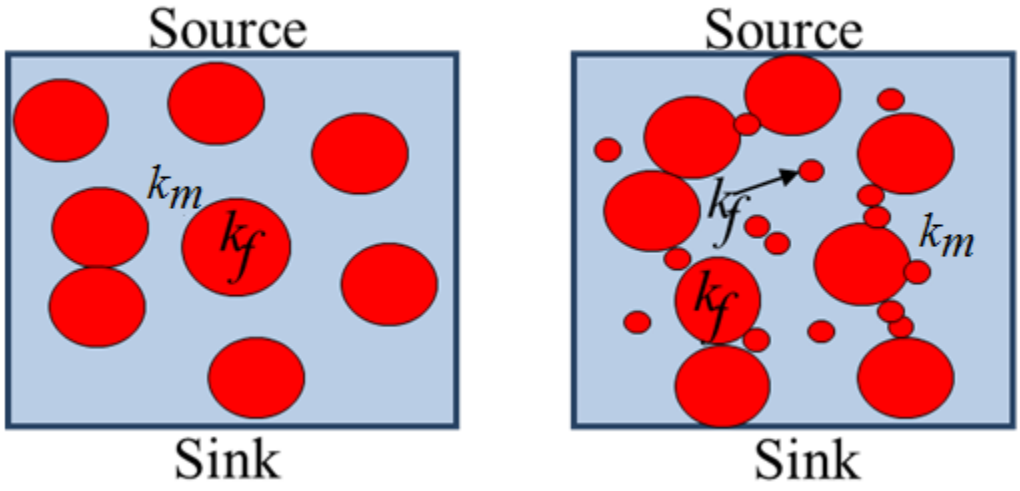

(a) (b)

Figure. 2.1 Percolation network through inclusion of nanoparticles (a) Large agglomerations fail to produce fully conducting network from source to sink (b) Inclusion of nano-filler completes network thereby increasing effective thermal conductivity of the matrix.

Table 2.2 Nanoparticle Laden TIM

Material	Matrix	Concentration	Avg. Particle Size	Technique	Observed Enhancement k_{eff}/k_m	Source
Al_2O_3	PMMA	10 wt %	60 nm	3ω	1.05	[14]
AlN	Epoxy	10 wt %	60 nm	Steady-state	1.18	[15]
BN	Epoxy	10 wt %	<100 nm	Steady-state	1.14	[15]
BN	Silicone Rubber	60 vol%	300 nm	Laser Flash	6.1	[13]
BN	Silicone Rubber	40 vol%	Mixed	Laser Flash	7.41	[13]
BN	Epoxy	22 vol %	70 nm	Laser Flash	1.8	[12]
BN	Epoxy	22 vol%	Mixed	Laser Flash	3.5	[12]
BN	Epoxy	-	50-400 nm	Steady-state	0.88 $W\ m^{-1}\ K^{-1}$	[16]

atoms. A MWCNT, is composed of multiple carbon atom rings and can have diameters ranging from 2-30 nm depending on the total number of tube walls. The structure of SWCNTs can be described by their chiral vector, $\vec{C}$ [19]

$$\vec{C} = ma_1 + na_2 \tag{2.1}$$

where m and n describe the chiral indices and a_1, a_2 are the CNT basis vectors. Different SWCNTs (either metallic or semiconducting) are based on their rolling along the $\vec{C}$.[20]

A significant portion of the early research work done regarding CNTs were on their mechanical behavior. The first experimental report of the measurements of the Young's Modulus (*E*) of MWCNT was by Treacy.[21] The elastic modulus was determined by embedding MWCNTs into an amorphous material at one end and the leaving the other end in free space. A thermally induced load was used to oscillate the tip and the deflection was monitored by transmission electron microscopy. The nanotubes measured *E* of 1.8 TPa. In comparison *E* for steel is up to 200 GPa. Similar values have also been reported for SWCNT [22] and MWCNT [23] Furthermore analysis into the

breaking stress and strain under tensile loading was done by Yu *et al.* between opposing atomic force microscope (AFM) tips.[24] The E measured for the individual MWCNT ranged from 270 to 350 GPa with breaking strains between 3% to 12 % and strength from 11 to 63 GPa.

For thermal interface material (TIM) applications as described here optimal materials possess a large k, and a low E which helps accommodate materials with mismatched coefficients of thermal expansion between heat sources and sink. Polymers generally have a low E but also a low k. Solder materials typically have a high k but are not generally mechanically compliant and can lead to long term reliability issues. However, due to their large aspect ratio, and packaging density, nanotubes used in arrays can be quite flexible with in-plane E values between 10-500 MPa, as measured by a microfabricated resonator.[25] This is lower than that of polymer by at least an order of magnitude, and lower than metals by several order of magnitude. Ginga *et al.*. [26] also showed through nano-indentation tests that effective compressive modulus for the nanotube array can be an order of magnitude lower than those reported for individual CNT.

In addition to desirable mechanical compliance characteristics, CNTs also have a k which reportedly exceeds that of diamond ($2,000\ \mathrm{W\,m^{-1}\,K^{-1}}$).[27] For non metallic solids, in which the thermal conduction is dominated by phonon conduction, from kinetic theory the k is a function of the heat capacity per unit volume, ρC (where ρ is the density and C is the specific heat), the speed of sound, v_a, and the mean free path, Λ .[19] The mean free path is related to the relaxation time by $\Lambda = v_a \tau$ where τ is the scattering rate. In the relaxation time approximation, the various scattering terms which account for τ are additive; these scattering events include events from boundaries, defects, and interactions with other phonons which take place at high temperatures (Umklapp scattering). Estimates of the range of room temperature Λ are between 50 nm

to 1.5 μm.[28, 29] Due to strong sp^2 bonding between the atoms, the acoustic speed of the phonons in CNT is expected to be high.[30] These then contribute to an expectedly high intrinsic k. At low temperature the four acoustic branches, two transverse modes, one longitudinal mode, and one torsional mode are expected to be dominate thermal transport for SWCNT.[31] The dispersion relation for all four modes is linear at low temperature leading to a linear C [19]. Mingo and Broido [32] showed that at low temperature the quantum thermal conductance, g_q, for a SWCNT can be given as

$$g_q = \frac{8\pi^2 k_B^2 T}{3\hbar} \tag{2.1}$$

where k_B is the Boltzmann constant, $\hbar$ is the reduced Planck's constant and the factor of 8 is due to the four active phonon branches. The thermal conductivity is then related to this conductance through $g = kA_c / L$ where A_c is the nanotube cross-sectional area and L is its length. At higher temperatures more phonons are active and more 2D characteristics for the g are observed.

Depending on the chirality of the tube, as previously discussed, the tube can be either semiconducting or metallic. For semiconducting SWCNT, the electron contribution is negligible due to the large electron bandgap.[33] For a mat of conducting SWCNT, Hone *et al.* independently measured the temperature dependent conductance and electrical conductivity.[29] The measured ratio was two orders of magnitude larger than the Lorentz number over a range of 30 K to 350 K. This would mean for a conducting mat the primary source of thermal transport is from phonon vibration rather than electrons.

Unlike SWCNT, MWCNT with a larger diameter cannot be considered as purely 1-D phonon systems due to weak van der Walls interwall interactions. Kim measured g of an MWCNT with a diameter of 14 nm and length 2.5 μm with a test fixture shown in Fig 2.2(a).[9] In the measurement, heat was conducted from one electrode through the

tube and is sensed by the opposing electrode which was used to determine the k of the tube.[9] Accompanying scanning electron microscopy (SEM) and atomic force microscopy (AFM) measurements were used to determine the diameter of the tubes. In the low temperature range, g increased at $T^{2.5}$ which is different from the linear behavior with temperature for SWCNT as described by Eqn. (2.1). Over an intermediate temperature range from $T = 50$ K to $T = 150$ K the k increased as T^2. Above 150 K, g increased and reached a maximum near 320 K, which is over $k = 3{,}000$ W m^{-1} K^{-1}. Beyond this temperature, g decreased due to an increase of Umklapp scattering. At low temperature, this scattering is negligible and the temperature dependence of the *k* follows that of C. An issue with measurement is the isolation of the tube g measurement from the interfacial resistances of the tube and the heating elements.

Through assuming the bulk dispersion relations of graphite, which permitted for interlayer coupling between tube layers, Prasher modeled the k of MWCNT observed in the early experiments of Kim through a combination of diffusive and ballistic thermal transport since the size of the tube was on the same order as the predicted mean free path.[34] The MWCNT k as modeled as graphite fibers was given as

$$k = \frac{\Lambda}{(2\pi)^3} \sum_j \int_0^{q_{b,\max}} \int_0^{q_{z,\max}} \hbar\omega \frac{df}{dT} v_{g,b} q_b dq_b dq_z \tag{2.2}$$

where ω is the angular velocity, f is the Bose Einstein distribution function, q is the wavevector, and $v_{g,b}$ is the phonon group velocity in the basal plane, $v_{g,b} = \partial\omega / q_b$, and the subscript *z* indicates the c-axis. Figure 2.2b shows the comparison between the experimental data and the prediction of Prasher demonstrating the estimate of semiballistic thermal transport was appropriate compared to the ballistic and diffusive regimes solely. Despite the loose coupling of layers compared to the strong coupling in the plane, the *k* perpendicular to the tube axis is expected to be orders of magnitude

lower as is the case in graphite. This leads to the multiwall CNTs being near ideal 1-D thermal conductors along the tube axis.

Widely quoted values for individual CNTs k are $\sim 3{,}000\ \mathrm{W\,m^{-1}\,K^{-1}}$ for MWCNTs as previously discussed and $\sim 3{,}500\ \mathrm{W\,m^{-1}\,K^{-1}}$ for SWCNTs at room temperature. [9, 36, 37] Both SWCNT and MWCNT have had g measurements made through suspended MEMS devices in which platinum electrodes are patterned between two membranes as seen in Fig. 2.2a. SWCNT measurements have also been made through applying a bias voltage to the tube and determining the thermal profile and k as a result of Joule heating. [37] Additional measurement through 3ω technique, which will be described as a TIM metrology technique, have resulted in a range of k for MWCNT and SWCNT of $300-3{,}200\ \mathrm{W\,m^{-1}\,K^{-1}}$.[28, 38, 39]

From these theoretical and measured thermal conductivities for SWCNT and MWCNT it is noted that their intrinsic thermal resistance due to tubes would be expectedly low. One of the significant factors to their implementation in devices currently is interfacial resistance between the tube and the opposing interface. This thermal resistance, as will be discussed, is primarily attributed to ballistic resistance due to the mismatch of acoustic properties between the substrate and CNT. A majority of the research in this area has been done through molecular dynamic (MD) simulations. Shenogin *et al.* [5] studied interfacial resistance between CNT and an organic fluid. The interfacial resistance resulted in an equivalent resistance of nearly 15 nm thick layer of the organic fluid, explaining why significant enhancement of randomly dispersed CNT in a matrix, as will be discussed, has not resulted in a significant increase in the k_{eff}. Other models have considered the end contacts of the CNT and different substrates. Diao *et al.* [40] modeled the interface between a CNT and silicon indicating that the thermal conductance can be increased through increased attachment pressure through larger

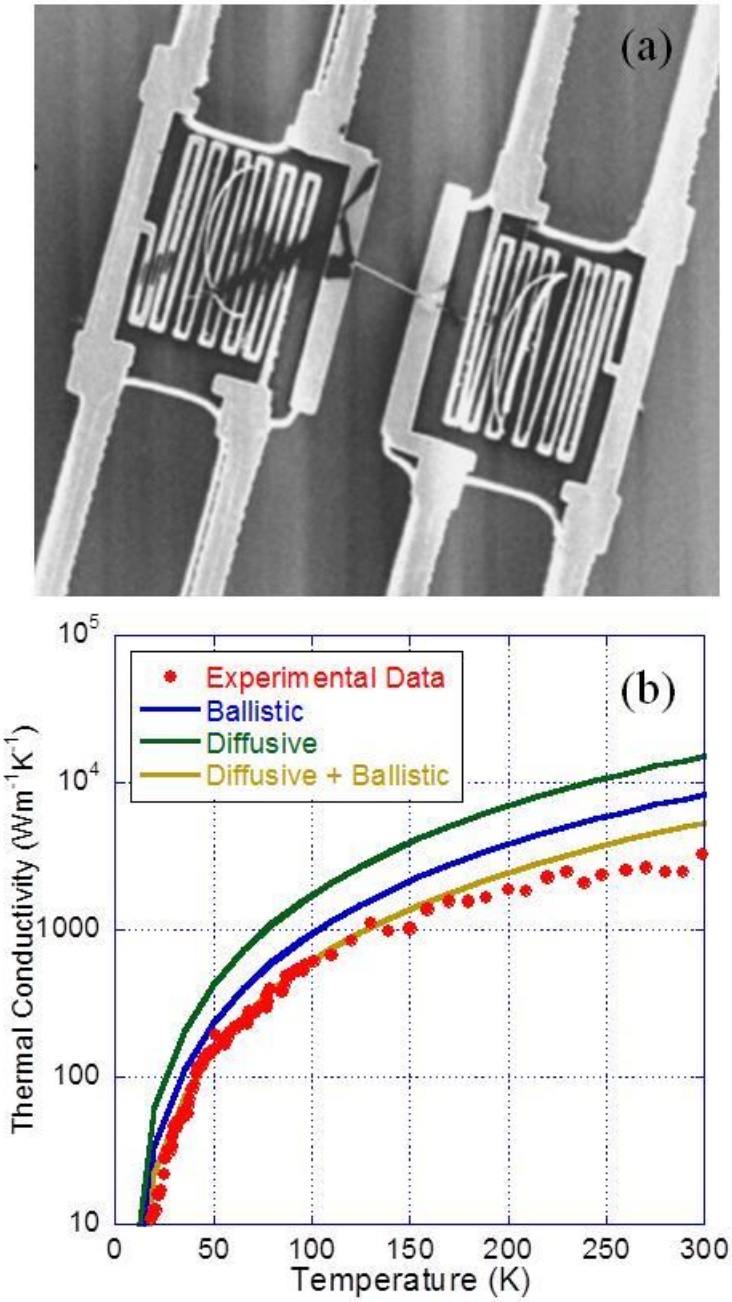

Figure 2.2. (a) Experimental bridge test structure for determining thermal conductivity of CNT [9] (b) Combined ballistic and diffusive theoretical modeling of MWCNT thermal conductivity [9, 35]

contact areas. Gao *et al*. [41] described the interfacial transport between a metallic CNTs and a metal substrate, demonstrating that electron-phonon coupling within the metal should be considered in the evaluation of interfacial resistance. These models can be used

as guides for future fabrication of CNT based TIMs and provide further insight into other experimental research.

2.2 Fabrication of CNT

Since their development, several different methods for CNT synthesis have been used. CNT synthesis techniques include arc-discharge, laser ablation, and various chemical vapor deposition (CVD) techniques. Arc discharge and laser ablation were the early methods used to produce CNT.[42-44] Both involve condensation of hot gases of carbon atoms generation from evaporation of solid carbon. With these methods disordered carbon nanotube entanglements are possible. CVD is typically preferred due to improved control over CNT length, diameter, alignment, and adhesion to the growth substrate. This method involves the decomposition of a gas containing carbon, catalyzed by metallic nanoparticles which serve as CNT nucleation sites to be initiated.[45] The method is the most widely used for commercial production.

There are still several issues associated with large scale production of CNT for use as TIM. These include high costs associated with larger scale processes, selective production including tailoring the structure of the CNTs and their corresponding thermal and electrical properties, organization of the CNTs including control over alignment, and also a complete knowledge of their growth mechanism.

2.3 CNT as TIM

Early work using CNTs includes dispersing them randomly in a matrix material, forming a percolating network, which increased heat flow similar to nanoparticle laden TIMs. Typically, the k of the base polymer ($\sim 0.2\ \mathrm{W\,m^{-1}\,K^{-1}}$) is orders of magnitude lower than the expected value for the nanotubes. The challenge is to enhance the k of the matrix by adding CNT at a low loading level. Biercuk *et al.*. [46] showed through electrical transport measurement that a percolating network of a randomly dispersed CNT

composite material was formed at a volume fraction, φ of 0.2%. For filler concentrations greater than the percolation threshold, Huxtable *et al.* [47] gave a relation for k_{eff} of a composite comprised of randomly oriented fillers as

$$k_{\text{eff}} = k_f \varphi / 3 \tag{2.4}$$

From Eqn. (2.4), at φ as low as 1% the k_{eff} of the composite should be near $10\ \text{W m}^{-1}\ \text{K}^{-1}$. However, only moderate increases in k_{eff} was noted in literature, far below this expected 50-times the base material. Two explanations for this discrepancy are that since the CNTs are randomly dispersed, not all tubes effectively participate in heat conduction and that at low φ, CNTs rarely form a connected path for heat flow since there are discontinuities either at the boundaries of the tube and base material, or through contact with adjacent CNT. Also, between the CNT and the polymer there can exist a thermal boundary resistance across the CNT-polymer interface due to acoustic mismatch between the two materials. Furthermore, if the nanotubes are in contact, the contacting area may be small leading to increased thermal resistance.

Improved methods of dispersing the CNTs involve better alignment along the heat flow path. Choi *et al.*. [48] noted an increase of 10% above the original composite conductivity by aligning the nanotubes in a magnetic field. Marconnet *et al.*. [49] analyzed the k_{eff} enhancement for nanotubes which were axially aligned and transversely aligned arrays in the direction of heat flow. The axially aligned tubes demonstrated increasing conductivity with increased packing density, while the transversely aligned arrays exhibited little enhancement over the base matrix. Additionally aligned nanotubes, in an epoxy matrix, were functionalized and microwave treated and exhibited a higher effective conductivity than similarly aligned CNT which were thermally cured.[50] It was suggested that microwave treating the composite resulted in increased chemical bonding, thereby leading to increased phonon transport.

VACNT arrays have recently received much attention as potential stand-alone TIM due to their high intrinsic k in the axial direction. Compared to randomly dispersed CNTs in polymer matrices, several early experimental results have shown that the VACNTs compare favorably to other modern TIMs. The mechanical compliance of CNTs has been of particular interest since elements of device package have different CTE, which may eventually lead to delamination of other TIMs, causing overheating and device failure. Since the CNTs have high intrinsic k, the primary source of thermal resistance is the boundary resistance at the free ends of the tubes. Cola *et al.*, showed that for single-sided VACNT arrays and for opposing VACNT arrays in intimate contact by increasing attachment pressure the contact area at the free ends of the VACNT was increased through bending of the tubes. This has the effect of decreasing the overall thermal resistance.[51] Furthermore, decreasing boundary resistance through various anchoring materials at CNT ends has been attempted, as described below.

Most previous research has focused on single-sided VACNT interfaces by maintaining the growth substrate for measurement purposes. Additional research has been ongoing into double-sided CNT interfaces, or removing the grown CNT from the native substrate and then affixing it to a new substrate through various anchoring techniques. The removal of the VACNT, and its subsequent stand alone use as a TIM has been examined, since the processing temperatures for VACNT synthesis are typically not compatible with integrated circuit fabrication. Lin *et al.* [52] examined a means of chemically transferring a CNT array. The method involved functionalizing the VACNT with reactive groups during the CVD process, and then covalently bonding the tubes to a separate monolayer. Apparent issues with this process included thermal instability of the TIM and weak adhesion to a silicon substrate. An improved approach described as "molecular phonon coupling" was used to improve phonon transport across the Si-VACNT interface. [52, 53] An inorganic solution was spin coated on top of a silicon substrate and was then adhered to a VACNT array grown on a copper substrate and

microwave treated. This newly formed TIM demonstrated an order of magnitude improvement in thermal conductance, as compared to a pressure contact TIM comprised of a similar VACNT array. Cross *et al.*. [54] demonstrated that the CNT adhesion to the growth substrate could be reduced by introducing water vapor during processing to etch the ends of the tubes as well as the CNT/catalyst interface. In addition, they explored the potential of metalizing the CNT ends with a material similar to that of the opposing substrate to decrease boundary resistance. Figure 2.6 shows some of the recent approaches for implementing a CNT array TIM to join a silicon chip to a metal heat spreader.

Table 2.3 describes results for aligned CNT. As a point of reference, many state-of-the-art TIM materials have R''_{tot} values between $8-10\,mm^2\,K\,W^{-1}$. It is notable that the reported VACNT TIM R''_{tot} values vary greatly in the literature. Performance can be dictated by many factors including array height, density and adhesion to the growth substrates. A deeper understanding of how interface materials affect conduction pathways and being able to better quantify actual CNT contact with the substrates are critical in improving performance of VACNT TIM . Both references [54, 55] have metalized CNT free ends with low R''_{tot} values, thereby demonstrating promise of using this technique.

The modeling of the VACNT TIM has been generally broken into three resistances. These include the resistance at the growth surface or separate mating substrate with the CNT array, the resistance of the free end of the CNT and the opposing surface, and finally the intrinsic resistance of the CNT array. Prasher [58] identified the resistance at the two ends, and their respective substrates as the sum of the ballistic

Table 2.3 Thermal resistance of VACNT Based TIM

Material	CNT Diameter nm	Array Height μm	Technique	Resistance $mm^2\ K\ W^{-1}$	Source
Si-CNT-Ag-Si	15-60	15 on Si	Photoacoustic	15.8	[56]
Si-CNT-CNT-Cu	15-60	20 on Cu	Photoacoustic	4.1	[56]
Si-CNT-Cu	20	10	Steady-state	19.8-31	[7]
Si-CNT-Ni	100	30	Photothermal	12	[57]
Si–CNT–Ag	16-40	-	Photoacoustic	8	[43]
Glass-In-CNT-Si	20-30	100	Thermoreflectance	~1	[24]
Glass-CNT-Si	10-80	13	3ω	74-83[1] $W\ m^{-1}\ K^{-1}$	[6]
Si-CNT-Ti/Au-Ag	18	30	Photoacoustic	1.7-4.5	[20]
Si-CNT-TIM-Ag	20	15-60	Photoacoustic	2.5	[56]

[1]Measured VACNT array thermal conductivity

resistance and a constriction resistance. Analytical expressions for the classical constriction conductance due a VACNT in contact with a substrate are can be found in [51]. Several models have been developed in order to effectively evaluate the ballistic resistance. Many are based on the diffuse mismatch model (DMM).[60] This model assumes that all incident phonons scatter both diffusely and elastically at the interface between two contacting materials. Applying a DMM approach, Prasher [34] made analytical calculations of the thermal conductance, between MWCNT and Platinum contacts both in horizontal and vertical orientations. Additional analytical modeling using DMM of an anisotropic material has been used to evaluate the interfacial resistance between graphite and metal [60]. Recently, near room temperature experiments of Panzer *et al.*. [61] suggested that inelastic phonon scattering may occur at the interface between SWCNT and metals. This model showed improved agreement with experimental data for an Al-graphite interface at 300 K than a two phonon elastic model. [63].

In *ab initio* models, the motions of atoms are governed by their interatomic potentials with neighboring atoms. Molecular dynamics (MDs) simulations of SWNT by Che and Berber [64, 65] place the *k* of a SWNT as high as 3,000-6,600 $W\ m^{-1}\ K^{-1}$ at room temperature, The high *k* is attributed to the large phonon mean free path of SWNT, on the order of a micrometer at moderate temperature. These simulations can be

particularly useful in detailing interfacial resistances. Shenogin *et al.*. [5] performed MD simulations on an interface comprised of a SWNT and a liquid designed to simulate randomly dispersed CNT composites and demonstrated that the interface resistance decreases as the tube length increases. Cao *et al.*. [66] recently performed atomistic simulations of heat flow at an aligned CNT/Si interface, showing that the interfacial conductance increased with tube length and contact pressure. It was also shown that the interfacial resistance decreases with increasing temperature. At higher temperature the difference in the phonon spectrum between CNT and Si is reduced thereby increasing the efficiency of thermal transport across the interface.

2.4 Experimental Characterization Techniques of Emerging Interface Materials

In addition to the fabrication of the aforementioned materials, there have also been improved thermal characterization techniques, which reportedly provide increased accuracy over standard measurement methods. These techniques can measure resistance, R''_{tot}, or in specific circumstances, resistances at the interface of the TIM and the mating substrate. It is apparent that such tools are necessary for the continued reduction in thermal resistance. The following describes several of these experimental characterization techniques.

2.4.1 Steady-state Measurement

Steady-state measurements have generally been based on the ASTM D5470 tester which is a one-dimensional testing method in which the specimen is placed between two co-planar surfaces [6, 7, 67, 68]. One of the arms of the test fixture is typically electrically heated, while the other is cooled such that a nearly uniform heat flux is established through the sample. An example of such a test fixture can be seen in Fig. 2.3(a). R''_{tot} of the sample is found by extrapolating the temperature difference between the two arms of the test fixture. Specially designed test fixtures can be used to apply a

constant pressure to the sample in order to simulate real package situations; additionally they can come equipped to optically determine the deformation of the sample upon loading and heating. Since the measurement area is away from the sample, other resistances up to the sample area need to be accounted for. These include attachment greases between the test specimen and the arms of the test fixture. Depending on the properties of the test fixture or the joining materials the leading resistances may be higher than the expected resistance of the sample; therefore, particular care must be given during loading of the sample for accurate evaluation of R''_{tot}. Also due to the additional resistance sources applicable to these systems, high experimental uncertainty is expected.

2.4.2 Laser Flash Measurement

The laser flash measurement technique is a non-contact method capable of determining the thermal diffusivity, α, of the material.[69, 70] In the set-up shown in Fig. 2.3(b), a flash lamp (typically xenon) is used to irradiate one side of the sample, while the temperature of the backside surface is monitored by an infrared detector. The temperature of the backside is plotted versus time and the thermal diffusivity is typically determined by fitting the data to various models which incorporate the boundary conditions of the test fixture. This technique has been widely used in the measurement of composite materials and has more recently been used for VACNT samples. There have been some concerns as to whether the system can accurately measure properties of TIMs comprised of multiple interfaces [71, 72]. This system does have the drawback in that the materials properties including ρ and C are needed for extraction of the k. Evaluation of an effective thermal conductivity for VACNT TIM presents challenges due to their porous nature. and potentially large interfacial resistances.[72]

2.4.3 Photoacoustic Technique

In the photoacoustic (PA) technique, a laser is used to irradiate and heat a sample loaded in a PA cell [56]. As the sample is heated up, there is conduction within the surrounding air in the PA cell that results in a change in pressure of the surrounding gas, causing an acoustic response, which is measured by an attached microphone. The properties of the multilayer sample are extracted through a set of transient heat conduction equations that includes variations in the surroundings of the sample sensed by the microphone. A figure of the test fixture for a photoacoustic measurement can be seen in Fig. 2.3(c) [56]. Reported interface resistances obtained with this technique are below $1\,\mathrm{mm}^2\ \mathrm{K\ W}^{-1}$. This technique has recently been used extensively in the measurement of VACNT samples [54, 56, 73, 74]. Uncertainty particularly depends on what is being measured. The R''_{tot} results in a unique solution for a best-fitting algorithm, while for multi-layered samples finding the interfacial resistance results in a non-linear regression which can result in higher uncertainty.

2.4.4 The 3ω Method

The 3ω method is a transient technique in which a strip heater in contact with the sample is heated by an alternating current at frequency ω. This induces a temperature variation within the sample at 2ω and a voltage drop across the heater at frequency 3ω, which is measured through a lock-in amplifier is related to the temperature oscillation along the metal bridge. [75]. This T oscillation is dependent on the thermal properties of the sample of interest. Hu *et al.*. [10] recently used this technique in the measurement of k_{eff} of VACNT samples. A metal bridge was fabricated on a glass substrate and a top layer of silicon nitride was deposited to electrically insulate the bridge from the CNT array. The CNT array was then pressed to the metal bridge and a current was applied through the bridge. The voltage drop across the metal bridge containing 3ω voltage

component was then measured. A transient one-dimensional model was used to extract the *k* since the width of the heater was several times larger than the thickness of the CNT layer and also since the in-plane *k* of the CNT array was considered to be negligible. The *k* was then found by fitting the data to the transient model.

2.4.5 Thermoreflectance

The thermoreflectance technique uses a high power laser to irradiate a sample surface causing periodic temperature oscillation [55, 74-76]. A second probe beam is focused on the other side of the sample as shown in Fig. 2.3(d). The intensity of the reflected signal and the phase are dependent on the thermal properties of the sample and are used to extract the properties. The measured parameters include the individual thermal resistance at the interfaces. Tong *et al.* [55] used this measurement method to determine the thermal conductance of the two interfaces on a CNT array structure and the cross-plane conductivity of the CNT array. Also Panzer *et al.* [77] has used this technique to analyze the thermal performance of metal coated single-wall VACNT arrays.

2.4.6 Infrared Microscopy

This steady-state measurement technique has several advantages over other previously described methods, including the elimination of the need for intrusive temperature monitoring devices like thermocouples near the sample area for precise measurements, as well as knowledge of the sample C and ρ. This technique has been previously used to measure R''_{tot} from a double sided VACNT arrays [78]. Additionally uses of this measurement include the thermal characterization of aligned CNT composites, and boron nitride based underfills materials.[49, 79] Table 2.3 describes reported resistance ranges and uncertainties to several common TIM characterization techniques for measuring next generation materials.

Table 2.4 Metrology techniques for characterization of next-generation TIM

Method	**Reported Range** $mm^2\ K\ W^{-1}$	**Approximated Uncertainty** $mm^2\ K\ W^{-1}$
Steady-state [3,41]	20-200	10
Photoacoustic [22,23,83]	~1-20	0.5
Thermoreflectance [22]	~1-20	0.1
Infrared Microscopy [44,45]	~5-50	1
Laser Flash	0.01-1000 $mm^2\ s^{-1}$	3%

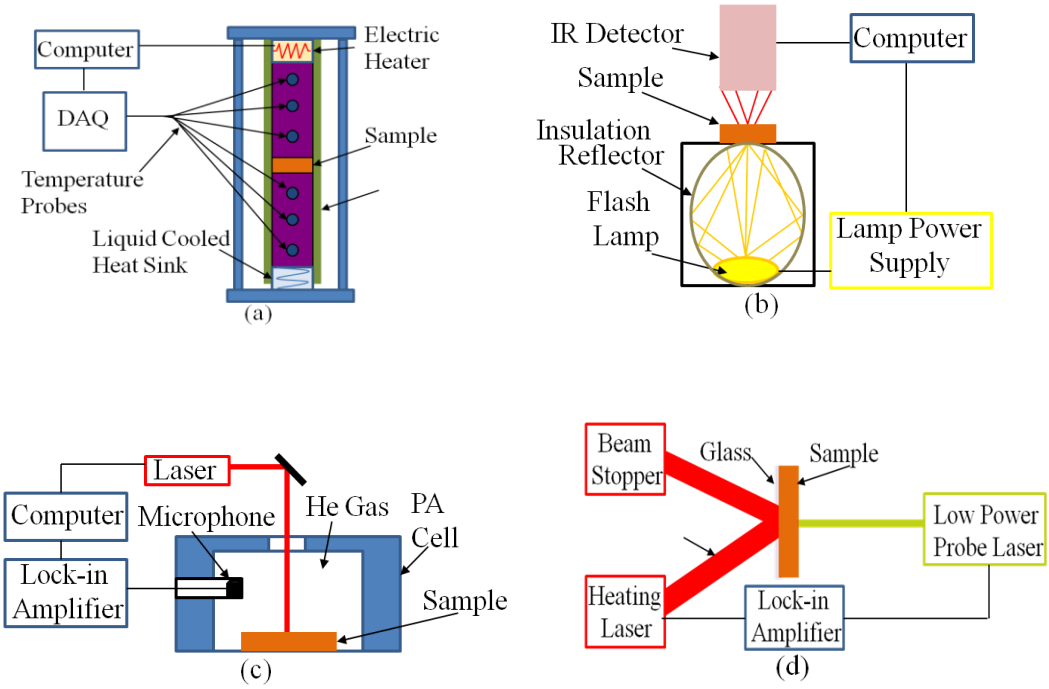

Figure 2.3 TIM thermal metrology tools (a) steady-state ASTM standard tester, (b) laser flash measurement system, (c) photoacoustic measurement, (d) thermoreflectance

2.5 Conclusion

With rising chip level heat fluxes, continued TIM development to reduce overall thermal resistance is of increasing importance. Nanostructured TIMs promise improvement in effective thermal resistance compared to conventional bulk materials. However, a number of advancements are needed before the promise of such materials is

fully realized in practical applications. Particular emphasis is needed on the alignment of materials and reduction of boundary resistances at the interfaces between the fillers and the matrix. For VACNT TIM, improvements in CNT synthesis including precise control over volume fraction, elimination of defects, and array height are all needed. Furthermore, the ability to effectively mechanically transfer the arrays from their native substrates to separate usable substrates is critical for potential commercial use. Mechanical transfer mechanisms must reduce interfacial thermal resistances, while ensuring all CNTs are being effectively used in heat conduction. For nanoparticle based composite TIMs, hybrids of multiple sized particles show promise in enhanced thermal transport. Also, functionalizing the particles with an additional agent meant to reduce boundary resistance between the particles and the matrix is to be investigated further.

The manufacturing and assembly challenges for nanostructured TIM are complemented by those in thermal characterization of these multi-scale materials. While the smallest sizes of interest are in the nm range, the layer thickness and other dimensions may be in mm or cm. Continuum based modeling, coupled with underlying atomistic modeling will continue to be developed to provide insight into TIM thermal properties. Atomistic models can be used to evaluate the boundary resistances of newer materials, which may be used to mate aligned CNT, or nanoparticles to other substrates. Modeling can also be done to examine the time dependent behavior and any performance degradation of TIM during operating conditions, particularly nanoparticle loaded greases. In addition, effects of increased contact pressure, particularly as related to VACNT array performance, need to be addressed. Thermal characterization techniques will continue to be developed which can accurately and rapidly determine the total thermal resistance of these materials. Measurement standards for low thermal resistance samples, below 1 mm^2 K W^{-1}, would provide more confidence in interpreting results. These standards could include sample size, attachment pressure and measurement temperature.

Furthermore, since the materials will be expected to withstand harsher operating conditions than current TIM, extensive experiments are needed that prove TIM reliability through their entire use. Results of TIM thermal performance through temperature cycling, or prolonged exposure to heat need to be conducted and, in the event of sample degradation, corrected. Ideally, real time data of thermal performance can be obtained, under harsh conditions.

CHAPTER 3

STEADY-STATE IR MEASUREMENTS AND RESULTS OF THERMAL INTERFACE MATERIALS

In order to characterize VACNT based TIM a steady-state IR system was used to measure the R''_{tot} through a sandwich structure. The following chapter will describe background associated with IR thermal imaging, the experimental setup used to measure the sample interfacial resistance, the system uncertainty as determine through standard error propagation analysis, validation of the system through the use of commercial TIM, and discussion of results of VACNT based TIM. Also comparison will be made between the measured values from the IR setup and Laser Flash measurements which were carried out at the National Renewable Energy Laboratory. Furthermore thermal spreading through a VACNT was observed using an IR measurement and will be discussed.

3.1 Infrared Imaging Background

Infrared (IR) thermometry has quickly become one of the most widely used forms of noninvasive temperature measurement.[76] The majority of the devices used in infrared thermometry are classified as spectral band thermometers.[80] These thermometer devices measure a surface's radiance over a narrow wavelength band which depends on the particular application. The principle of the operation is to collect radiation from the targeted source, filter it to through the spectral band of interest and then measure that radiation through a detector.

The measurement equation for a radiation thermometer as an IR system is [79]

$$S = A_t \delta\Omega \int_{\lambda-\Delta\lambda/2}^{\lambda+\Delta\lambda/2} \tau_\lambda R(\lambda) L_\lambda(\lambda) d\lambda \tag{3.1}$$

where S is the detector output, A_t is the target area viewed through the detector through solid angle $\delta\Omega$, τ_λ is the spectral transmittance of the microscope system which may include filters and lenses, $R(\lambda)$ is the reponsivity of the detector, and $L_\lambda(\lambda)$ is the spectral radiance that reaches the detector. Generally it is recommended that the emission from the target be much greater than that from the environment, either directly toward the detector or reflected by the target.[76] The radiance due to pure emission is given as

$$L_\lambda(\lambda) = \varepsilon_\lambda L_{\mathrm{b},\lambda}(\lambda, T) \tag{3.2}$$

where $L_{\mathrm{b},\lambda}(\lambda, T)$ is given by Planck's Law

$$L_{\mathrm{b},\lambda}(\lambda, T) = \frac{2hc_0^2}{\lambda^5\left(\exp(hc_0 / \lambda k_{\mathrm{B}} T) - 1\right)} \tag{3.3}$$

where h is Planck's constant, k_{B} is Boltzmann's constant, and c_0 is the speed of light.

IR detectors can be broadly grouped into two main categories: quantum and thermal detectors. Quantum detectors measure the direct excitation of electrons to conduction states by incident photons. These detectors typically have high noise at room temperature. The noise level is temperature dependent so the detectors are typically cryogenically cooled to reduce noise. The second category is thermal detectors, which collect electromagnetic radiation and cause the detector to heat. Such devices include bolometers, pyroelectric detectors, and thermopiles. The quantum detectors generally have a faster response than the thermal detectors which rely on the resulting temperature change due to photon absorption.

Measurements using infrared thermometers can be subject to several sources of error primarily associated to background radiation and surface ε_λ. The ε_λ of a material is defined as the ratio the actual emissive power of a surface to that of a black surface at the same conditions.[81] Background radiation includes any radiation that is not associated with the primary target. One method of decreasing these errors is to ensure

that the target completely fills the field of view. Then the only background radiation present is that which is reflected from the surroundings onto the sample surface. This can be achieved using a microscope lens to focus on the area of interest of the sample. Another source of error is a lack of previous knowledge of the material's ε. The spectral emittance is known to vary among materials with larger values in the IR for non-metals, and smaller values for metals which are highly reflective. Furthermore, the ε can be affected by surface features. Methods to account for this variation, which have been noted in the following experimental setup, include coating the target for a uniform ε, as well as ensuring that the surface is well maintained through polishing.[82]

3.2 Experimental Setup

Using the IR microscope, the R''_{tot} through each interface can be characterized using the steady-state IR microscope technique. The R''_{tot} measured by the technique is given as [2]

$$R''_{tot} = R''_{C1} + R''_{C2} + R''_{int} \tag{3.4}$$

where R''_{C1}, R''_{C2} are the contact resistances between the TIM and the substrates which for bonded VACNT arrays as will be discussed includes the intrinsic *k* of the bonding agents, and R''_{int} is the intrinsic resistance the TIM material itself.

The through thickness R''_{tot} measurement used an Infrascope II by Quantum Focus Instruments as shown in Fig. 3.1.[83] The quantum InSb detector used is sensitive to radiation in the 1-5 μm wavelength range and uses 3 objective lenses (1x, 5x, 15x) with a minimum spatial resolution of 3 μm using the 15x lens and produced a temperature mapping of 256 x 256 pixels. The actual pixel size for the stead-state camera is shown in Table 3.1. The full system was mounted on a Kinetic Systems Inc. Vibraplane® workbench to lessen motion during measurement. The IR system permitted 6 degrees of freedom (no rotation) for the camera turret to course and fine focus on the

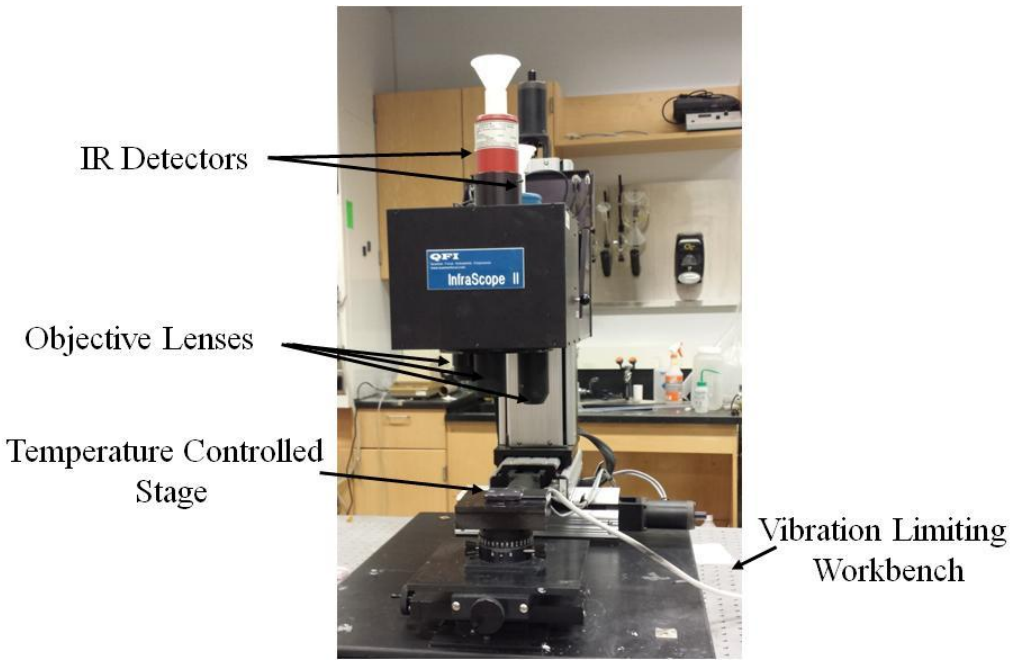

Figure 3.1 QFI Infrascope II IR microscope

sample holder. The steady-state InSb infrared detector used in these measurements was cryogenically cooled using liquid nitrogen (LN2) to reduce signal noise during measurements. The steady-state detector reportedly held 300 ml of LN2 but for initial cool down required nearly 1.5 liters of LN2.[83] The dewar was full when the LN2 would boil out from under the metal funnels.

The test fixture, shown in Fig. 3.2, was used to generate a thermal gradient across the samples thickness which is observed using the IR microscope on the polished sample edge. A custom developed copper block, suitable for the 1 cm^2 nominal square samples used, was developed which would thermally insulate all sides of the sample except for the sides exposed to the camera, heater, and copper block. A set of beryllium oxide (BeO) heaters were used to supply heat to one side of the sample. The heater was powered using an Agilent 6644A DC Power Supply $(0-60\ \text{V}/0-3.5\ \text{A})$ The opposing sample side was then affixed to the copper block and was cooled through the use of a thermoelectric module (Custom Thermoelectric). The thermoelectric module was

Table 3.1 Steady-state IR detector pixel size

Microscope Objective Lens	Measurement Spot size (μm)
1x	18.7
5x	4.4
15x	1.6

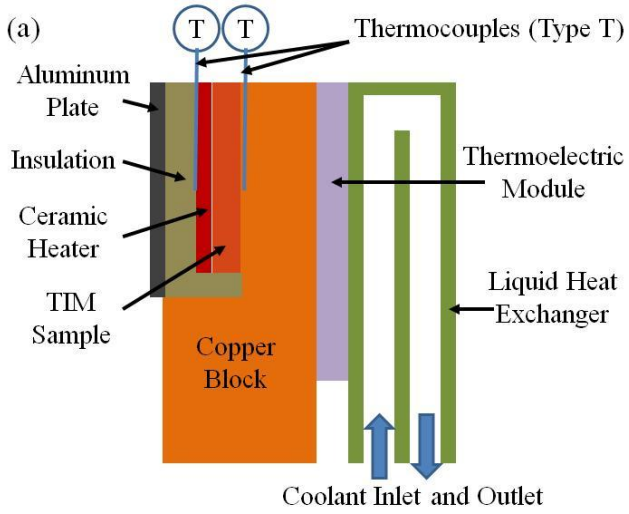

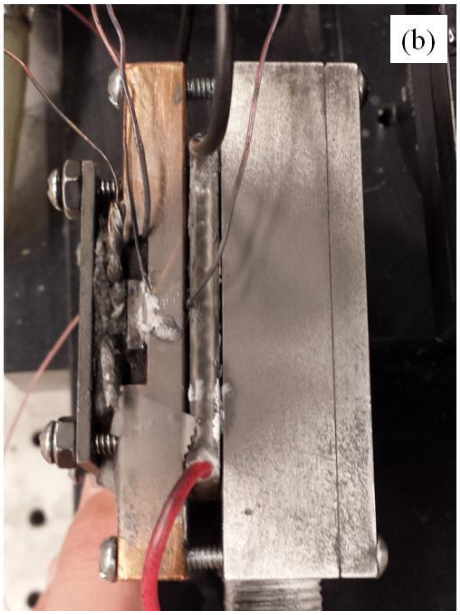

Figure 3.2 (a) Schematic of steady-state IR microscope imaging test fixture (b) photo of top view of test fixture

powered using a Xantrex XPF 35-10 Dual Power Supply $(0-35\ \text{V}/0-10\ \text{A})$. The thermoelectric was additionally used during the ε_λ measurement in order to bring the sample to a uniform temperature, as measured by type-T thermocouples (Omega) between the sample and the copper block and behind the BeO heater. The thermocouple data was recorded and stored using an Agilent 34970A Data Acquisition/Switch Unit. A refrigeration unit (Lab Companion RW-1025G) was used to pump chilled water through the heat sink which rejected the heat from the heater and the thermoelectric cooler. For moderate heating powers $(<75\ \text{W})$ water was used while at higher power measurements $(>75\ \text{W})$, necessary for low R''_{tot} samples, a water-ethylene glycol mixture was used through the heat sink to maintain all the samples near 70 ^{o}C for each measurement. The attached thermocouples on either side of the sample were further used to determine when steady conditions for the reference measurement and R''_{tot} measurement had been established.

Figure 3.3 shows the initial startup menu following a background radiance measurement. Following the background measurement, the microscope is focused on the thermal target. The focusing was controlled through both an equipped manual control box, which allowed for 6 degrees of motion and course focusing and also through the IR software for fine focusing. A reference ε_λ mapping was taken after the microscope had been properly focused on the area of interest by using the thermoelectric module in a heating mode to heat the sample to manufacturer recommended measurement temperature of 70 ^{o}C. This was done to reduce the influence of background radiation during the actual measurements. The interface for the TIM samples to me analyzed was determined by finding a discontinuity along the samples edge. For the reference ε_λ mapping, the microscope measured the sample's radiance at a fixed temperature. Each

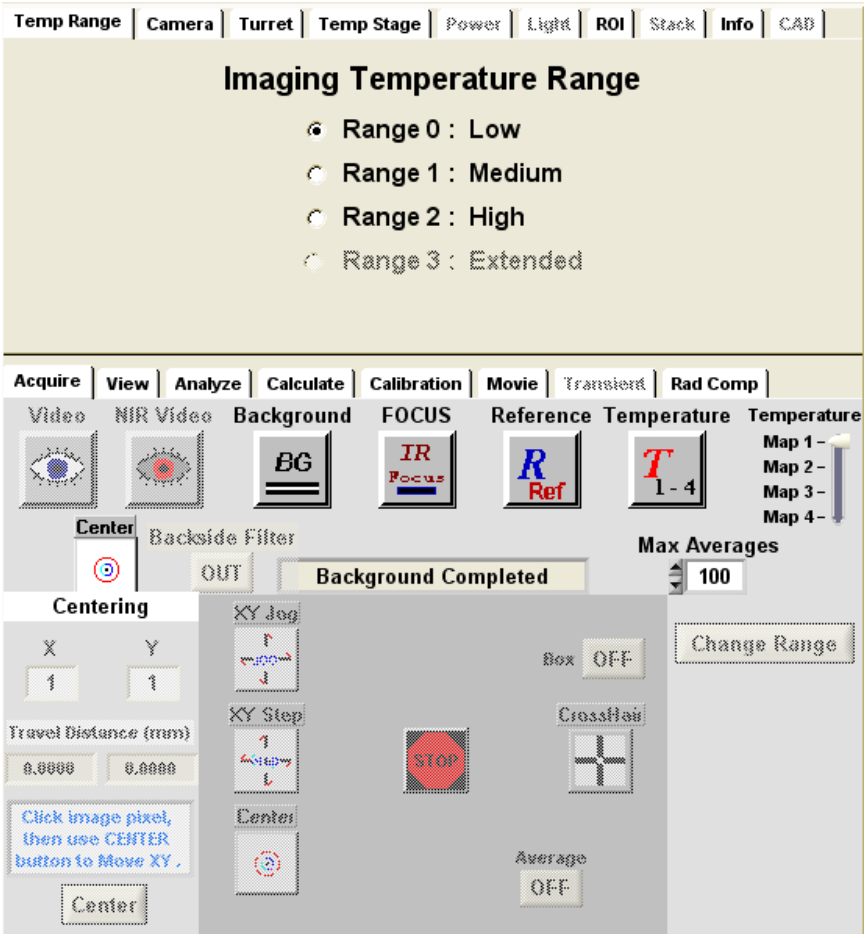

Figure 3.3 Initial startup menus for IR measurements using Infrascope 2 software

pixels stored valued was converted to a reference ε_λ . The stored ε_λ mapping was recalled while measuring the powered sample's thermal gradient induced radiance to convert to actual temperature. Care was taken to limit the vibration during this critical measurement including taping down hose connections from the liquid heat exchanger and lead wires to the ceramic heater and thermoelectric module and also clamping the full test fixture to the temperature controlled stage. Furthermore, the sample edge to be measured was coated with a carbon spray which provided a near uniform emittance (0.9-0.95) prior to measurement, in order to further reduce variability in the measured radiance.

Additional tabs, which can be seen in Fig. 3.3, include the "Temp Range" tab with set points of low, medium, and high, depending on the application. For the majority of the TIM measurements below 120 ^{o}C the system could be left in the default low position.

The "Turret" tab permitted for autofocus by the IR software on the sample after the camera had been focused with a lower magnification lens. The "Temp Stage" tab allowed for a manual temperature override setting during the reference ε_λ measurement rather using the set point temperature of the temperature controlled stage. Additional tabs include the "View" tab which allowed for visualization of the temperature, radiance, and ε_λ mappings. The "Analyze" tab was used for pixel blocking, as will be discussed, for temperature averaging, determining the number of pixels, and the evaluating the standard deviation of the temperature readings. Furthermore the "Line Trace" command was used for the determination of certain lengths of area and will be further discussed in Chapter 5 as will the "Movie" tab.

Following the reference ε_λ measurement using the thermoelectric module, the polarity of the module was reversed and power was supplied to the ceramic heater to form a gradient through the sample. The thermal map was captured and stored in one of the 4 slots for later analysis, and the camera was repositioned and focused on a different interface region to ensure the sample's measured R''_{tot} was consistent across the sample. The A_c of the TIM samples was measured prior to measurement using calipers. The heater power, Q, given as the product of the applied voltage, V, and current, i, was used to compute the heat flux along with A_c. Measured temperature regions on either side of the interface, T_{High} and T_{Low}, are determined by blocking and averaging temperature values of approximately 10 % of either the Cu or Si substrates using the built in camera software mean calculation, as shown in Fig. 3.4. The overall R''_{tot} was then determined by

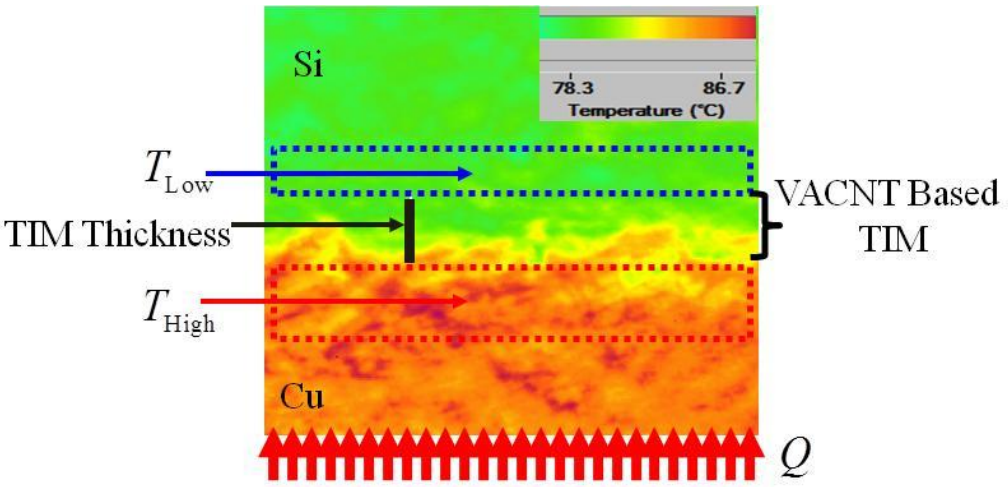

Figure 3.4 Representative IR images TIM sample

$$R''_{tot} = \frac{(T_{High} - T_{Low})A_c}{Q} \tag{3.5}$$

The prepared TIM materials were all placed in between rigid substrates including copper and silicon. A thin layer of thermal grease (ShinEtsu G571) was applied at the interfaces of the heater/sample and the sample/cooling block to promote a continuous thermal path from the heater to the cooling block.

3.3 Experimental Uncertainty

Experimental uncertainty in the total thermal resistance measurements was estimated using a standard error estimation approach given as

$$\delta R''_{tot} = \left[\sum_{i=1}^{n} \left(\frac{\partial R''_{tot}}{\partial X_i} \delta X_i \right)^2 \right]^{1/2} \tag{3.6}$$

where $X_i = T_{High}, T_{Low}, A_c, i, V$. Uncertainty analysis has been performed on the key instruments with combined uncertainties shown in Table 3.2. The uncertainty for T_{High} and T_{Low} is determined by using a conservative sensitivity (0.30 ^{o}C) to account for errors in reference emittance calibration and statistical variation of the thermal images.

Table 3.2 Experimental uncertainty for IR steady-state measurements

Variable *X*	**Combined Uncertainty**
T_{hot} and T_{cold}	0.31 ^{o}C
A_c	0.63 mm^2
i	0.013 A
V	0.061 V

Taking a representative sample standard deviation of the temperature measurement in the blocked area (0.75 ^{o}C) the statistical variation based uncertainty is given by

$$U_{Stat} = \frac{k_c SSD}{\sqrt{N}} \tag{3.7}$$

where k_c is the coverage factor for a 95 % confidence interval and N is the number of data points (over 900 pixels) in the averaged areas for T_{High} and T_{Low}. The area uncertainty is based on statistical variation uncertainty from Eqn. (3.7). The uncertainty in the current supplied and the read back accuracy of the voltage across the resistor are 0.15%+4.1 mA and 0.07%+40 mV respectively.[84] Measurement precision is based on the last stable digit for each of the respective digital readouts, namely, 0.01 V and 0.01 A.

Figure 3.5 shows the uncertainty as a function of a TIM sample R''_{tot} for various input heat flux. For low R''_{tot} samples (< 7 mm^2 K W^{-1}), a heat flux greater than 62.5 W cm^{-2} is necessary to generate a sufficient temperature gradient across to the TIM layer to be accurately measured with the IR system. Lower heat flux would provide a much higher measurement uncertainty. For larger R''_{tot} (> 20 mm^2 K W^{-1}) VACNT based TIM, lower heat fluxes can be used to achieve the needed temperature difference for accurate measurements. Additionally, the lower heat flux for such samples is

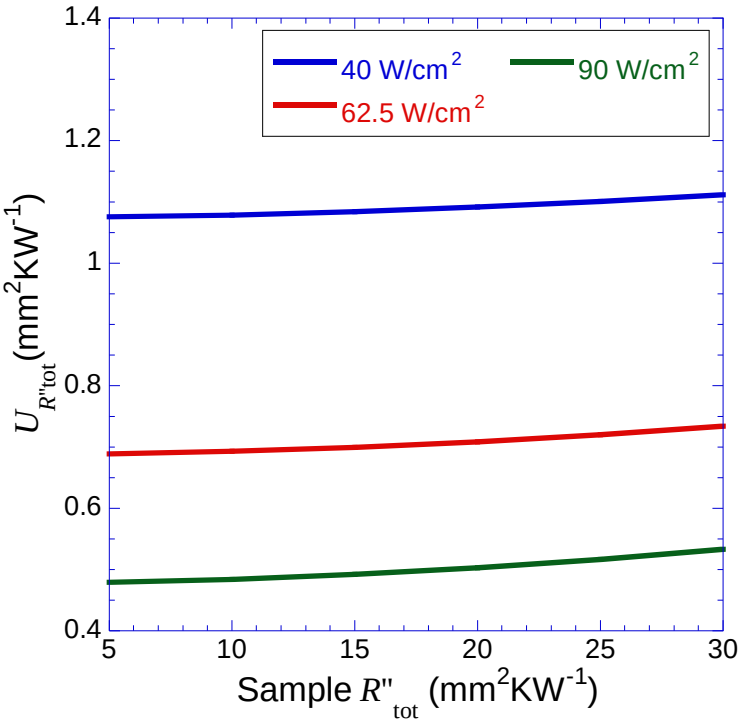

Figure 3.5 Total uncertainty based on Eqn. (3.6) for the measurement of TIM R''_{tot} using IR imaging

necessary such that the heater temperature does not become too excessive. The error, as shown, for the higher R''_{tot} samples is still lower on a percent basis, than that with low R''_{tot}.

The heat loss through the sample was modeled through COMSOL using a representative maximum power of 100 W. The custom test fixture, insulation, heater and sample were all included in the analysis. A constant backside temperature corresponding to a constant temperature of the thermoelectric module was supplied to the backside of the copper test fixture. The heater was taken as a volumetric heat source and natural convection and radiation boundary conditions were used on all other surfaces. A simulated test fixture and sample are shown in Fig. 3.6(a). Figure 3.6(b) shows the heat flux distribution through the sample. The total heat flux loss through the sample was less than through this simulation.

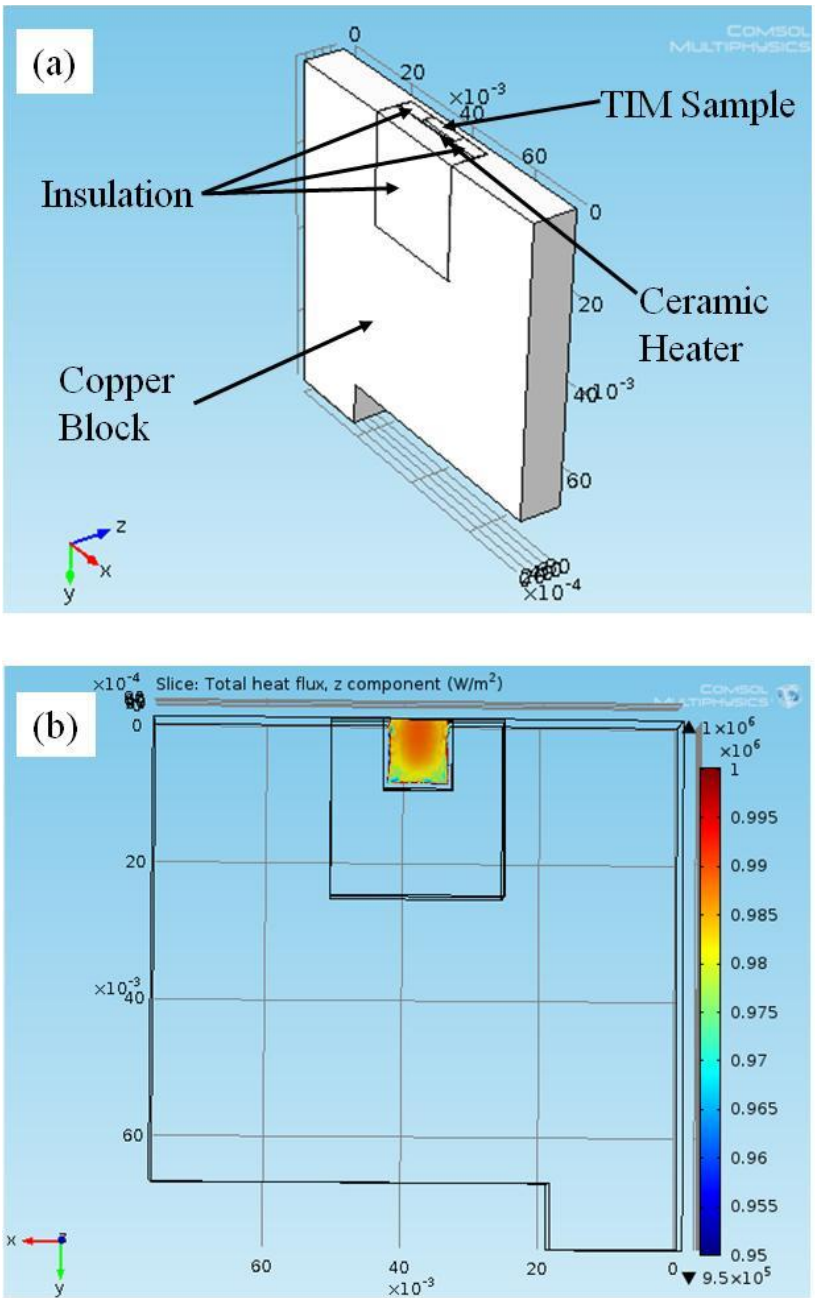

Figure 3.6 Numerical simulations of heat losses during steady-state experiments

3.4 Validation of Steady-state IR Measurements with Commercial Samples

Three commercial TIMs were analyzed using the current IR system. These include Hi-Flow® 225UT from The Bergquist Company (hereby referred to as PCM1), Loctite® Silverstrate® from Henkel Technologies (referred to as PCM2) and

Table 3.3 IR steady-state measurement of commercial TIM [85-87]

Sample	TIM Thickness (μm)	Reported Resistance (mm^2 K W^{-1})	IR Measurement Value (mm^2 K W^{-1})
PCM1	77	45-58	57.3
PCM2	107	8-15	11.8
TCA	100	16.7-20.3	18.2

Ablethermᴿ 3188 from Ablestik (referred to as TCA). PCM1 is a pressure sensitive TIM which changes phase above 55 °C.[85] It is supplied as two separate pieces which adhere to the opposing substrates and are then heated above the phase change temperature to create an interface. PCM2 is a phase change TIM above 51 °C and is supplied as a dry material coated onto an aluminum substrate.[86] TCA is a silver filled, oven cured, conductive adhesive.[87]

Table 3.3 describes the results of the steady-state IR measurements for the three samples and which are near their reported values. The values in Table 3.3 for PCM1 correspond to measurement attachment pressures between 68.9-344.7 kPa (10-50 psi), with the lowest reported thermal resistance occurring at 344.7 kPa. The attachment pressures for PCM2 are 137.9-275.9 kPa (20-40 psi). The reported thermal resistance values for PCM1 and PCM2 samples were measured using ASTM D5470 test fixture. The mounting pressure for this set of IR measurement was expected to be near 209 kPa (30 psi), as measured by an Ultra Low Pressurex® film from Sensor Products Inc. but this value is subject to variability, including how tightly the back aluminum plate is affixed to the test fixture, sample type, and sample thickness. The resistance given for the commercial measurement for the TCA sample is based on the reported thermal conductivity of 5.4 $W\,m^{-1}\,K^{-1}$ and an approximate sample thickness during IR

measurement of 90-110 μm. The commercial thermal conductivity measurement was made through a laser flash-measurement.

3.5 Measurement of Total Thermal Resistance of VACNT Based TIM

The following will describe the sample preparation and IR measurements of VACNT based TIM samples. The samples are composed of different interface attachments as will be described. Also VANCT TIMs will be further characterized after thermal aging and thermal cycling tests to address reliability concerns.

3.5.1 Sample Preparation

VACNTs were grown on silicon at ambient pressure using a Chemical Vapor Deposition (CVD) system. Al_2O_3 (10 nm)/Fe (2.2 nm) were used as CNT catalysts deposited via e-beam evaporation. The CVD growth of VACNTs was carried out at 750 °C with ethylene (130 sccm) as the carbon source and hydrogen (150 sccm) and argon (350 sccm) as carrier gases. The water vapor concentration in the CVD chamber was controlled by bubbling a small amount of argon gas through water. Ethylene flowed into the CVD system for CNT array growth for a preset time, after which the flow was terminated.

Various anchoring materials including TCA, silver based inks, and solders were considered for VACNT anchoring purposes.. In order to determine which materials would be considered initial R''_{tot} measurements of the anchoring materials alone were made. A measurement of the solder was not made since it was assumed due to its high conductivity and previous use as TIM that is would be a suitable anchoring material.. The other materials which were considered were a TCA (Diemat, Sk70) silver based ink (IncTec, PIA-KIA1) sample 1 and ink sample 2. The thicknesses of the TIM were

Table 3.4 IR steady-state measurement of VACNT anchoring materials

Sample	TIM Thickness (μm)	IR Measurement Value (mm^2 K W^{-1})
TCA	39	0.8
Silver Based Ink	20	21.6

determined through optical microscope inspection. After the results of these preliminary tests, shown in Table 3.4, it was concluded that future VACNT TIM be anchored using the TCA and solder attachments.

To prepare the VACNT TIM samples anchored using the TCA the VACNT on their native substrates were flipped onto a separate Si substrate which had a pre-applied TCA layer. 30 psi was use to press the VACNT array into the TCA layer to promote adhesion. The VACNT-TCA interface was cured at a maximum temperature of 200 ^{o}C with the nanotubes anchored by adhesion with the polymer. The array was fully transferred by peeling off the VACNT from the growth Si substrate. A TCA-coated Cu substrate was pressed into the exposed growth ends of the VACNT array at the same attachment pressure and was cured to anchor the array. The overall structure is Si-TCA-VACNT-TCA-Cu. Figure 3.7(a) shows an SEM image of the sandwich interface structure. The exposed compliant VACNT region is expected to still withstand thermal stresses due to mismatched CTE between the Cu and Si. The Ag particles provide additional thermal pathways for the CNT array. Figure 3.7(b) shows the CNT anchored to the adhesive through the cured polymer. The effective thermal conductivity of this newly formed CNT-polymer composite region is expected to be higher than the base polymer matrix.[88-90]

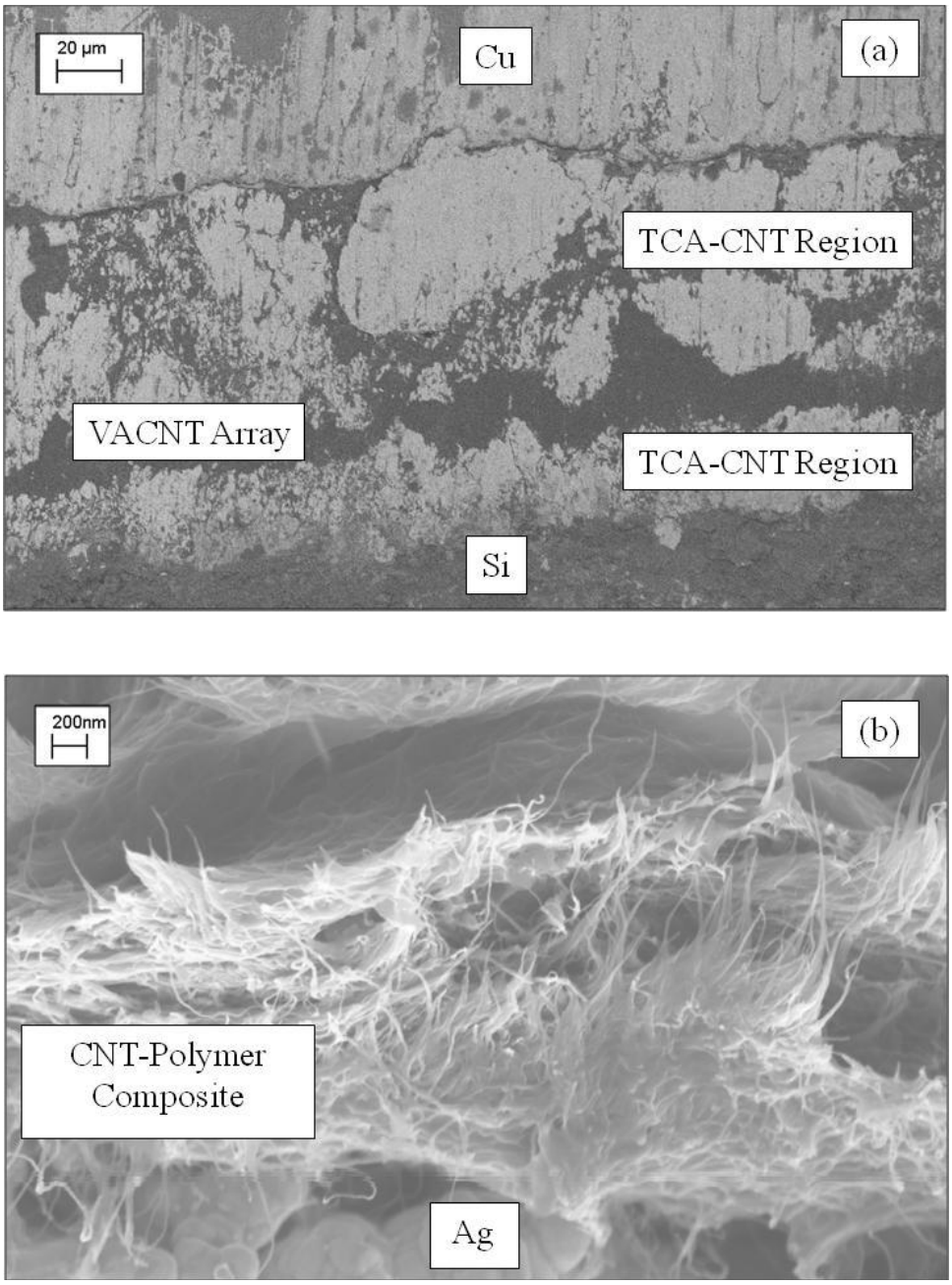

Figure 3.7. (a) SEM of TCA bonded VACNT TIM. (b) Zoomed in SEM showing bonding between CNT and polymer.

Pure indium (In) solder has also been used in multiple thermal management applications for interfacial resistance reduction.[91-93] Since In has a high intrinsic *k* of 81.8 $W\,m^{-1}\,K^{-1}$ it is not anticipated to contribute significantly to the thermal resistance of the TIM interface. Furthermore its low melting pointing of 157 ^{o}C makes indium soldering to microprocessors in organic packages possible. A thin In film (around 1 µm)

has been previously used to bond metalized CNT films to adjacent surfaces to reduce the contact resistance at the interface.[91] Both the top of the VACNT array, shown in Fig. 3.8, and the top of the to be bonded Si and Cu substrates were metalized with 30 nm titanium (Ti), 300 nm nickel (Ni), and 300 nm gold (Au) using e-beam evaporation. A 25 μm In foil (99.99%, Indium Co.) was then attached on the metalized silicon substrate. The metalized VACNT array on the silicon plate was placed upside down on to the top of the In/Si substrate, then the whole stack was put into a furnace for 10 min at 200 ^{o}C in a mixed gas flow of 300 sccm argon and 150 sccm hydrogen to make the VACNT/In bond. Light pressure was applied to materials during bonding to ensure good contact and wetting of the In to the Au surfaces. The growth Si was removed from the VACNTs that were transferred onto the In/Si substrate. Once transferred, a second metallization layer of 30 nm Ti, 300 nm Ni, and 300 nm Au was applied to the exposed end of the VACNT array.

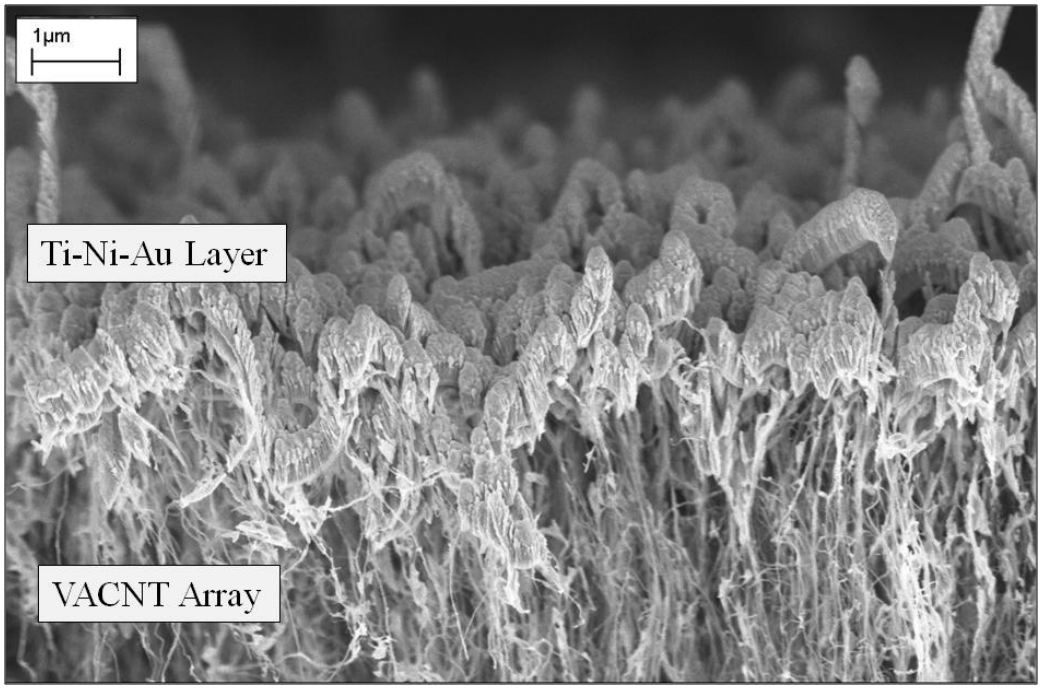

Figure 3.8. Metalized CNT used for In solder attachment.

Then, on a metalized Cu substrate, a 25 μm In foil was coated and then the transferred VACNT/Si was bonded to the indium/Cu substrate.

Additioanlly, from the laboratory grown VANCT samples, arrays were produced through a Black Magic commercial CVD system (AIXTRON). The Black Magic system deposits CNT through plasma enhanced CVD and thermal CVD. Al_2O_3 (10 nm)/Fe (0.8 nm) were deposited via e-beam evaporation to act as the catalyst for CNT growth. A gas mixture of acetylene/hydrogen at flow rate of 20/700 sccm was used for CNT growth at 15 mbar, after the system reached the temperature of 720 °C. Previous to steady-state IR characterization, transmission electron microscopy, raman spectroscopy [94, 95] and thermal gravimetric analysis tests were conducted with results indicating overall higher quality VACNT arrays than those from the laboratory system.[96]

3.5.2 Thermal Resistance Measurements of VACNT TIM using Steady-State IR Microscopy

The averaged R''_{tot} measurements for TCA anchored arrays of varying VACNT growth thickness are shown in Fig. 3.9(a). Each sample was measured at least two different locations along the sample edge and at various power levels. The uncertainty bounds for the measurements based on Eqn. (3.6) are also shown. These thicknesses are not directly correlated to overall VACNT TIM thickness, which also includes the thickness of the anchoring TCA layers. From Fig. 3.9(a) there exists no clear relationship between the CNT growth thickness and measured R''_{tot} using this TCA anchoring technique. Typically, the as-grown CNT have exhibited packing densities near 3-7% as determined through SEM analysis. For such an array where an individual CNT thermal conductivity is expected to be as high as 3000 $W\,m^{-1}\,K^{-1}$ and with a 100 μm nominal thickness for the array, the intrinsic thermal resistance would be expected to contribute

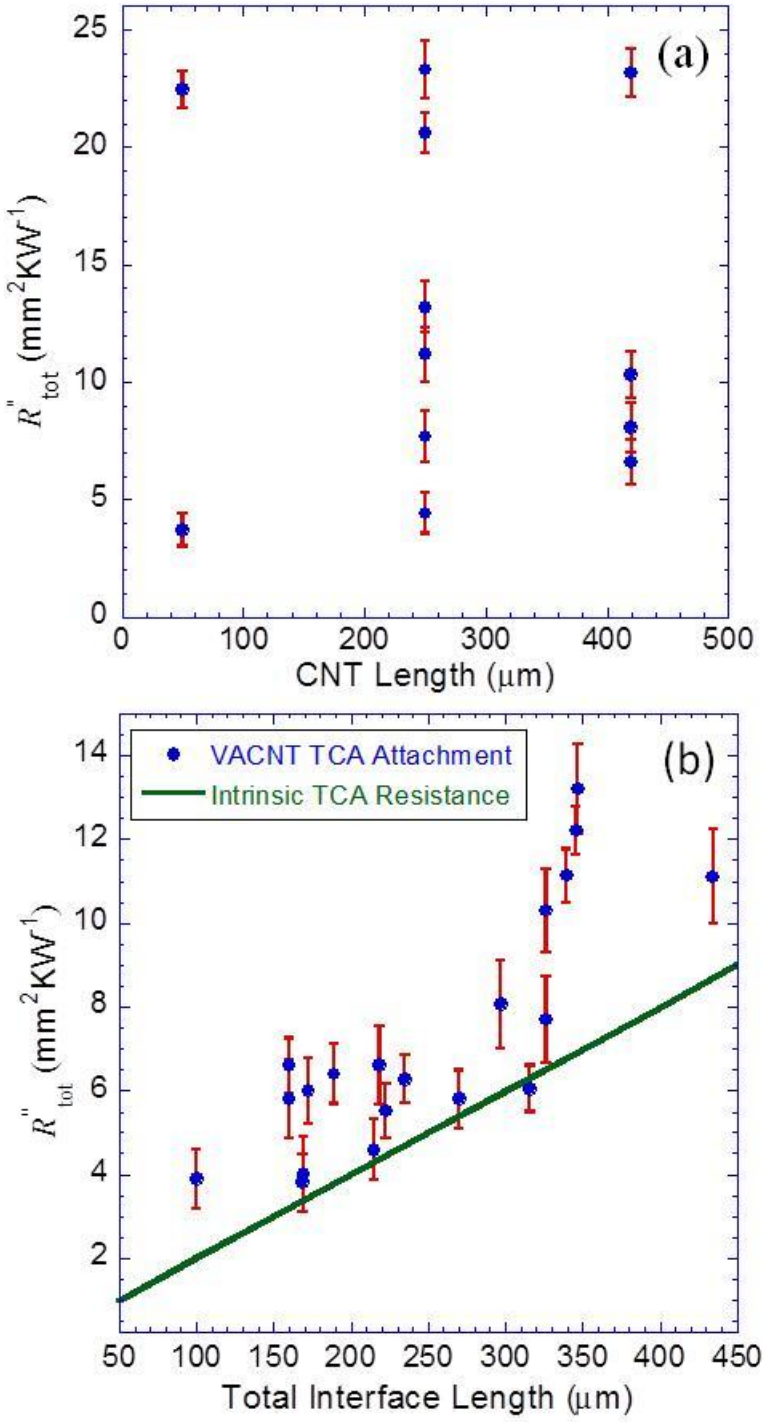

Figure 3.9 (a) Measured R''_{tot} of TCA based VACNT TIM as a function array growth thickness and (b) R''_{tot} for TCA based VACNT TIM of varying total interfacial layer thicknesses.

less than 1 mm^2 K W^{-1} which is significantly lower than the measured R''_{tot} here. It is then clear that the significant contribution of the VACNT TIM R''_{tot} is at the anchored regions between the TCA and VACNT layers. Figure 3.9(b) shows the variation R''_{tot} with full TIM thickness for CNT arrays attached using TCA adhesion layers. The as-grown VACNT had a nominal height of between 100-200 μm. Outliers due to poor bonding, including samples appearing in Fig. 3.8(a), which resulted in large R''_{tot} are not reported here. As can be seen, the lowest R''_{tot} is shown for the thinnest VACNT TIM materials. This can be attributed to the thickness of the TCA layers. Also plotted is the intrinsic resistance of the TCA layer. This was found by.

$$R''_{TCA} = \frac{k_{TCA}}{L_{TCA}} \tag{3.8}$$

The thickness of each TCA layer used for VACNT adhesion was between 50-200 μm as shown in Fig. 3.7(a) with the intrinsic TCA resistance in this range between $1-4$ mm^2 K W^{-1}. Accounting for two adhesion layers for full VACNT anchoring and additional interfacial resistances between the TCA, Cu, and Si substrates the VACNT layer shows an expectedly low contributing resistance. Furthermore, the presence of the VACNT within the TCA layer may have the effect of increasing its own intrinsic conductivity by forming CNT-polymer composite regions as seen in Fig 3.7(b).[88-90] Beyond 320 μm total interface thickness, where the TCA layers are expectedly larger, the TCA contribution would be as high as 8 mm^2 K W^{-1}, the increase in R''_{tot} of the VACNT cannot be directly correlated to the change in TCA thickness. This is then attributed to poor CNT infiltration into the TCA regions such that the full array was not participating in thermal transport.

A concern with any new TIM material is its potential delamination TIM and device failure due to prolonged use and thermal cycling between extreme temperatures.

Thermal cycling tests of TCA VACNT array were performed in which the sample was cycled 10 times from 0°C to 70°C at a ramping rate of 26°C/min in an environment controlled test chamber (ESPEC). Thermal aging tests were performed for 100 hrs. at 130 °C, after which the R''_{tot} of the TIM was again measured using the IR system. Figure 3.9 shows response of measured TCA bonded VANCT TIM to the changes given. As can be seen there is not a significant degradation for the TCA bonded VACNT. It would be expected, due to the large CTE mismatch between polymer and substrates, that there would be a large significant thermal degradation. Lin *et al.* [97] recently described how infiltration of the VACNT array may lower the effective CTE of a polymer/CNT material such that thermal stability concerns may be addressed. The best performing

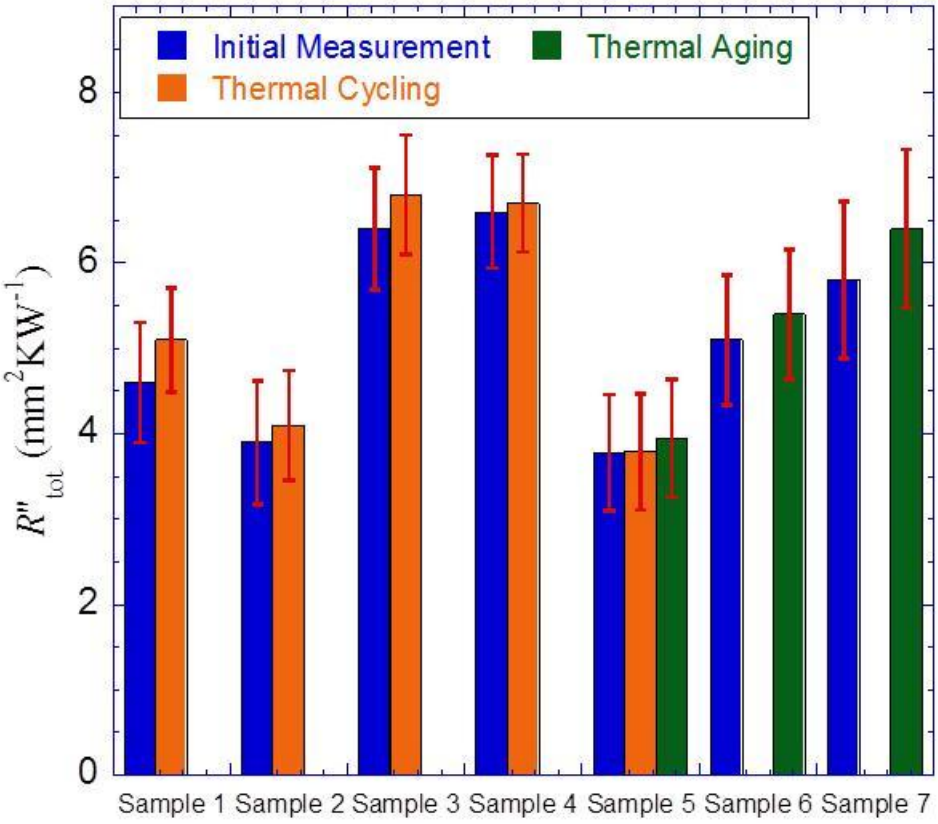

Figure 3.10. Thermal degradation of TCA based VACNT TIM due to thermal cycling and aging tests.

TCA anchored VACNT TIM (i.e. Sample 5 in Fig. 3.10) demonstrated less than 5% degradation after enhanced thermal cycling and aging tests (cycled between -40°C and 80°C 50 times and aged at 150°C for 300 hrs.).

Figure 3.11(a) shows the thermal resistance of the In based attachments made with the laboratory based CVD system. Due to the fact that the metallization layers on top of the VACNT array were not continuous as shown in Fig. 3.8, it is possible that incomplete wetting between the solder attachment and the array may limit the full performance of the VACNT array. Significant degradation of the TIM seen in Samples 1-3 after cycling and aging processes would indicate poor bonding. It is known that a significant issue related to solder use is void formation. Recent experiments however indicate that this approach may have thermal resistance on the order of ~1 mm^2 K W^{-1} .[55] Figure. 3.11(b) demonstrates results from the high quality VACNT arrays. While the lowest measurement ($R''_{tot} = 3.7$ mm^2 K W^{-1}) was lower than other laboratory attached solder samples ($R''_{tot} = 8$ mm^2 K W^{-1}) the higher quality did necessarily guarantee better thermal performance as shown in samples 4 and 5. Additional research is recommended into analyzing the role of VACNT quality on the anticipated overall thermal resistance.

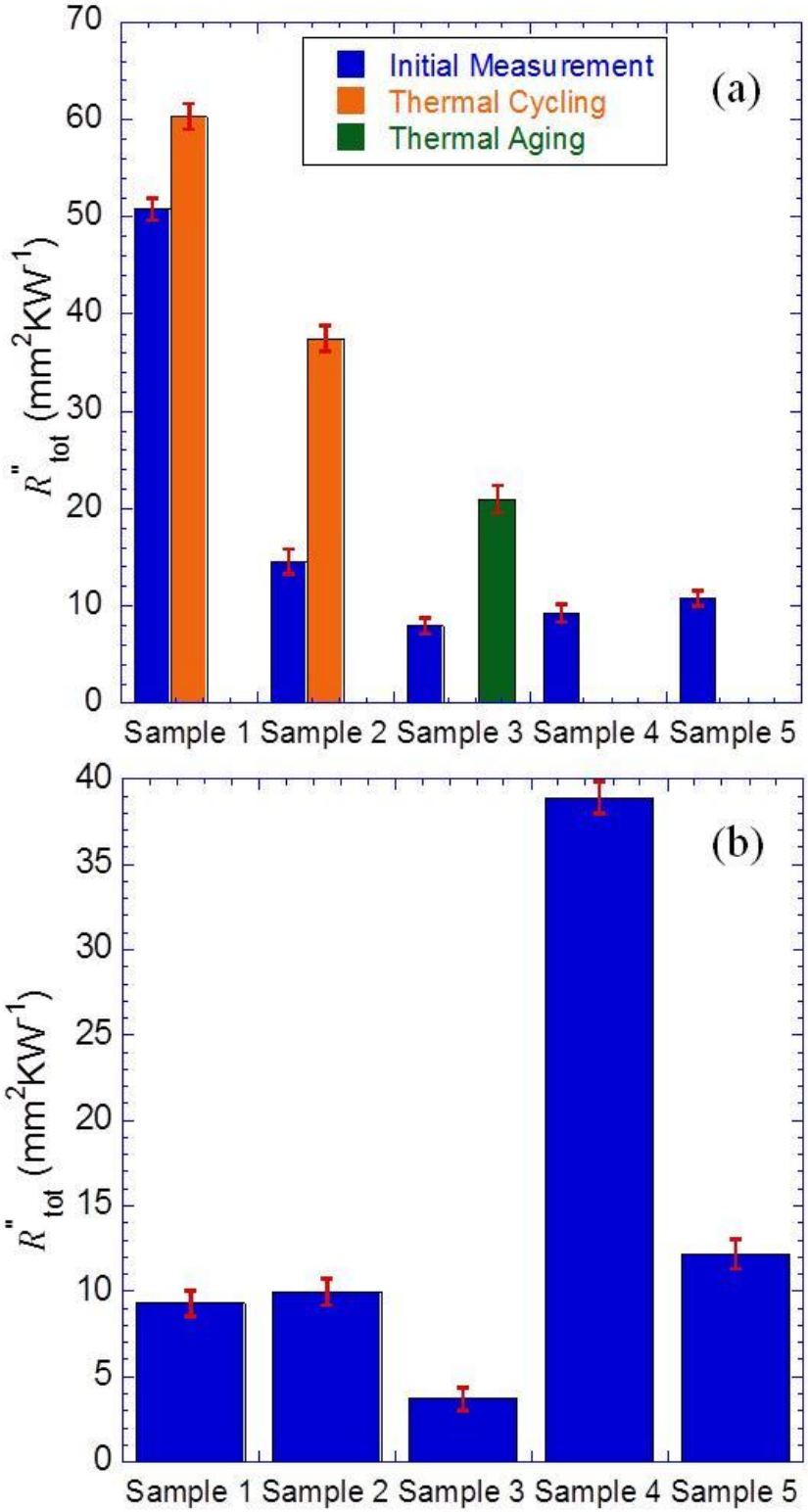

Figure 3.11. (a) R''_{tot} of solder based attachment and R''_{tot} after thermal cycling and aging tests. (b) Solder attached samples as prepared by Black Magic CVD system

3.5.3 Measurement of VACNT Based TIM Comparison Between Laser Flash and Steady-State IR Measurements

Thermal characterization of R''_{tot} using a laser flash measurements system located at the National Renewable Energy Laboratory (NREL) were conducted for the best performing samples steady-state IR measurements anchored using TCA. As mentioned in Chapter 2 the laser flash measurement works by irradiating a surface with a flash lamp and then measuring the transient temperature response as a function of time with an IR camera. NREL characterized the thermal resistance of samples using a Xenon Flash system and used average values of 4.5 g cm^{-3} for the density and 0.33 J g^{-1} K^{-1} for the specific heat in order to determine k_{eff} for the full TIM samples. The applicability of multilayer sample analysis for the measurement of TIM has been questioned in literature since it provides an effective thermal diffusivity which is calculated to a k_{eff} . The R''_{tot} is then found through the knowledge of the length of the interface as given in Eqn. (3.8).

Figure 3.12 shows the results of the NREL R''_{tot} measurements along with the measurements through the steady-state IR system. As shown, 9 of the 13 measured samples showed good agreement or within uncertainty bounds. Samples which had significantly higher resistance including samples 1, 2, 4, and 9 may have been damaged during the shipping process. Some of the measured R''_{tot} was actually better than was measured during the screening using the steady-state IR measurement (i.e. samples 6, 12, 13). However if the specific heat and density are not well characterized there can be errors in the measurements.

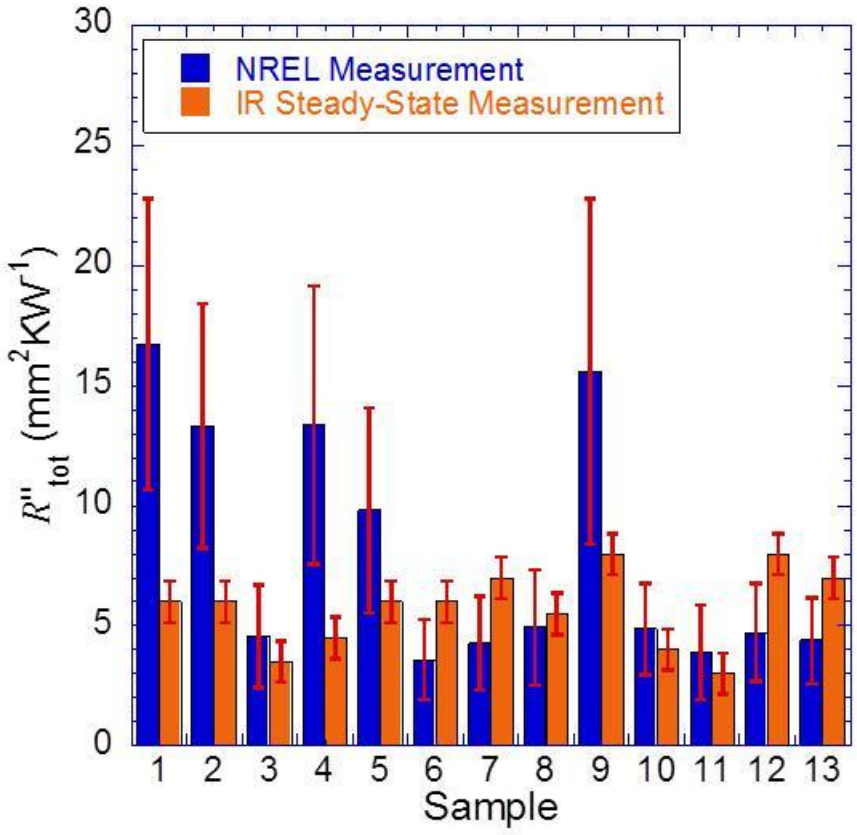

Figure 3.12 Comparison between IR measurements and NREL laser flash measurements

3.6 Pressure Dependence on Total Thermal Resistance for a VACNT TIM

Due to the weak contact formed when a VACNT array is attached to an opposing surface there has been work done on analyzing the pressure dependence of resistance for VACNT TIMs. Significant work has been done for non-bonded VACNT arrays which are in contact with Cu [98], Ni [99], and Ag [100] with all resulting in decreasing R''_{tot} with increased attachment pressure. Based on these measurements, Cola described that through increased contact area with increased pressure R''_{tot} would decrease.[51] Less work has been done in the analysis of bonded VACNT arrays. Xu and Fisher used an PCM to bond to VACNT array on Si and demonstrated that at low pressure (< 0.28 MPa) the PCM did not fully wet the array and there was a strong pressure dependence on R''_{tot} .[7] As the pressure was increased and the VACNT infiltrated the PCM, this pressure dependence greatly lessened. Furthermore, Barako *et al.* [93] measured an solder attached

sample with one side attached to the growth substrate, increasing pressure up to 600 kPa with R''_{tot} ranging from $28-71$ mm^2 K W^{-1}.

In order to assess the pressure dependence on R''_{tot} for the samples described here, 3 samples, 2 attached using TCA and the other with In were analyzed using a load cell. Figure 3.13(a) shows the load cell (Futek Advanced Sensor Technology Inc.) which was used to characterize this pressure dependence. The maximum compression of the cell was 25 lbs. The sensor head has a rectangular shape (16 mm x 4.7 mm) with a hole with which a set screw could be placed. A ceramic piece was cut to be the same size as the heater so that when pressed, the load cell was pressed in series with the heater and sample. The load cell was positioned between the aluminum plate and the heater as shown in Fig. 3.13(b). The load cell was pressed into the heater and sample by increasing the pressure that was applied through the aluminum plate. The same measurement procedure which was previously described was used during the measurements. After each measurement, the pressure was adjusted and the microscope was refocused before proceeding to subsequent measurements.

Figure 3.14 shows the edge view of TCA samples loaded into the test fixture. TCA Sample 1 has clear voids along the interface due to incomplete wetting of the TCA to the Si or Cu substrates. This poor contact may hinder full VACNT array participation leading to larger R''_{tot}. Alternatively for TCA Sample 2 shown in Figure 3.14(b) no clear voids along the interface were present indicating more complete wetting of the substrates.

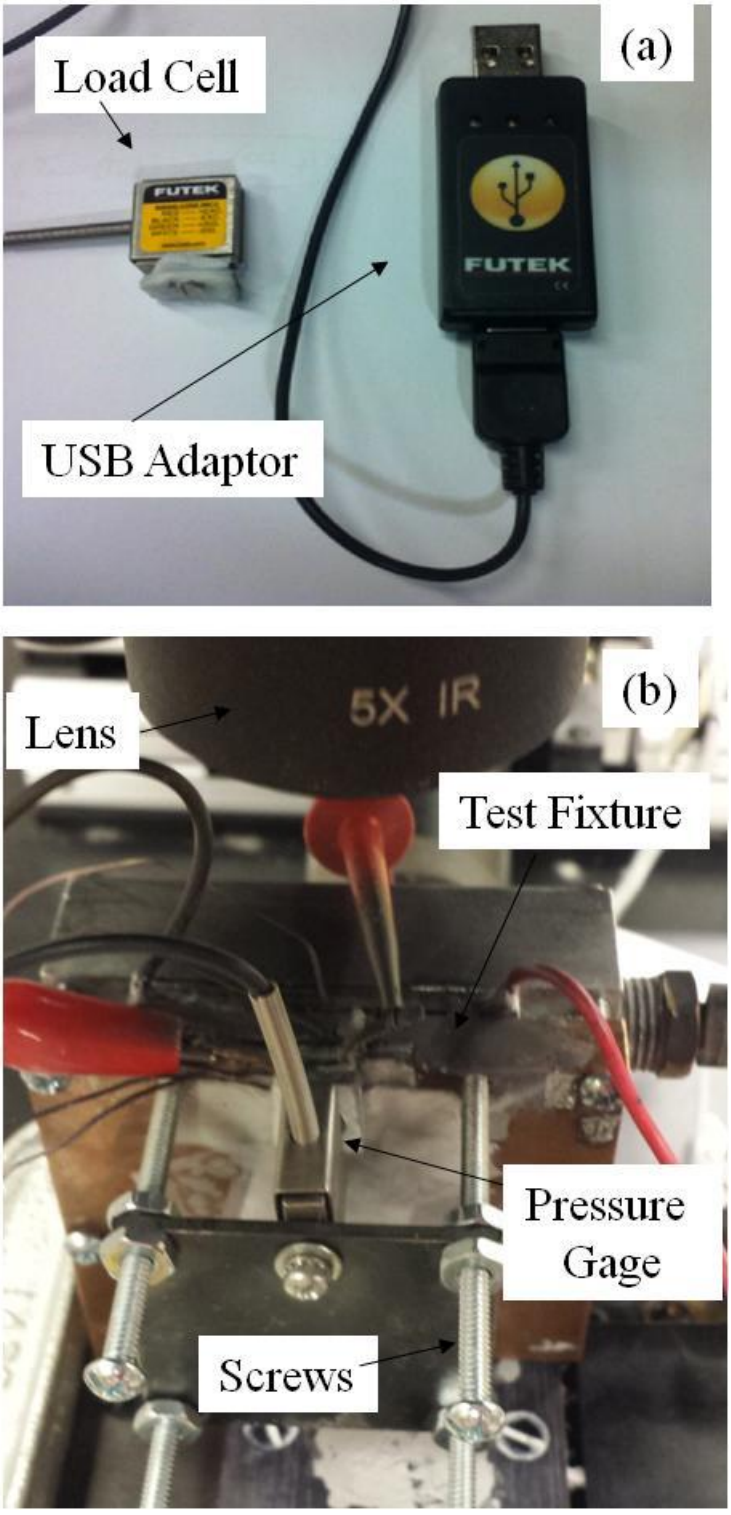

Figure 3.13 (a) Load cell used during pressure measurement of CNT based TIM and (b) Load cell positioned in series with the heater and sample

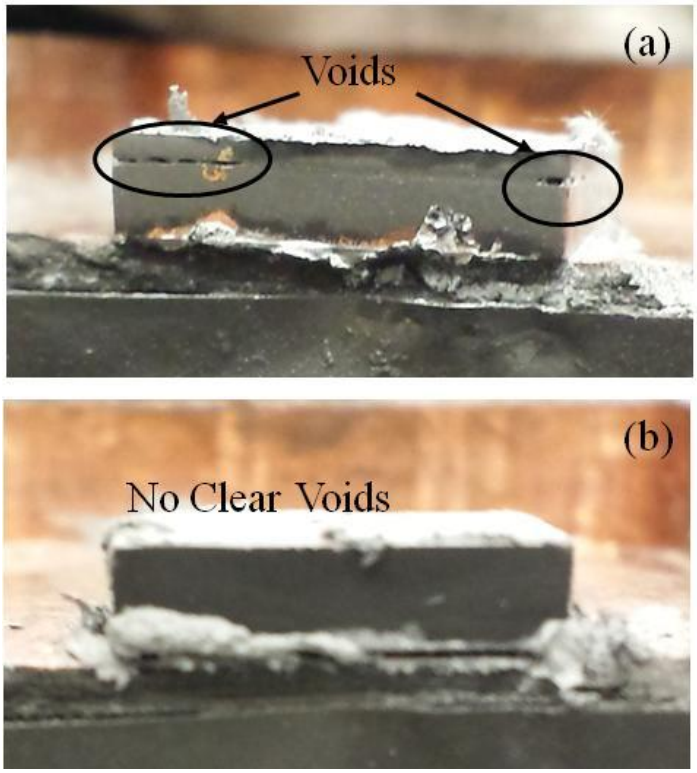

Figure 3.14 Edge photographs of (a) TCA pressure Sample 1 and (b) TCA pressure Sample 2

Figure 3.15 shows R''_{tot} for the three evaluated samples as a function of attachment. For the IR steady-state measurements described for TCA sample 2 and the Solder based attached sample there exists no clear relationship between the R''_{tot} and increased pressure. This would indicate that the tubes are well anchored. However, as shown for TCA sample 1, R''_{tot} does appear to have pressure dependence similar to that of the described in [102].

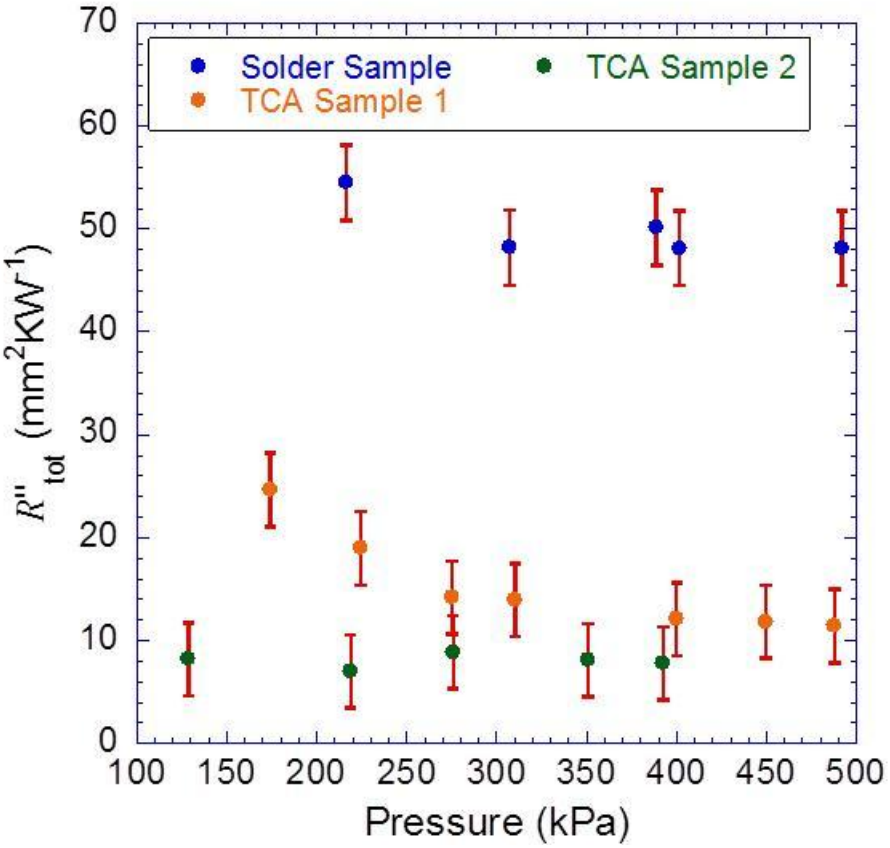

Figure 3.15 Pressure dependent study of the R''_{tot} of anchored VACNT arrays

3.7 Lateral Heat Conduction Through a VACNT Array

Due to the weak contact between neighboring tubes within a VACNT array it has generally been seen that the cross-plane conductivity is significantly higher than the in-plane conductivity, and there will be little lateral heat spreading. This behavior for an array is expected to be further exaggerated due to the low CNT volume fraction. Tong *et al.* , using a thermoreflectance measurement analyzed the k anisotropy ratio (k cross-plane vs. k in-plane) for a VACNT array grown on Si to be as high as 110 .[55] Through a laser flash measurement Ivanov evaluated the ratio to be as high as 80 for thicker VACNT arrays.[101].

The lateral heat spreading through a VACNT array is examined here using the IR microscope and a thermal test chip shown in Figure 3.16(a). The thermal test chips

(Thermal Engineering Associates) are 2.5 mm x 2.5 mm and comprised of two resistor heating elements connected in series, which are capable of providing 6 W of electric power each. There are also a set of thermal diodes which are positioned near the heaters but are not used in the experiments. The thermal test chips arrived in sets of 2 and due to the limited supply and potential damage to the die were remained attached as shown in Fig. 3.16(b) beneath an epoxy layer used to hold the heaters in place. The epoxy further provides stability to the wire bonded connections to the larger test board (Rockwell Collins). The larger test board was then attached to lead wires to a DC power supply (Xantrex).

The thermal test stage of the IR microscope was used to supply the heat for the reference temperature measurement shown in Fig 3.16(c). The board was attached to the

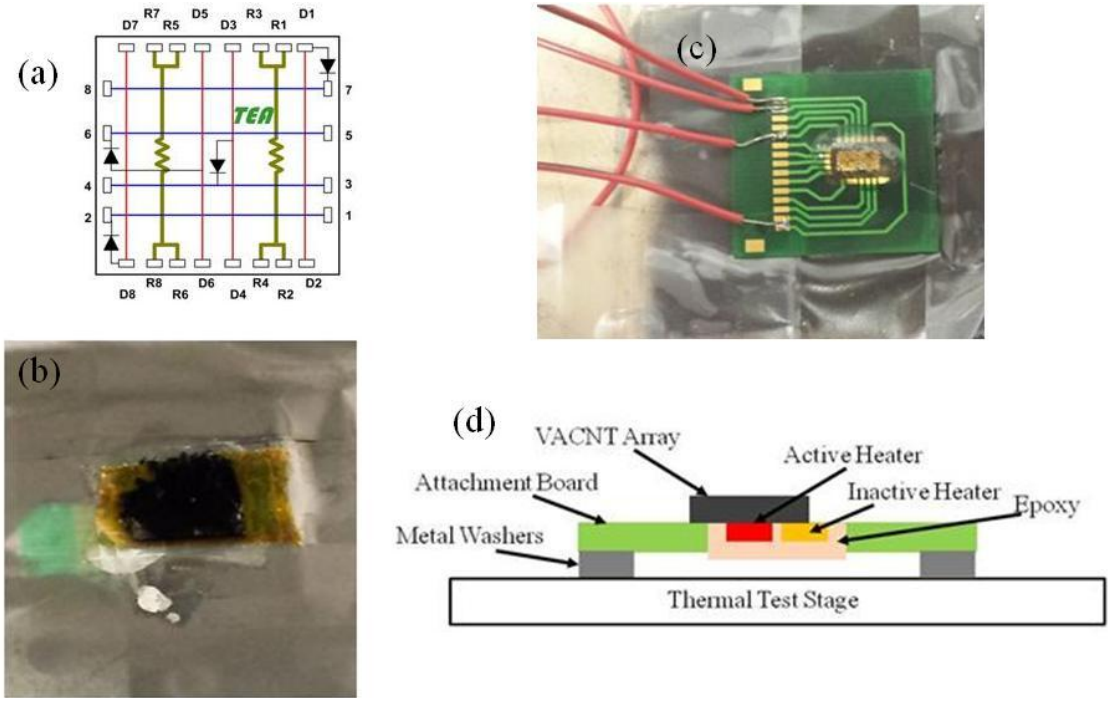

Figure 3.16 (a) Thermal test tie (Thermal Engineering Associates) (b) Two packaged thermal dies on thermal board (c) VACNT array on heater (d) Lateral heat spreading measurement test setup

thermal test stage through a set of metal washers and thermal grease. The full board was then taped to the test stage to limit motion during measurements. A Type-T thermocouple was used to determine the difference between the actual temperature of the heater and the test stage, and was used to set the reference temperature value for ε_λ mapping.

A VACNT sample (100 μm length) was prepared using the aforementioned fabrication technique and was removed from the growth Si substrate using a double sided adhesive. The thickness of the tape as measured using calipers was 400 μm. The other side of the tape was attached to the heater as shown in Fig. 3.16(d). In order to account for the lateral heat spreading a separate temperature mapping of the adhesive tape was done and is shown in Fig. 3.17(a). Due to the size of the heater multiple thermal mappings across the heater were made and were pieced together to generate a larger temperature map. The adhesive tape expectedly has a low thermal conductivity (<1 $\mathrm{W\,m^{-1}\,K^{-1}}$) and would limit spreading so the outline of the heater location is still well maintained. Figure 3.16(b) shows the IR temperature mapping of the powered VACNT sample using the thermal test chip. The heat flux applied through the heater was $6\ \mathrm{W\,cm^{-2}}$. A VACNT sample, which had an expectedly high cross-plane k but low anisotropy ratio would be expected to have a more uniform mapping than the one shown here.

A 3-dimensional COMSOL model was used to simulate the experiment to approximate the anisotropy ratio from the IR images. The Si heater pieces were modeled with one having a heat flux boundary condition to match that of the experiment. Convective heat flux and surface radiation with high conditions were considered on all other exposed areas. The resulting COMSOL model with a cross-plane $k = 150\ \mathrm{W\,m^{-1}\,K^{-1}}$ and in-plane $k = 2\ \mathrm{W\,m^{-1}\,K^{-1}}$ is shown in Fig. 3.17. The resulting anisotropy ratio of 75 is expected due to the poor interactions between the neighboring

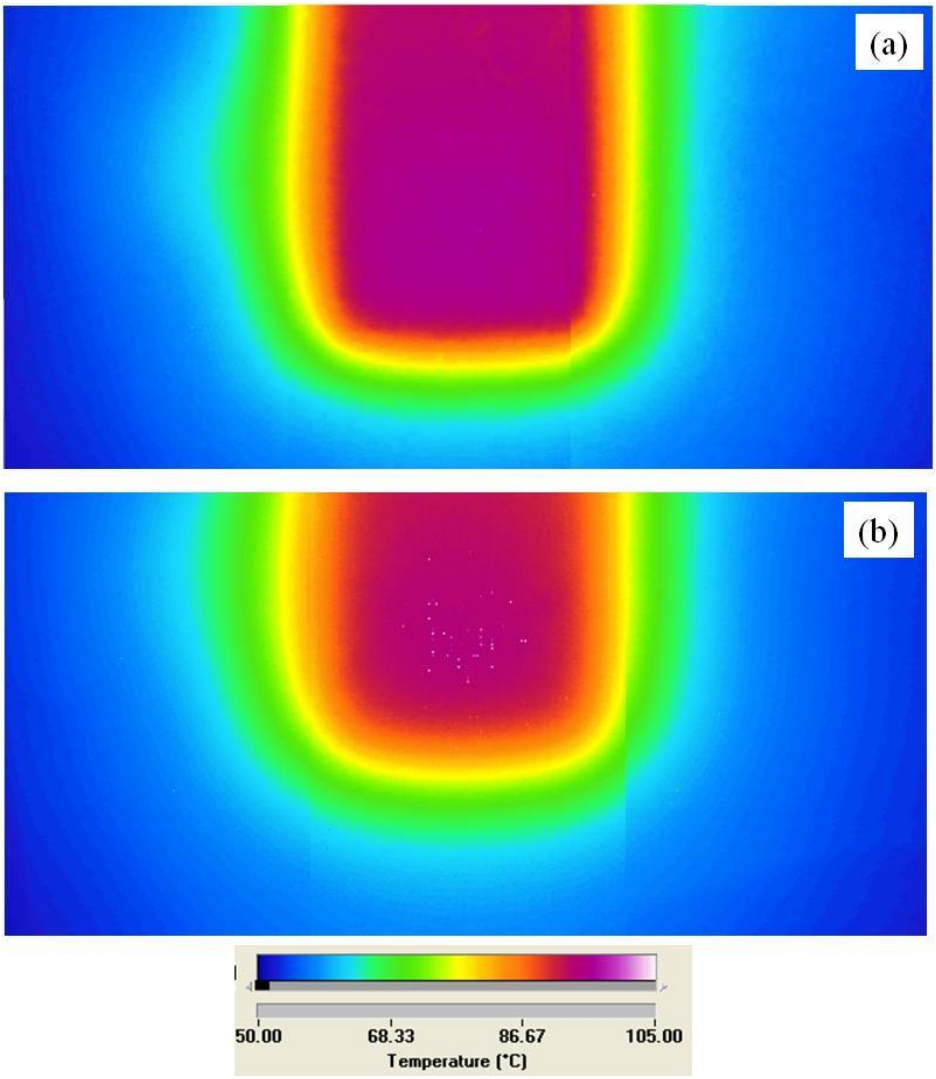

Figure 3.17 IR temperature mappings of (a) adhesive tape on heater (b) VACNT array attached through double sided adhesive tape

tubes.[4, 107] This clearly shows a one-dimensional behavior through array can be assumed with little lateral heat spreading

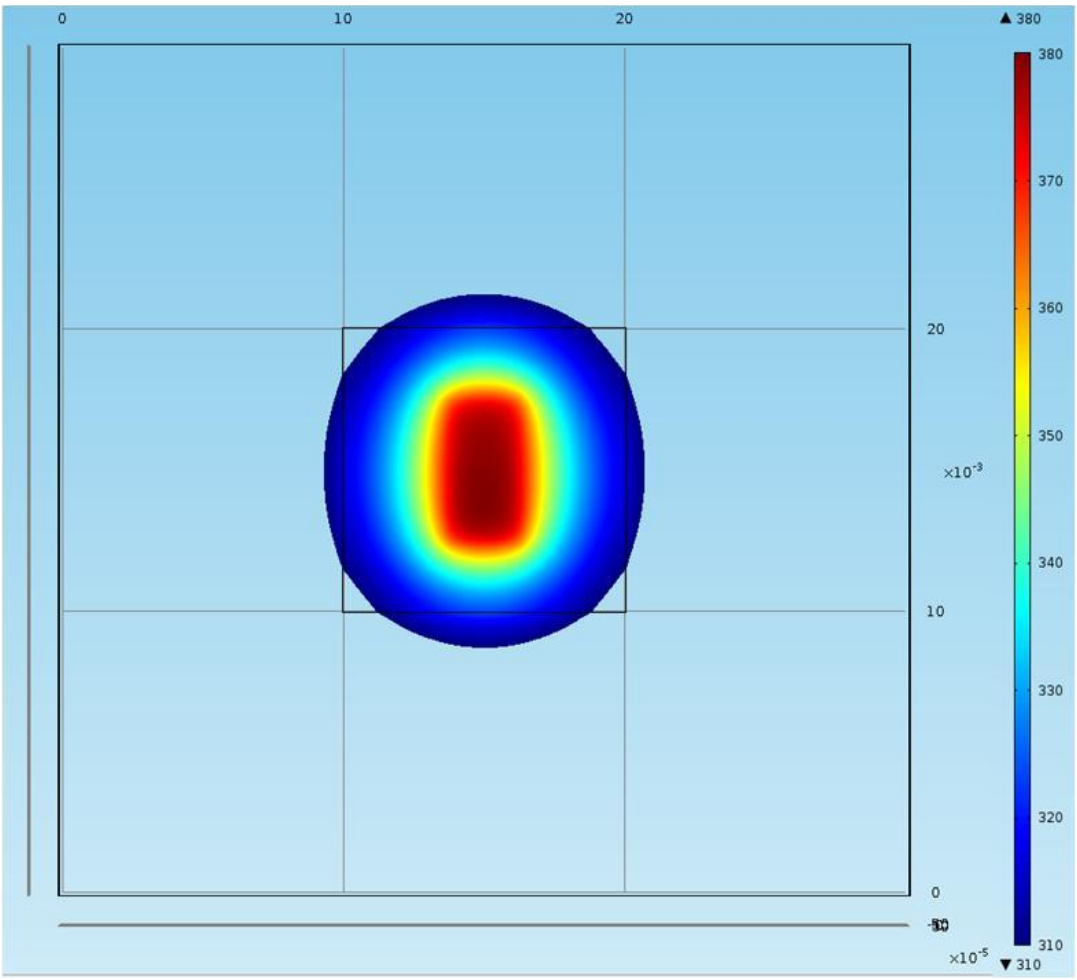

Figure 3.18 COMSOL model of VACNT array on heater

3.8 Conclusion

This chapter has presented work on the development of a steady-state IR measurement system for the purposes of measuring next generation TIM. The system was validated by the measuring of three commercial samples with R''_{tot} which were comparable to their reported values. Furthermore the experimental uncertainty associated with the measurement has been presented.

Due to the high growth temperatures associated with VACNT synthesis which is not compatible with CMOS processes a method of transferring the array from the growth substrate through a TCA and solder attachments has been demonstrated. The prepared

sample's R''_{tot} were measured using the steady-state IR measurement. The TCA bonded approach provided for the most consistent samples with well bonded samples below 10 mm^2 K W^{-1} which place them in the range of high end commercial TIM. It was shown that the primary source of the R''_{tot} could be attributed to the bonding interfaces with no clear relationship between R''_{tot} and VACNT array height. Furthermore the VANCT TIM samples were thermally cycled and aged to examine the effects of long term use. The VACNT arrays anchored using the TCA were shown to be quite resilient with the best performing TIM deteriorating by less than. 5%. Furthermore, increased quality of the VACNT as determined through Raman spectroscopic analysis, demonstrated improved R''_{tot} as compared to the lab grown CVD VACNT arrays showing that continued improvements to VACNT synthesis is still an important research focus.

The pressure dependence of the arrays were analyzed and unlike previous reports in literature non-bonded samples, the fully bonded VACNT arrays did not exhibit significant improvements in R''_{tot} with pressure. The VACNT TIM which had clear voids in the sample did increase in the same manner as previously reported measurements. Finally, the lateral heat spreading through a VACNT array was analyzed using a thermal test chip significantly smaller than the array.

CHAPTER 4

NUMERICAL MODEL OF THE THERMAL RESISTANCE OF CARBON NANOTUBES/THERMAL CONDUCTIVE ADHESIVE ANCHORED INTERFACE MATERIAL

As described in Chapter 3 the best performing VACNT anchored array was evident through the use of the TCA attachment and the best measured results of this method showed a minimum R''_{tot} of $\sim 4\,mm^2\,K\,W^{-1}$. A question regarding the future implementation of the this method is what is the minimum theoretically anticipated R''_{tot} through this anchoring technique. The present chapter describes steady-state computational modeling of the interface structure, and presents results as a function of TCA silver volume fraction, CNT filling fraction, TCA thickness, and CNT thermal conductivity. The initial section gives a general description of the method used for finding R''_{tot}. Following sections describe models associated with evaluating k_{eff} of a CNT-polymer composite and the thermal boundary resistances which are expected to contribute to the overall R''_{tot}. Finally a comparison of the computational results with the experimental steady-state IR measurements is discussed.

4.1 Steady-State Computation of R''_{tot} for a TCA Anchored VACNT Array

Figure 3.7(a) shows the sandwich structure of Cu-TCA-CNT-TCA-Si. The Si and Cu layers are used to simulate materials typically found in an electronic device package. As shown the CNT array is anchored to the substrate through the cured TCA. A steady-state finite-volume computational model with a linear solver is used to simulate a thermal load applied to the structure.[102] All simulations are made with the domain including base substrates of Cu and Si with 20 μm thickness, a VACNT array of 100 μm thickness,

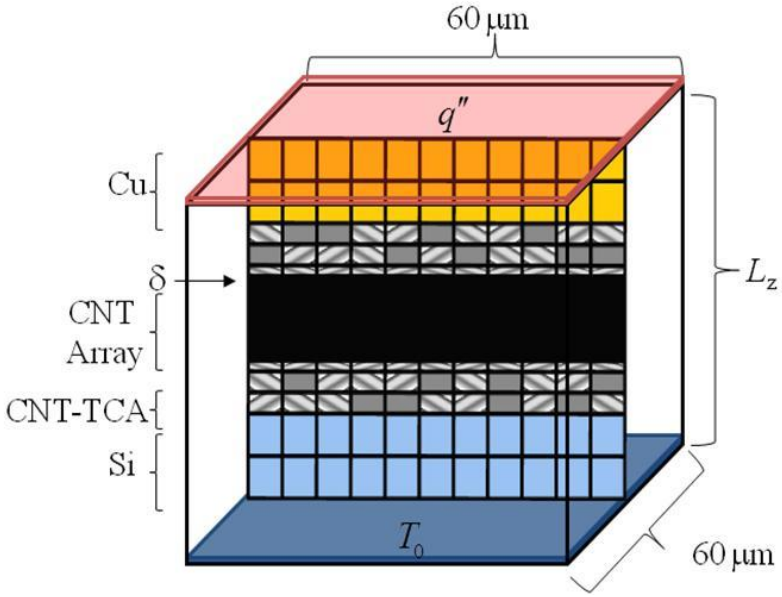

Figure 4.1. Adaptive meshing scheme used to highlight interfacial region

with width and depth of 60 μm for all materials as seen in Fig. 4.1. Using the model R''_{tot} ,of the sandwich structure can be evaluated by varying the volume fraction of filler particles within the TCA, *f*, the thickness of the TCA layer, *t*, and the packing density of the CNT array, φ . An adaptive meshing scheme was used to highlight the TCA interface, with each control volume being the size of an Ag particle (1.5 μm). Table 4.1 describes the materials used in the model, including k , phonon wave speeds (v_l, v_t) and atomic number density (n_a) of each material used to determine interfacial resistances. A heat flux boundary condition is supplied to one of the faces in the 3-dimensional model perpendicular to VACNT alignment, while the opposing face is given a constant temperature boundary condition. All other surfaces are treated as adiabatic. The k of the VACNT array was found through an equivalent parallel thermal resistance between air and an individual CNT at φ. Shown in Fig. 3.7(b), the ends of the CNT infiltrate the TCA composite, adding volume to the TCA region. While modeled as cubic structures in the

Table 4.1 Material properties for computational model [9, 19, 59, 60]

Material	k **(W m^{-1} K^{-1})**	v_l **(m s^{-1})**	v_t **(m s^{-1})**	n_a **(10^{28} m^{-3})**
Carbon Nanotube*	3,000	23,600	15,900	1.9 x 10^{19}**
Copper	400	4,910	2,500	8.45
Polymer	0.2	1,950	540	12.2
Silicon	140	8,970	5,332	5
Silver	429	3,780	1,740	5.85

*Carbon nanotube conductivity and wave speeds taken along basal plane
**Carbon nanotube planar point density in graphite, m^{-2}

control volume analysis, the Ag particles, as seen in Fig. 3.7(b), are spherical shaped, allowing for the CNT array to more easily bend around the particles.

Assuming that the array penetration volume can be as thick as the two sided adhesives used, the total thickness to the TCA region with the presence of the infiltrating CNT array is

$$t_1 = (1+\varphi)t \tag{4.1}$$

It is assumed that the top newly formed region of thickness δ is a polymer-CNT composite material as seen in the highlighted regions of Fig. 4.3. For a scenario in which the packing density of CNT within δ and t regions are the same, the packing density of CNT is given as $\varphi' = \varphi/(1+\varphi)$. The volume fraction of polymer in δ and t regions are then $1-\varphi'$ and $1-\varphi'-f$ respectively, where f is the volume fraction of Ag in the TCA layer. This assumption is reasonable for thin TCA layers; however, as t increases, full CNT infiltration within the TCA may not be possible. Furthermore, it is assumed that the CNT array does not displace the original Ag particles.

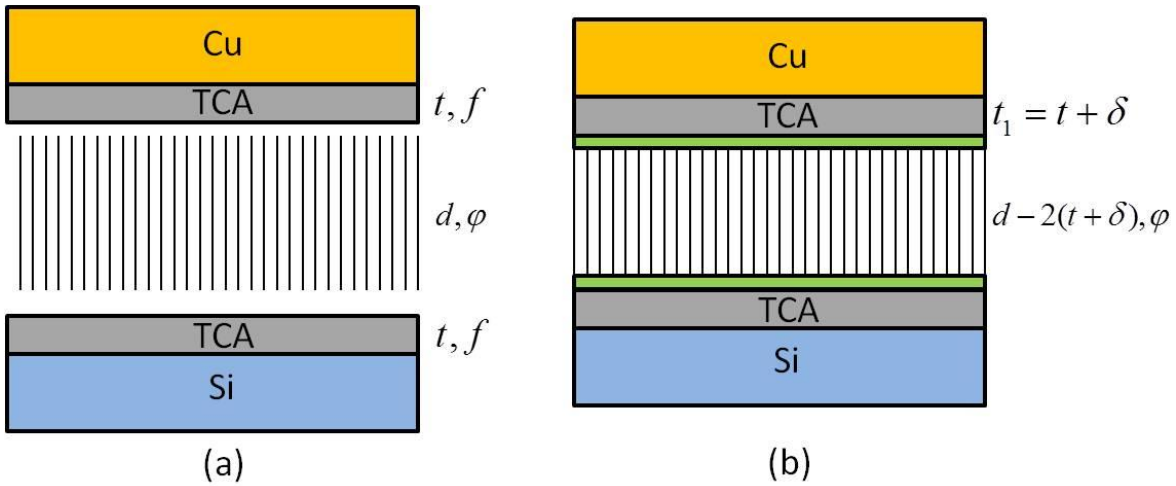

Figure 4.2. (a) Image indicating interface structure prior to CNT-TCA infiltration (b) Image indicating final structure

4.2 Effective Thermal Conductivity of a CNT-Polymer Composite Material

For the model a generalized Bruggemann effective medium theory model was used to determine the k_{eff} of the CNT/polymer composite regions. The following will briefly describe the model According to the average polarization theory, the k_{eff} of CNT composites is found by the definition [103]

$$\langle q'' \rangle = k_{\text{eff}} \langle \nabla T \rangle \tag{4.2}$$

Where $\langle \cdots \rangle$ denotes an average over the system volume. To find the k_{eff} the distribution of heat flux in the system when a temperature field is applied is needed. The internal intensity H, of CNTs and matrix particles averaged over all orientations are equal

$$H = \sum_{i=x,y,z} \frac{1}{1 + B_{\text{CNT},j}(k_{\text{CNT},k} - k_{\text{eff},k})/k_{\text{CNT},j}} H_0 \tag{4.3a}$$

$$H = \sum_{i=x,y,z} \frac{1}{1 + B_{m,j}(k_{m,k} - k_{\text{eff},k})/k_{m,j}} H_0 \tag{4.3b}$$

where $B_{m,j}$ and $B_{\text{CNT},j}$ are the depolarization factors which are determined by the shape of the matrix particles and CNTs along the j axis (j=x,y,z) respectively. Substituting this into Eqn. (4.2) an equation for the k of the composite is obtained.

$$\sum_{j=x,y,z}(1-\varphi')\frac{k_{\text{eff},j}-k_{m,j}}{k_{\text{eff},j}+B_{m,j}(k_{m,j}-k_{\text{eff},j})}+\sum_{j=x,y,z}\varphi'\frac{k_{\text{eff},j}-k_{\text{CNT},j}}{k_{\text{eff},j}+B_{\text{CNT},j}(k_{\text{CNT},j}-k_{\text{eff},j})}=0 \quad (4.4)$$

In this model it is assumed that the matrix particles maybe treated as spherical particles while the CNTs are taken as elongated spheroids. For the matrix particles the polarization factor is

$$B_{m,x}=B_{m,y}=B_{m,z}=1/3 \quad (4.5)$$

Substituting Eqn. (4.5), Eqn. (4.4) may be written as

$$(1-\varphi')\frac{k_{\text{eff}}-k_m}{2k_{\text{eff}}+k_m}+\frac{\varphi'}{9}\sum_{j=x,y,z}\frac{k_{\text{eff}}-k_{\text{CNT},j}}{k_{\text{eff}}+B_{\text{CNT},j}(k_{\text{CNT},j}-k_{\text{eff}})}=0 \quad (4.6)$$

The CNTs are considered here have a large aspect ratio $p=L/d\gg 1$, where L and d are the nanotubes length and diameter respectively resulting in the depolarization factor being given as

$$B_{\text{CNT},x}=\frac{\ln(p+\sqrt{p^2-1})p}{(p^2-1)^{3/2}}+\frac{1}{1-p^2} \quad (4.7a)$$

$$B_{\text{CNT},y}=B_{\text{CNT},z}=\frac{1-B_{\text{CNT},x}}{2} \quad (4.7b)$$

Figure 4.3(a) shows the polarization factors as a function of the aspect ratio. As shown for very large aspect ratios as are expected with CNT, $B_{\text{CNT},x}$ decays very quickly while $B_{\text{CNT},y}$ and $B_{\text{CNT},z}$ approach $1/2$. Substituting Eqns. (4.7) into Eqn. (4.6) for CNT with large aspect ratios the relation for k_{eff} of CNT can be approximated as

$$(1-\varphi')\frac{k_{\text{eff}}-k_m}{2k_{\text{eff}}+k_m}+\left(\frac{\varphi'}{9}\right)\frac{k_{\text{eff}}-k_{\text{CNT}}}{k_{\text{eff}}}=0 \quad (4.8)$$

Eqn. (4.8) is plotted in the Fig. 4.3(b) as can be seen at high aspect ratio as is expected for CNTs the depolarization factor takes a smaller value leading to an important factor in the evaluation of the k_{eff}.

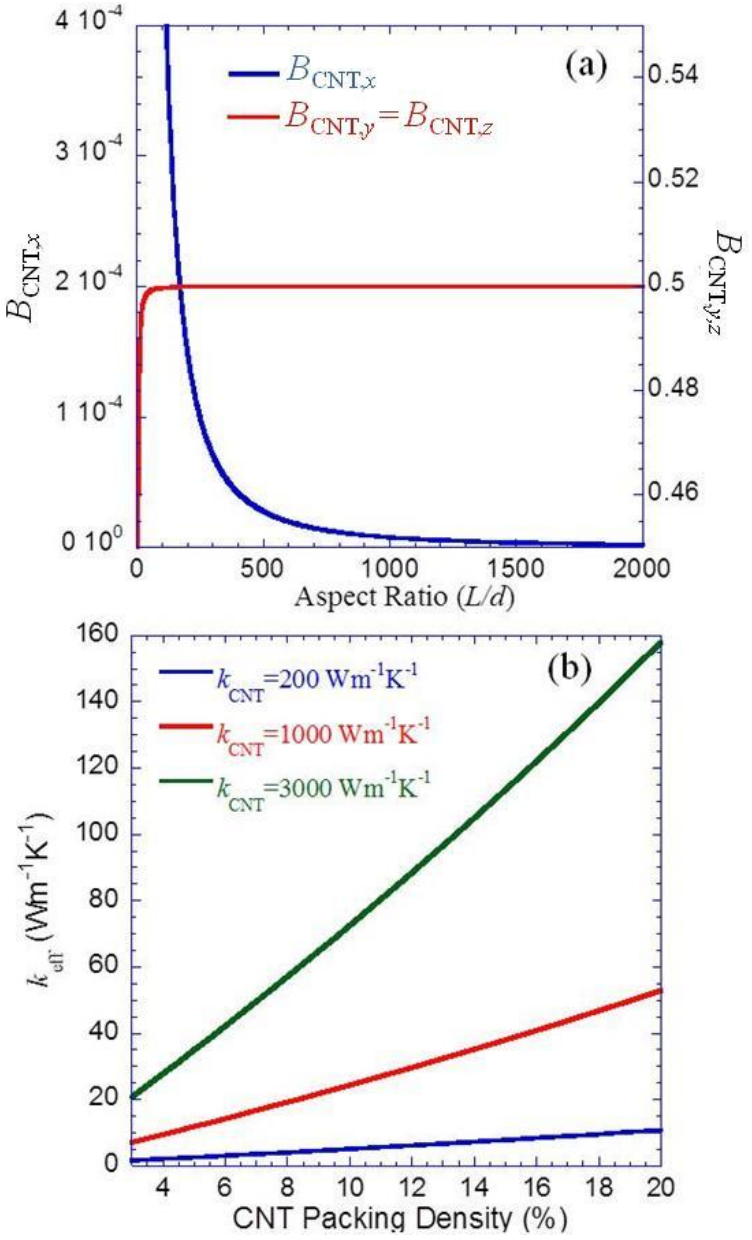

Figure 4.3 (a) Depolarization factors for base CNT (b) Effective medium calculation of k_{eff} of a polymer/CNT composite

4.3 Thermal Boundary Conductance

The thermal boundary conductance at all relevant interfaces are accounted for within the computation domain. It is assumed that the tips of the nanotubes are in contact with the opposing material. The thermal boundary conductance for the CNTs is taken to be the sum of the ballistic and diffusive contributions.[56, 58] The efficiency of the

thermal transport across the boundary is known to be a function of the condition of the interface in addition to the relevant vibrational spectra between the two surfaces. The number of faces which could be contacted by the CNT in a random arrangement as compared to a vertical orientation is used to determine the percent of CNT contacting on each face. The models adopted here assume perfect contact between surfaces such that the thermal transmission across the interface is only a function of either phonon vibration properties for nonmetallic interfaces or electronic properties for metallic interfaces.

A benefit of the proposed adhesion method is that the bond between CNT and the opposing substrates is expected to be more secure than the weaker van der Walls contact. Tong *et al.* measured the contact resistance of the CVD grown CNT array on an Si substrate, in addition to the resistance of an array in van der Walls contact with a glass substrate.[55] Due to weak surface adhesion it was found that the van der Walls contact had approximately an order of magnitude higher thermal resistance than the as grown surface. A metallic adhesion layer was used to promote contact with the glass substrate decreasing the overall thermal resistance. The presence of the TCA layer is expected to display similar behavior.

4.3.1 CNT/Solid Thermal Boundary Conductance

Interfacial resistance between the VACNT array and relevant solids is also considered (i.e. Ag, Cu, and Si). It is assumed that the tips of the nanotubes are in contact with the opposing material with the polymer anchoring them in place. The diffusive constriction resistance is modeled as a circular area on the boundary of a semi-infinite medium. This is used since the contact area is small compared to the other dimensions for low filling ratio of CNT. The constriction resistance is given as

$$R''_{\mathrm{d}} = \frac{\pi d}{8k_{\mathrm{sub}}} \tag{4.9}$$

where k_{sub} is the thermal conductivity of the opposing substrate. In the completely ballistic limit, thermal transport is a function of the transmission of phonons from one material to the other. It is known that in metals, electrons are dominate heat transport carriers while in CNT, as has been discussed. the primary method of transport is through phonons.[19] According to Majumdar and Reddy, for a metal in contact with a non-metal there is first an electron-phonon interaction within the metal followed by a phonon-phonon interaction at the interface.[104]. Majumdar and Reddy characterized this interaction and gave an expression for the interface conductance, h_{m-n}, as

$$h_{m-n} = \frac{k_p \sqrt{\frac{G_{ep}}{k_{hm}}}}{\left[1 + \frac{k_p}{h_{pp}} \sqrt{\frac{G}{k_{hm}} - \frac{k_{hm}}{k_e}}\right]} \tag{4.10}$$

where k_p and k_e are the phonon and electron thermal conductivities within the metal respectively, G_{ep} is the electron to phonon energy transfer per unit volume, h_{pp} is the phonon-phonon conductance between the metal and non-metal, and k_{hm} is as the harmonic mean of the k_e and k_p. For metals generally $k_e \gg k_p$ such that $k_{hm} \approx k_p$ In this case Eqn. (4.10) may be written as

$$h_{m-n} = \frac{h_{pp} \sqrt{G_{ep} k_p}}{h_{pp} + \sqrt{G_{ep} k_p}} \tag{4.11}$$

The k_p of the metal can be taken from kinetic theory as[19]

$$k_p = \frac{1}{3} C_p v_a \Lambda_p \tag{4.12}$$

C_p is the lattice heat capacity, v_a is the average acoustic speed within the lattice, and Λ_p is the phonon mean free path. The mean free path, Λ_p, is a function of phonon-phonon scattering and phonon-defect scattering. As temperature of a material increases phonon-

phonon scattering increases (Umklapp scattering) thereby decreasing the mean free path. At low temperatures, scattering on defects is the limiting factor to the mean free path. It will be assumed in calculations that the Λ_p is ~5nm at near room temperatures but this value will greatly vary at lower temperatures [5]. The energy of a phonon is given by

$$\varepsilon = \hbar\omega \tag{4.13}$$

where ω is the angular frequency. Here a linear dispersion relation will be used to find the specific heat such that the relation between the wavevector, q and ω is given as

$$\omega = v_a q \tag{4.14}$$

where is the average speed of the longitudinal speeds, v_l, and transverse acoustic speeds v_t given as

$$v_a^3 = 3/(v_l^{-3} + 2v_t^{-3}) \tag{4.15}$$

These speeds for the materials considered here are given in Table. 4.1. The expectation of the number of phonons in a state with a given energy, ε, is given by the Bose Einstein distribution function, f_{BE}, given by

$$f_{\mathrm{BE}}(\omega, T) = \frac{1}{\exp\left((h\omega)/(k_{\mathrm{B}}T)\right) - 1} \tag{4.16}$$

In the 3-D reciprocal lattice space, the volume *V* allowed for each q is given as

$$\left(\frac{2\pi}{L}\right)^3 = \frac{8\pi^3}{V} \tag{4.17}$$

and the number of allowed modes, *N*, is found confined within a sphere of radius q_D is given as

$$N = \frac{V q_D{}^3}{6\pi^2} \tag{4.18}$$

The 3-D density of states is given as

$$D(\omega) = \frac{1}{V}\frac{dN}{d\omega} = \frac{\omega^2}{2\pi {v_a}^3} \tag{4.19}$$

The lattice specific heat is given as

$$c_p(T) = 3MR\int_0^{\omega_D} \hbar\omega D(\omega)\frac{\partial f_{BE}(\omega,T)}{\partial T}d\omega \tag{4.20}$$

The electron to phonon energy transfer per unit volume, G_{ep}, is given as

$$G_{ep} = \frac{\pi^4 (n_e v_a k_B)^2}{18k} \tag{4.21}$$

where k is taken as the effective conductivity of the metal.

The final term to be analyzed in Eqns. (4.10) and (4.11) is the phonon-phonon interaction between the metal and the nonmetal. For an ensemble of phonons which are incident on the surface the h_{pp} is given by [59]

$$h_{pp} = \frac{1}{2}\int_0^{\pi/2}\left[\sum_j \int_0^{\omega_{c,j}} \hbar\omega v_j(\omega)\alpha_{j,1\to 2}(\omega,\mu)D_j(\omega)\frac{\partial f(\omega,T)}{\partial T}\partial\omega\right]\cos(\theta)\sin(\theta)\mathrm{d}\theta \tag{4.22}$$

where $\alpha_{1\to 2}$ is the phonon transmissivity between mediums 1 and 2. The primary issue in finding h_{pp} is correctly representing $\alpha_{1\to 2}$ which varies for different approaches. For calculating this generally two methods are used, the acoustic mismatch model (AMM), and the diffuse mismatch model (DMM).[59] In the AMM, phonon transmission at an interface is due to relative mismatch in properties of the material as well as transmission direction. This model is typically used at low temperatures where phonon wavelengths are low. Furthermore the model is a completely specular model which is applicable when the phonon wavelength is greater than interface roughness. As a result the model is applicable at low temperatures for smooth interfaces. In the DMM it is assumed all phonon scattering is diffuse, meaning that the angle of the transmitted or reflected phonon and its polarization have no relation to the incident phonon. This assumption is generally reasonable at high temperatures where the average phonon wavelength

approaches the length scale of atomic roughness. For two isotropic materials using the DMM the $\alpha_{1\to 2}$ is given by

$$\alpha_{1\to 2}(\omega) = \frac{\sum_j v_{2,j} D_{2,j}}{\sum_j v_{1,j} D_{1,j} + \sum_j v_{1,j} D_{1,j}} \tag{4.23}$$

These two models, AMM and DMM provide upper and lower limits for considering elastic phonon scattering in which the phonon frequency is conserved. Additional advances to the DMM have included accounting for full dispersion, interface disorder, and inelastic scattering. Furthermore Duda *et al.*. described a model based on the diffuse mismatch model between an isotropic material and a material of extreme elastic anisotropy.[60] This is clearly applicable for CNT and graphite in which the *k* along the a-axis (tube length) vs. c-axis (perpendicular to the tube length) can vary by up to 3 orders of magnitude. For graphite the interaction between monolayers can be described as a van der Walls interactions. As a result of this weak interaction an effective density of states can be used to describe the bulk graphite. For the development of a phonon-phonon conductance between graphitic materials one can consider a single layer of graphite described by a two dimensional density of states then becomes

$$D_{\text{eff}}(\omega) = \frac{\omega}{2\pi v^2 d} \tag{4.24}$$

where *d* is the monolayer spacing between layers of graphite *d*=3.55 A.

After substituting in Eqn. (4.23) into Eqn. (4.22) and assuming diffusive transport. The h_{pp} in graphite perpendicular direction to the interface is given by the DMM as

$$h_{pp} = \frac{1}{4}\sum_j^3 \int_0^{\omega_{\max,j}} \alpha_{1-2} \hbar \omega v_{1,j} D_1(\omega, v_{1,j}) \frac{df}{dT} d\omega \tag{4.25}$$

The elastic phonon transmission coefficient, $\alpha_{1-2,e}(\omega)$,as given by the development of the DMM for an energy balance on each phonon frequency is given as

$$\hbar\omega D_1(\omega, v_{1,j}) f(\omega)\alpha_{1-2,e}(\omega) = \hbar\omega D_{\text{eff}}(\omega, v_{1,j}) f(\omega)\alpha_{2-1,e}(\omega) \tag{4.26}$$

By assuming a completely diffusive scattering (i.e. $\alpha_{1-2,e}(\omega) = 1 - \alpha_{2-1,e}(\omega)$) an expression for $\alpha_{1-2,e}(\omega)$ can be found. Duda *et al.*. further suggested that multiple phonon processes should be considered. In this model decay of high energy phonon at frequency $n\omega$ into *n* lower energy phonons each at a frequency ω . The maximum vibrational frequencies in metals are typically less than 10 THz, while the maximum vibrational frequency of CNT is over 48 THz.[105] This large mismatch opens up the potential for inelastic phonon–phonon processes contributing to phonon thermal transport across solid-graphite interfaces. After full substitution Eqn. (4.10) is plotted in Fig. 4.5(a) as a function of interface temperature.

4.3.2 Thermal Boundary Conductance Between Ag/Cu

Through an extension of the thermal transport through phonon across an interface, Gundrum *et al.*. [106] described thermal transport across a metal interface and compared results to conductance measurements made through thermoreflectance measurement. In the numerical model used to simulate this novel VACNT TIM material the metal/metal thermal boundary conductance between Cu/Ag interfaces. Electrons, which are the primary heat carrier in metals were assumes to scatter diffusely and elastically at the interface similar to the basis of the DMM model described earlier. The transmission coefficient between 2 metallic mediums, Γ_{1-2}, under this extended model is given as

$$\Gamma_{1-2}(E) = \int_0^{\pi/2} \frac{v_2(E)D_2(E)}{v_1(E)D_1(E) + v_2(E)D_2(E)} \cos(\theta)\sin(\theta)d\theta \tag{4.27}$$

Table 4.2 Electronic Properties of Ag and Cu [19]

Material	μ_F (eV)	n_e (10^{28} m^{-3})	M (kg $kmol^{-1}$)
Ag	5.51	5.85	108
Cu	7	8.45	63.5

Further development with a degenerate metal with an isotropic Fermi surface leads to the thermal conductance between metallic surfaces, h_{m-m}, of [106]

$$h_{m-m} = \frac{1}{2} v_1(E_F)\Gamma_1(E_F)\int_0^\infty E \frac{dN_1(E,T)}{dT} dE \tag{4.28}$$

where $N_1(E,T)$ is the product of the density of states of free electrons the Fermi-Dirac distribution function

$$N_1(E,T) = 4\pi\left(\frac{2m_e}{h^2}\right)^{3/2} \frac{\sqrt{E}}{\exp\left((E-\mu_F)/k_B T\right)+1} \tag{4.29}$$

The integral in Eqn. (4.28) is the same for determination of the electronic heat capacity per unit volume C_e. . High thermal conductance values for metallic surfaces have been observed experimentally between aluminum and Cu 4 GW m^{-2} K^{-1} at room temperature.[106] Figure 4.4 shows the calculated conductance across an Ag/Cu interface. As anticipated the electron based interfacial conductance yields the large value. The interfacial conductance at larger temperatures is limited by the electron-phonon energy transfer rate which scales with the inverse of *k* which generally increases linearly.

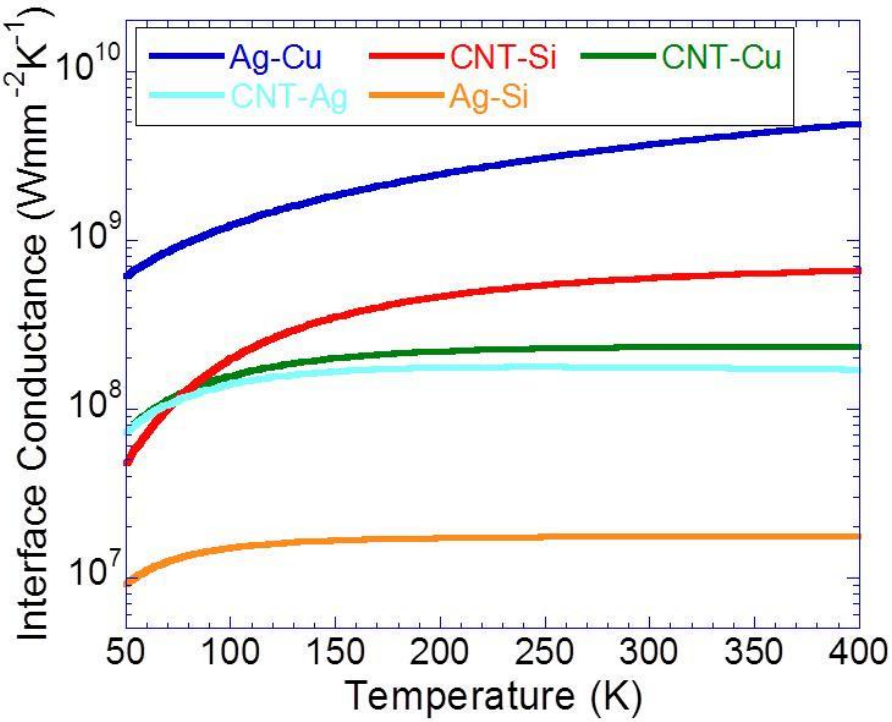

Figure 4.4 Interfacial thermal conductance between contacting surfaces in the numerical model

4.4 Numerical Results

In order to evaluate the R''_{tot} for each parametric test the steady-state differential equation

$$\frac{\partial}{\partial x}\left(k\frac{\partial T}{\partial x}\right)+\frac{\partial}{\partial y}\left(k\frac{\partial T}{\partial y}\right)+\frac{\partial}{\partial z}\left(k\frac{\partial T}{\partial z}\right)=0 \tag{4.30}$$

is transformed into a system of discretization equations of the form [102]

$$a_p T_p = a_E T_E + a_W T_W + a_N T_N + a_S T_S + a_F T_F + a_B T_B \tag{4.31}$$

where $E,\ W,\ N,\ S,\ B,\ F$ correspond neighboring control volumes of control volume P and a_i (where $i = E,\ W,\ N,\ S,\ F,\ B$) is the effective interfacial resistance

including the intrinsic k resistances and interfacial resistances, multiplied by the differential area of each contacting face and

$$a_p = \sum_i a_i \tag{4.32}$$

Boundary conditions including, constant boundary temperatures, adiabatic boundaries constant heat flux conditions can found by modifying a_i accordingly.

A 3D k matrix can be recalled upon evaluating a_i for each control volume. Fig. 4.5(a) shows an example of the mid-plane k matrix used in the parametric study. As can be seen the Ag, Si, Cu volumes are given a constant k according to Table 4.1 and the k of the CNT array was determined through $k_{\text{Array}} = \varphi k_{\text{CNT}}$. The k_{eff} of the CNT/polymer composite found within the t and δ regions is through Eqn. (4.8). After populating the a_i matrix the temperature distribution is found through matrix multiplication. A corresponding temperature distribution represented by Fig. 4.5(b) is generated. The boundary in which q'' is applied is applied being the bottom surface results in the highest temperatures. The R''_{tot} for the model is given by

$$R''_{\text{tot}} = \frac{\left(\frac{1}{n^2}\sum_{i,j} T(i,j,1)\right) - T_0}{q''} \tag{4.33}$$

where n is the number of control volumes in the x and y directions and $T(i,j,1)$ is the boundary in which q'' is applied.

Figure 4.6 shows the modeled thermal resistance at different Ag volume fractions $f = 40\% - 60\%$. As shown the lowest calculated resistance for a fixed φ and f is expected when the thickness of the TCA layer is minimized. The combined effects of the low k_{eff} over a small distance and a significant

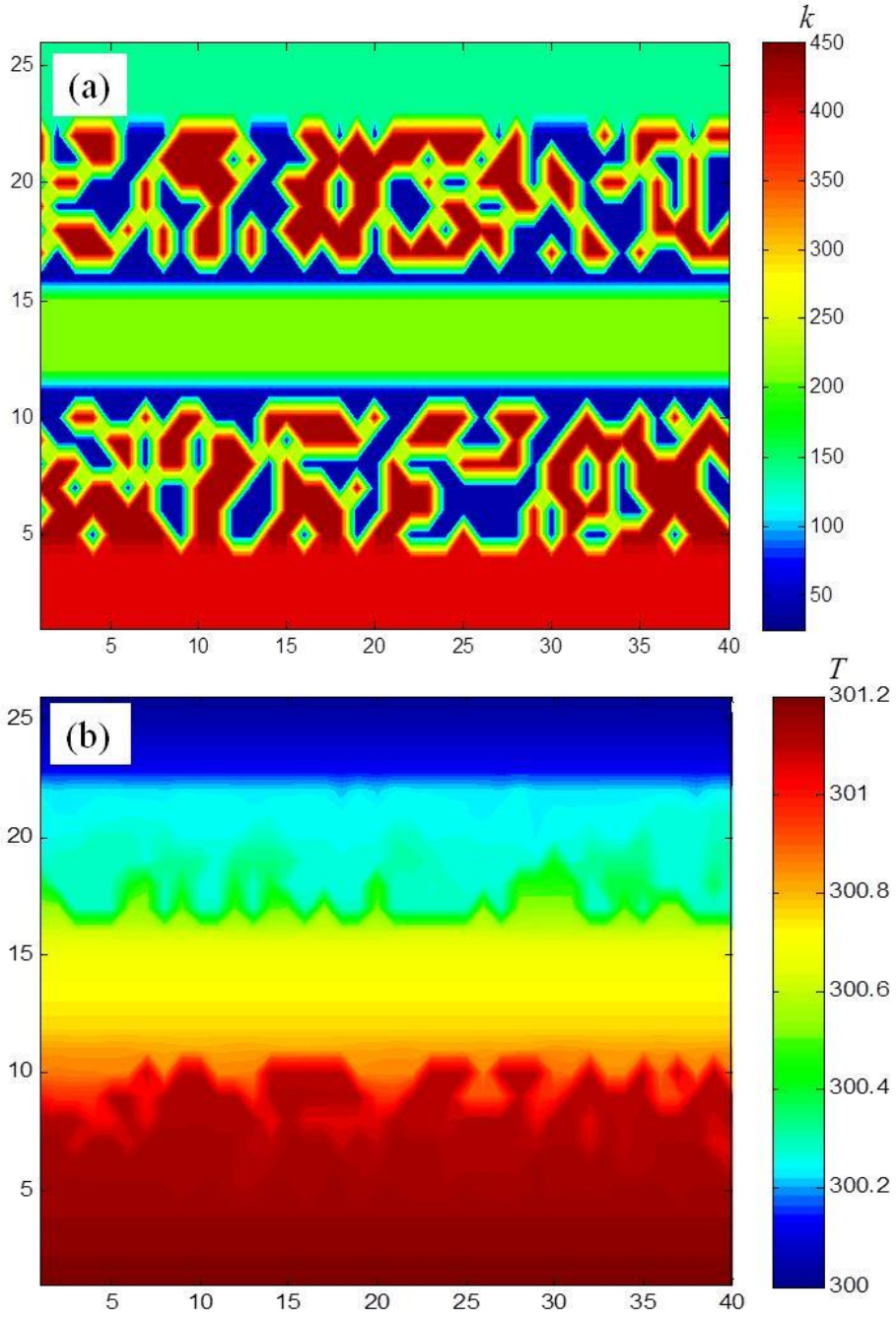

Figure 4.5 (a) Thermal conductivity matrix (in $\mathrm{W\ m^{-1}\ K^{-1}}$) (b) Temperature distribution (in K) based on the aforementioned conditions and boundary resistances used to determine R''_{tot}

portion of the full array penetrating through t_1 lead to this minimization. Furthermore for low t (< 3 μm) the lowest calculated resistances occur at $f = 40\%$ at fixed φ. At this

level since there are fewer Ag boundaries which would need to be overcome by the array a network of percolating Ag particles would not be expected to reduce resistance. Also since an increased φ leads to a higher composite conductivity the lowest calculated resistance is given at $f = 40\%$ and $\varphi = 20\%$ with a value of 0.39 mm^2 K W^{-1} which is significantly better than other commercially available interface materials. However, due to the low t_1, this configuration may lead to poor adhesion strength between the TCA and the array. At larger t, the presence of an Ag percolation network becomes more evident. It is clearly seen that at fixed f and φ there is a trend of increasing R''_{tot} with increasing t. Figure 4.6 further demonstrates that at larger φ the rate of increase in R''_{tot} is generally lessened as t increases. Due to the large thermal conductivity for the Ag fillers, fully percolating networks at larger f assist in the thermal transport and the influence of component resistances related to interfaces is lessened due to the larger intrinsic resistances associated with the thicker composite regions. However, comparing Fig. 4.6(b) and 4.6(c) the increased number of interfaces and associated thermal resistances can still lead to larger R''_{tot} at higher f. This is particularly evident at low φ. As k_{eff} increases with greater φ, the role of the interfacial resistances is lessened and the R''_{tot} is expected to be lower for larger f. This would then be of interest if control of thickness of the TCA layer is difficult to maintain.

Figure 4.7 demonstrates the effect of altering the CNT density at a fixed $f = 60\%$. These are shown in contour plot in Fig. 4.6(c). As shown in Fig, 4.3(b), k_{eff} is expected to scale almost linearly with φ The change in R''_{tot}, however, does not follow

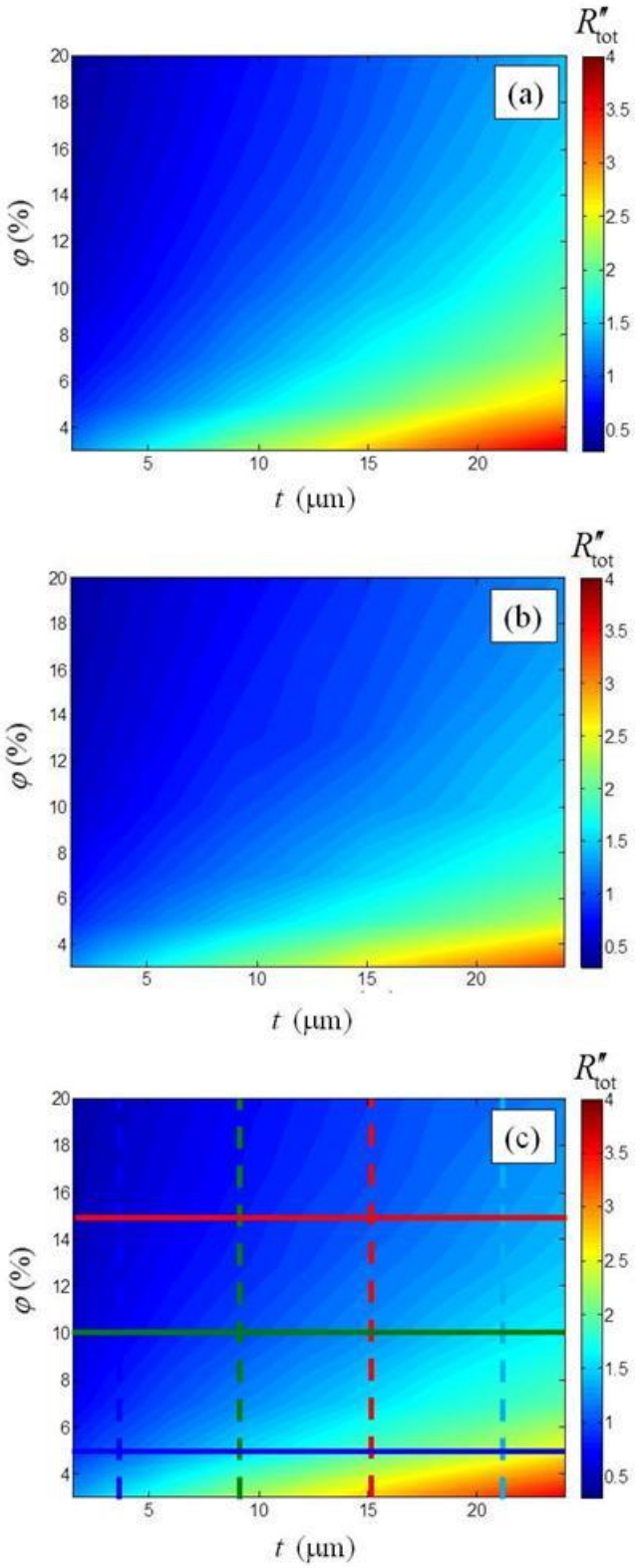

Figure. 4.6. Parametric study of various interfaces for VACNT-TCA attachment schemes with contours showing R''_{tot} (in $mm^2\ K\ W^{-1}$) calculated at room temperature for (a) $f = 40\%$ (b) $f = 50\%$ (c) $f = 60\%$ with $k_{CNT} = 3,000\ W\ m^{-1}\ K^{-1}$

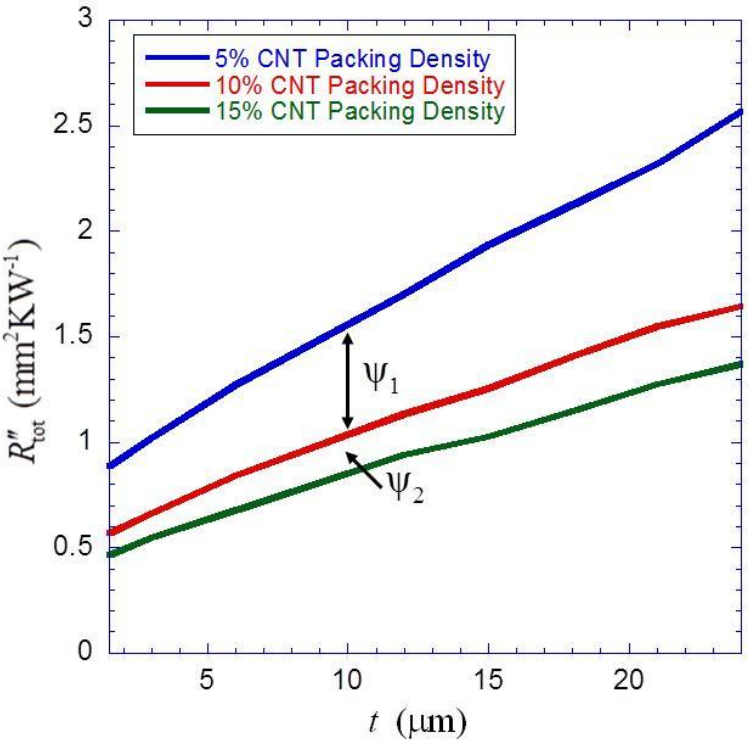

Figure 4.7. R''_{tot} (mm^2 K W^{-1}) across VACNT based TIM for 60% Vol. Ag with $k_{CNT} = 3{,}000$ W m^{-1} K^{-1} Through lines from Fig 4.6(c) showing variation of R''_{tot} at different CNT densities

this general trend. For the change between $\varphi = 5\%$ and $\varphi = 10\%$, as shown as ψ_1, and ψ_2 between $\varphi = 10\%$ and $\varphi = 15\%$ the benefit of increased CNT array densification is diminished. Since k_{eff} is expectedly low at small φ, networks of percolating Ag particles are of increased benefit. As φ is further increased, the CNT-polymer matrix itself becomes a good thermal conductor and would expectedly reduce the expected benefit of the Ag particles. Currently the majority of CNT arrays are produced such that the $\varphi < 10\%$ in which case the use of Ag fillers as supporting conductive pathways can be considered advantageous.[107]

Figure 4.8 demonstrates the effect of increasing the TCA thickness. As initially described R''_{tot} is reduced as the thickness of the TCA layer is lower. The change, however, is not constant with CNT density. The differences in R''_{tot} between large t, Δ_1

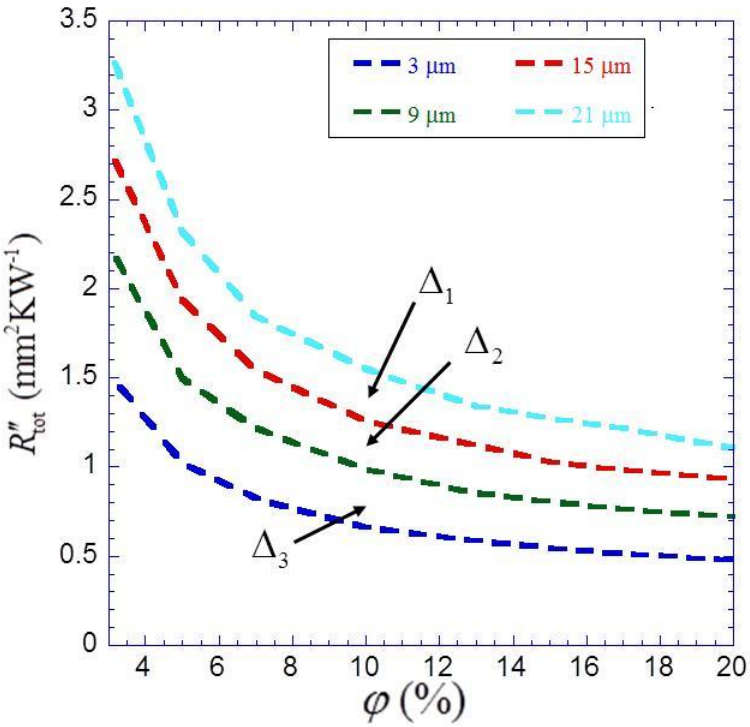

Figure 4.8. R''_{tot} (mm^2 K W^{-1}) across VACNT based TIM for 60% Vol. Ag with $k_{CNT} = 3{,}000$ W m^{-1} K^{-1} Through lines from Fig 4.6(c) showing variation of R''_{tot} at different TCA thicknesses (t)

and Δ_2, and smaller thicknesses, Δ_3 is lower at small thicknesses since the array can penetrate fully through the layer before contacting Ag particles. As φ increases, thereby increasing k_{eff} and reducing the influence of Ag contact it is seen that the R''_{tot} scales nearly linearly with thickness, $\Delta_1 \approx \Delta_2 \approx \Delta_3$

Figure 4.9 shows the impact of a varying intrinsic k_{CNT}. Recently reported values of the intrinsic thermal conductivity for MWCNTs demonstrated that with increased defects the thermal conductivity may be greatly reduced.[108] The impact of the thermal conductivity reduction is particularly evident at lower φ where an over 6 times increase in R''_{tot} is generated. In comparison at low φ the k_{eff} as described by Eqn. (4.8) would be

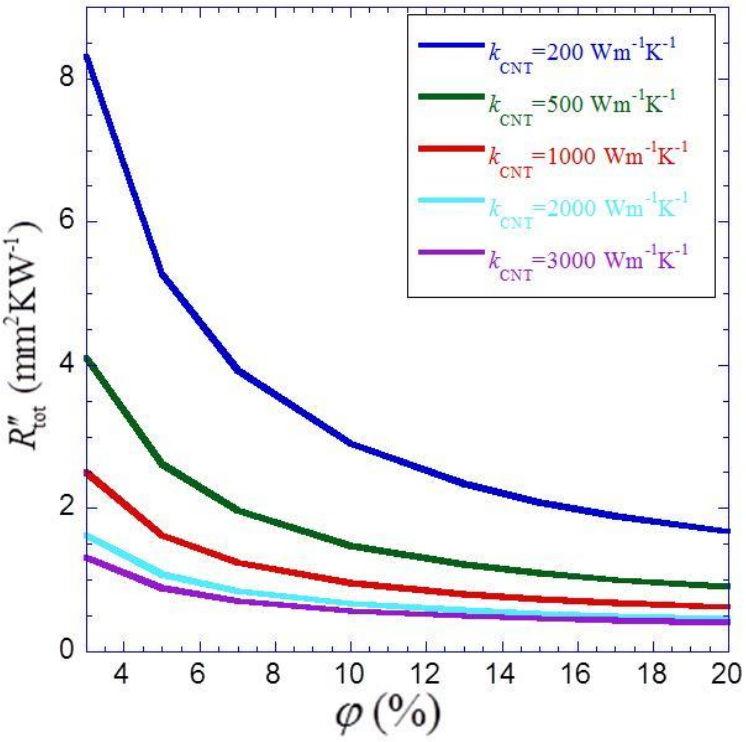

Figure. 4.9. R''_{tot} (mm^2 K W^{-1}) of Si-TCA-CNT-TCA-Cu structure at room temperature at various k_{CNT} (f = 50%, $t = 1.5\,\mu\text{m}$)

expected to be 15 times larger for $k_{\text{CNT}} = 3{,}000$ W m^{-1} K^{-1} than with $k_{\text{CNT}} = 200$ W m^{-1} K^{-1}. This provides a further rationale for the inclusion of highly conductive filler particles described here. If the k_{eff} becomes too low, despite the additional resistance associated with contacting a filler particle, the R''_{tot} which would result from contact would be lower.

4.5 Comparison with Experiments

Figure 3.7(a) shows a representative IR image of a VACNT based TIM material attached using a TCA adhesive. The sample consisted of a 100 μm VACNT array with φ between 5-7%. Difficulty in control over applied TCA thickness assumes that $t > 24$ μm with $f \approx 60\%$. The sample's averaged R''_{tot} over multiple visualized locations was

less than $4\ \text{mm}^2\ \text{K}\ \text{W}^{-1}$. Furthermore, the sample was thermally cycled between -40 – 80 °C 50 times and thermally aged at 150 °C for 300 hrs. resulting in a degradation of less than 5% as measured by the IR system. This sample can be compared to the aforementioned model with perfect contacting interfaces ($t = 24\,\mu\text{m}$, $f = 60\%$, $\varphi = 5\%$, k_{CNT}=3,000 $\text{W m}^{-1}\ \text{K}^{-1}$) whose R''_{tot}=2.56 $\text{mm}^2\ \text{K}\ \text{W}^{-1}$. As seen the value is expectedly lower than the experimental result since perfect interfaces are assumed as well as a uniform CNT density through the TCA layers. Comparing the model with the experiment would show that at an effective individual k_{CNT}=1,000 $\text{W m}^{-1}\ \text{K}^{-1}$, which would account for imperfect contact of the array or increased defects, would result in R''_{tot}=3.92 $\text{mm}^2\ \text{K}\ \text{W}^{-1}$. This would demonstrate that the model can be used to give guidance to improved methods to lower total resistance.

4.6 **Conclusion**

Improved interface materials have a key role in the development of future high power density microelectronic devices. A novel thermal interface material, which takes advantage of the promising thermal properties of VACNT has been theoretically considered, demonstrating potential resistances below $1\ \text{mm}^2\ \text{K}\ \text{W}^{-1}$. The use of a thermal adhesive layer is expected to have the benefit of improving thermal contact between the CNT array and opposing surfaces, as well as assisting in thermal transport at moderate filler concentrations. The best results be seen at low adhesion layer thicknesses as the array can fully penetrate through providing good mechanical support for the array and minimal contacting interfaces. Reduced thermal resistance for thicker samples can still be achieved through increased CNT densification techniques and/or control of filler concentrations. Comparisons with early experimental work on VACNT TIM materials

demonstrates that the model is able to accurately capture expected total thermal resistances and can serve as a tool for future VACNT based TIM development.

CHAPTER 5

TRANSIENT INFRARED MEASUREMENT FOR DETERMINING THERMOPHYISCAL PROPERTIES OF MULTILAYER SAMPLES

In order to further analyze next generation interface materials, a transient IR measurement system was developed. For lower resistance samples there are inherent issues with the steady-state measurement. One of these is that the lower thermal resistance samples require higher heat flux in order to get a substantive temperature gradient through the sample. This can lead to excessive temperatures which were not compatible with the heater. A short duration high heat flux is one solution for this issue. Furthermore additional information of thermal diffusivity of the sample along with thermal interfacial resistances is possible using this technique. Also higher sample throughput may be possible using a transient IR measurement than compared with other steady-state techniques.

Similar to other metrology techniques described in Chapter 2 the thermophysical properties are determined through property extraction using a transient heat conduction model. Unlike the other methods, by sampling at different locations, the transient behavior of each layer can be analyzed individually, providing a more accurate representation of the properties of each layer. The analytic 1-D heat conduction model will be 1st described, followed by the least square property extraction technique. The experimental setup including the use of a high speed transient IR acquisition mode and a lower speed movie mode will then be described. Sensitivity analysis of both techniques will be presented and measurement of VACNT based TIM with the movie mode will be presented.

5.1 Analytical Modeling

For heat conduction problems which are one-dimensional, transient with nonhomogeneous terms which are constant and independent of time, the general solution may be of the form

$$T(x,\theta) = a(x) + b(\theta) + u(x,\theta) \tag{5.1}$$

The functions $a(x)$ and $b(\theta)$ are chosen such that the problem for $u(x,\theta)$ is nonhomogeneous. Problems with time-dependent nonhomogeneous terms required other methods. One of those methods is variation of parameters which is used here, another type of technique is termed Duhamel's theorem. [109] The following will describe the steps involved in the solution of a time dependent multilayer stack which can be analyzed using transient IR imaging. The first step is to set up a problem for each layer with nonhomogeneous terms equal to zero and determining eigenvalues λ_m and eigenfunctions Φ_m. The next step is to construct a solution to the nonhomogeneous problem in the form

$$T_i(x,\theta) = \sum_{m=1}^{\infty} A_{m,i}(\theta)\Phi_{m,i}(x) \tag{5.2}$$

and evaluate $A_{m,i}(\theta)$ through orthogonality Ordinary differential equations are solved by substituting Eqn. (5.2) into the initial problem and can be solved by substituting boundary conditions and initial conditions $A_{m,i}(0)$.

The problem which is considered for determining the thermophysical properties and interfacial conductance of a TIM are shown in Fig. 5.1. A periodic heat flux, $q''(\theta)$, is applied to the leading edge of the 1st layer while on the n^{th} layer a time varying temperature boundary condition is given $T(\theta)$. It is further given that there is imperfect contact (i.e. $-k_i \frac{dT_i(L,\theta)}{dx} = G(T_i(L,\theta) - T_{i+1}(L,\theta))$ where i is the layer in which the transient problem is solved, L is the length of the layer, and G is the interfacial conductance due to imperfect contact between interfaces as well as thermal boundary

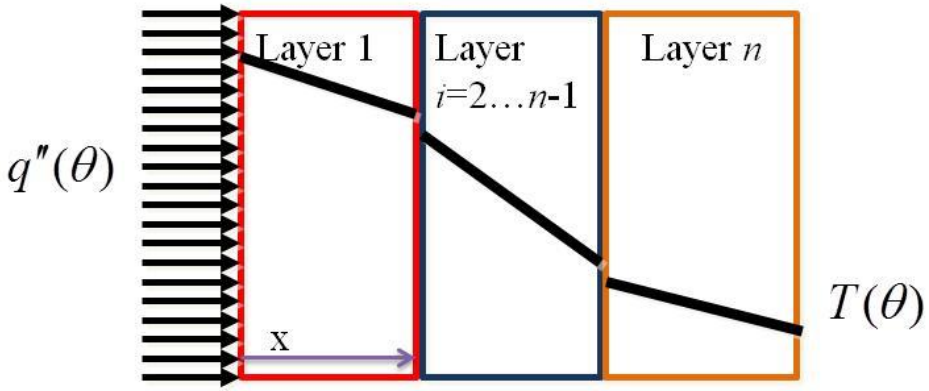

Figure 5.1 Analytical problem for evaluating properties of TIM using transient IR imaging

resistances previously described. Also between the interfaces is a constant heat flux condition, $k_i \frac{dT_i(L,\theta)}{dx} = k_{i+1} \frac{dT_{i+1}(L,\theta)}{dx}$. It is assumed that the initial temperature T_0 condition is thesame through all the layers. Through variation of parameters it can be determined that the solution to the prescribed problem for the 1st layer is of the form [109]

$$T_1(x,\theta) = \sum_{m=1}^{\infty} \left\{ \begin{array}{l} \frac{2\alpha_1}{k_1 L_1} \int_0^{\theta} \left[q^{"}(\tau) \exp(\lambda_m^2 \alpha_1 \tau) \right] d\theta \exp(-\lambda_m^2 \alpha_1 \theta) \\ + \left[\frac{2T_0}{L_1 \lambda_m} \sin(\lambda_m L) \right] \exp(-\lambda_m^2 \alpha_1 \theta) \\ + \frac{2G_1 \alpha_1 \cos(\lambda_m L)}{k_1 L_1} \int_0^{\theta} \left[T_2(0,\tau) \exp(\lambda_m^2 \alpha_1 \tau) \right] d\theta \exp(-\lambda_m^2 \alpha_1 \theta) \end{array} \right\} \frac{\cos(\lambda_m x)(\lambda_m L_1)^2}{2((\lambda_m L_1)^2 + H_1 \cos^2(\lambda_m L_1))} \quad (5.4)$$

Where α_1 is the thermal diffusivity of the 1st layer, $H_1 = G_1 L_1 / k_1$, and, λ_m the series of eigenvalues given by solutions of $\lambda_m L_1 \sin(\lambda_m L_1) - H_1 \cos(\lambda_m L_1) = 0$. The solutions for subsequent layers excluding the final layer are

$$T_i(x,\theta)=\sum_{m=1}^{\infty}\left\{\begin{array}{l}-\dfrac{2\alpha_i k_i}{L_i k_{i-1}}\displaystyle\int_0^{\theta}\left[\frac{\partial T_{i-1}(L_{i-1},\tau)}{\partial x}\exp(\lambda_m^2\alpha_i\tau)\right]d\tau\exp(-\lambda_m^2\alpha_i\theta)\\+\left[\dfrac{2T_0}{L_i\lambda_m}\sin(\lambda_m L_i)\right]\exp(-\lambda_m^2\alpha_i\theta)\\+\dfrac{2G_{i+1}\alpha_i\cos(\lambda_m L_i)}{k_i L_i}\displaystyle\int_0^{\theta}\left[T_{i+1}(0,\tau)\exp(\lambda_m^2\alpha_i\tau)\right]d\tau\exp(-\lambda_m^2\alpha_i\theta)\end{array}\right\}\frac{\cos(\lambda_m x)(\lambda_m L_i)^2}{2((\lambda_m L_i)^2+H_i\cos^2(\lambda_m L_i))} \tag{5.5}$$

For the final layer the solution gives

$$T_n(x,\theta)=\sum_{m=1}^{\infty}\left\{\begin{array}{l}-\dfrac{2\alpha_n k_n}{L_n k_{n-1}}\displaystyle\int_0^{\tau}\left[\frac{dT_{n-1}(0,\tau)}{dx}\exp(\lambda_m^2\alpha_n\tau)\right]d\tau\exp(-\lambda_m^2\alpha_n\tau)\\+\left[\dfrac{2T_0}{L_n\lambda_m}\sin(\lambda_m L_n)-\dfrac{2\alpha_n\lambda_m T_{i+1}(L_n,\theta)}{L_n}\right]\exp(-\lambda_m^2\alpha_n\tau)\\+\dfrac{2\alpha_n\lambda_m T_{i+1}(L_n,\theta)}{L}\sin(\lambda_m L_n)\end{array}\right\}\cos(\lambda_m x) \tag{5.6}$$

where $\lambda_m=(2m-1)\pi/L_n$. As can be seen the solution for each layer is a function of the time dependent temperature profile of the adjacent layers and must be solved iteratively. This procedure is computationally expensive. The analytical method is compared to a test case numerical model using COMSOL for a 3 layer problem which would be expected when analyzing TIM using IR imaging. A comparison between the two models can be seen in Fig. 5.2 for a test case. Not shown is that the analytical model after many iterations begins to converge to the numerical solved solution through COMSOL. Furthermore the numerical model proved to be substantially faster for the simulation. What is important in the analytical solution is that is clearly shows that all thermophysical properties (including k, ρC) for each layer and the G between layers can be extracted through the solution of an inverse heat transfer problem

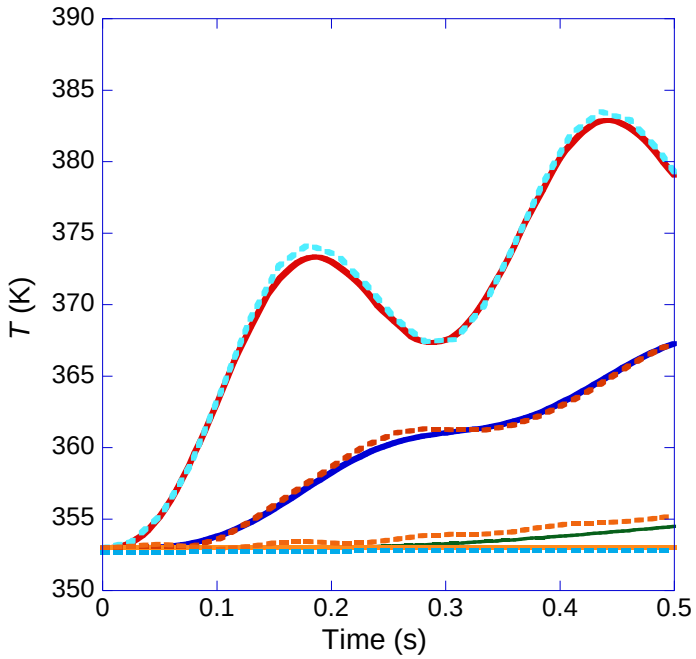

Figure 5.2 3 layer problem consisting of BeO (Layer 1), Al (Layer 2), Cu (Layer 3) each 1cm thick, $q''(\theta) = 200\sin(12t)^2$ W m^{-2} and $T_0 = 80$ °C

5.2 Inverse Heat Transfer Algorithm

While standard heat conduction problems are concerned with finding the temperature distribution along a surface with known boundary conditions, heat generation rates, and thermophysical properties, inverse heat conduction problem aim at determining those given the temperature distribution at one or more locations. This section presents the method for determining thermophysical properties including interfacial conductance from a multilayer sample whose temperature distributions are described by Eqns. (5.4), (5.5), and (5.6). It is in the analysis that the properties do not vary spatially within a given layer.

For the 1-D inverse heat conduction problem for times $\theta > 0$, a known heat rate given by $q''(\theta)$ is applied at surface $x = 0$ while the boundary surface at $x = L$ is defined by $T_0(\theta)$ Temperature measurements using the IR camera are taken at multiple spatial locations $x_i (i = 1, 2, ...N)$ and the temperature readings are taken at times $t_j (j = 1, 2, ...M)$. Therefore a total of $M \times N = \Omega$ temperature measurements are available.

The existence of the inverse solution is guaranteed by requiring that the inverse solution minimizes the least squares norm given as

$$S(p) = \sum_{i=1}^{\Omega} \left[Y_i - T_i(p_j) \right]^2 \tag{5.7}$$

where Y_i is measured temperature, T_i is the estimated temperature obtained from the solution of the heat conduction problem by using the estimated set of properties p_j. Eqn. (5.7) is minimized by differentiating S with respect to each of the unknown parameters and then setting the resulting expression equal to zero such that

$$\frac{\partial S}{\partial p} = 2 \sum_{i=1}^{\Omega} \left(\frac{\partial T_i}{\partial p} \right) \left(T_i(p) - Y_i \right) = 0 \tag{5.8}$$

Here the total number of measurements should be larger than the total number of unknowns. For the IR measurements this is more than sufficient as will be described later. Eqn. (5.8) can be written in matrix form as

$$\frac{\partial S}{\partial \mathrm{p}} = 2\mathrm{X}^T (\mathbf{T} - \mathbf{Y}) = 0 \tag{5.9}$$

where $\mathbf{T}$ is the estimated temperature vector, $\mathbf{Y}$ is the measured temperature vector and $\mathbf{X} = \partial \mathbf{T} / \partial \mathbf{p}^T$ where $\mathbf{p}$ is the properties vector Since the generated system of equations are nonlinear as seen in Eqns. (5.4), (5.5), and (5.6) an iterative technique is used to determine the unknown parameters. A modified Levenberg-Marquardt algorithm is used to solve the nonlinear least squares equations. It uses a combination of the Newton method which converges quickly but requires a good initial guess and the steepest descent method which converges slowly but does not require a good initial guess. The iterative algorithm takes the form

$$\mathbf{p}^{k+1} = \mathbf{p}^k + (\mathbf{J}^T \mathbf{J} + \mu \mathbf{I})^{-1} \mathbf{J}^T (\mathbf{Y} - \mathbf{T}) \tag{5.10}$$

where, μ is a damping parameter which is adjusted higher or lower between iterations as the solution converges, and **J** is the sensitivity coefficient matrix $\mathbf{J} = \partial \mathbf{Y} / \partial \mathbf{p}$. Here k refers to the iteration number.

In order to determine the properties through the algorithm the set of temperature readings at all locations were downloaded as text files and imported to define the matrix $\mathbf{T}$. COMSOL was used to simulate the experiment under a set of **p** in addition to the amplitude of the heat flux, the thickness of each layer, the locations of the measured temperatures, the initial temperature and the backside temperature imported from the last measurement reading location. The output of this COMSOL model was the matrix $\mathbf{Y}$. Define sensitivity matrix, **J**, by varying parameter by a fractional amount to determine the partial derivative of the temperature with respect to a change in a given parameter from the **p** set. A new **p** was found according to Eqn. (5.10) and the procedure was continued until the convergence.

5.3 Measurements of TIM Using Transient IR Imaging

Preliminary samples of were analyzed using a beryllium oxide heater used to generate the pulsed heat input, a commercial thermal grease, and the leading edge of a machined copper water block which raise the temperature of the samples to a reference temperatures and was used as a thermal sink in which the heat is removed. The copper block fixture was placed on the Infrascope II thermal test stage, similar to the configuration in Fig. 3.1. The copper block was further secured to the test stage using a metal vice to reduce undesired motion during the measurement. Insulation was placed around the sample and the backside of the heater to prevent heat loses.

Two separate methods were utilized for acquiring transient data. One of these with an equipped high-speed transient IR detector would capture the thermal response at a single point as a function of time at a rate of up to 50 kHz. The measurement spot sized

Table 5.1 High-speed transient detector spot measurement size

Microscope Objective Lens	Measurement Spot size (μm)
1x	500
5x	100
15x	33

using the high-speed detector with different microscope objective lenses is described in Table 5.1. The second method used the steady-state camera movie mode which takes a series of full temperature mappings, as described in Chapter 3, over time, to form a movie. As can be seen, at the maximum possible resolution with the equipped transient detector has a spot size of 30 μm which can be nearly 1/3 the size of the anticipated TIM layer or greater. Alternatively, the maximum resolution as seen in the steady-state detector shown in Table 3.1 is significantly lower but rate of acquisition for the movie-mode (13 Hz) is slower.

For a series of measurements involving the high speed transient detector, the steady-state detector was first used to focus on a particular measurement location which would be used for data analysis as shown in Fig. 5.3. Furthermore, the length of the layer, which is a required parameter for the property extraction as seen in Eqns. (5.4), (5.5), and (5.6), was determined using the software. From Fig. 5.3, the grease TIM layer is focused on, while the BeO layer and the Cu layers are out of focus. Upon clamping and initial heating portions, of the grease were squeezed out. An average cross-sectional thickness was determined in order to set the thickness of this layer. A benefit of this method over the steady-state method is being able to focus on each layer independently since each point measurement is separate from the others. The high speed transient detector signal acquisition is triggered through an external voltage which is supplied to the oscilloscope

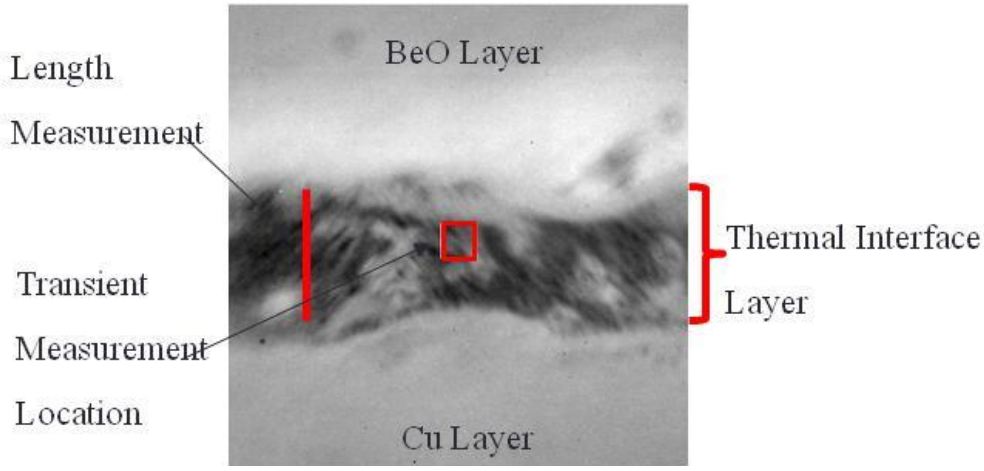

Figure 5.3 Measurement location focusing for high speed transient IR imaging

acquisition card. Therefore, it is possible to sync the camera to the thermal power supplied to the sample. During the data reduction process, each measurement and the applied trigger signal is used to combine all measurement sets for property extraction.

For the measurements using high-speed transient detector, a function generator (Agilent 33250 80 MHz Function/Arbitrary Waveform Generator) was used to trigger a second function generator (Agilent 33250) and the thermal signal acquisition from the detector. The time was set between pulses from the first function generator to allow for heat supplied to be removed through the water block, and to stabilize the sample back to its initial temperature. The temperature of the sample was constantly monitored by thermocouples on the heater and within the copper block. The second function generator was used to generate a periodic heat flux which was amplified using a voltage amplifier (Kepco Bipolar Operational Power Supply/Amplifier). The second function generator's supplied waveform was recorded for data analysis. An oscilloscope (Agilent 54615B Oscilloscope) was used to determine the amplitude of the flux to the heater. The camera software was set to take a total of 10 reading at each location and export the average of those readings for data analysis. This was designed to reduce the uncertainty of the measurement for a single data set. The synced trigger signal and the temperature vs. time data at each point were saved and recalled during data analysis.

Using the high-speed transient detector, a preliminary measurement of a silver loaded grease TIM material was analyzed. A square waveform heat flux with an amplitude 78 $W\,cm^2$ and 500 ms period with 50 % duty cycle was generated for 1 s using the function generator and the power amplifier. Transient images were captured at each measurement location and then the camera was moved to develop the temperature vs. time data set as shown in Fig. 5.4. Two data sets were taken within the BeO layer, three measurements within the grease layer and two data sets recorded within the copper block region. The final data set recorded furthest away from the heat source within the copper area, which is not shown in Fig. 5.4, was used to as the boundary temperature in the property extraction. Precise measurement locations were determined using the steady-state detector.

Using the inverse heat transfer algorithm the data was fit and a best-fit set of material properties were established for the heater and TIM layers. Table 5.2 describes demonstrating good agreement between the measured and reported *k*.

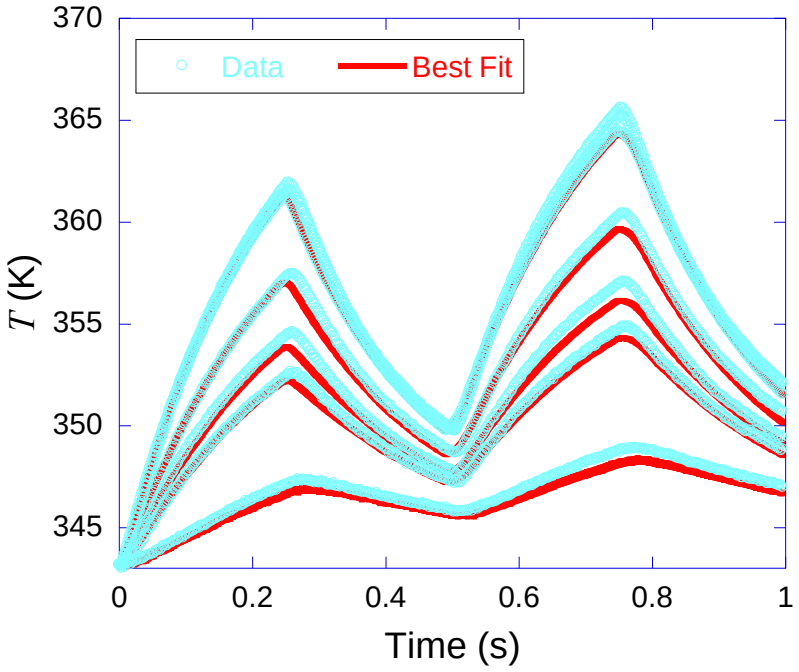

Figure 5.4 High-speed transient measurement and data reduction of silver loaded TIM

Table 5.2 Measured and reported TIM values using high-speed transient detector

	Reported Value	**Measured High-Speed IR Values**
k (W m^{-1} K^{-1})	4.5	3.2
ρC (J m^{-3} K^{-1})	-	6.4×10^{6}
G_1 (W m^{-2} K^{-1})	-	3.7×10^{5}
G_2 (W m^{-2} K^{-1})	-	1.7×10^{5}

For the movie-mode measurement, a LabView code was used to trigger the Agilent 6644A DC Power Supply, used in the steady-state measurements, output on/off for a prescribed period of time. The movie-mode thermal capturing was first initialized and recording before the output of the power supply was initiated. The reference image for the movie-mode capture can be seen in Fig 5.5(a). Unlike the previous measurement using the high speed transient detector, for the measurement using the movie-mode the TIM layer could not be clearly focused as compared to the other two surfaces. This was due to the grease pump out from the interface when the temperature was brought up to a reference value. This further makes the total thickness for the layer difficult to evaluate. Due to this issue a steady-state image in Fig 5.5(b) was used later for comparison to the data extraction rather than commercial reported values

Thermal mappings captured using the movie-mode times can be seen in Fig. 5.6(a)-(i) at given times. A heat flux of 122.5 W cm^{-2} was applied for 8 s during the measurement. The data which was collected can be used to determine the average temperature vs. time histories along the interface. Mappings were recorded each 0.075 s. The last temperature vs. time history which was taken the farthest away from the heating source was taken to be the boundary temperature used in Eqn. (5.6).

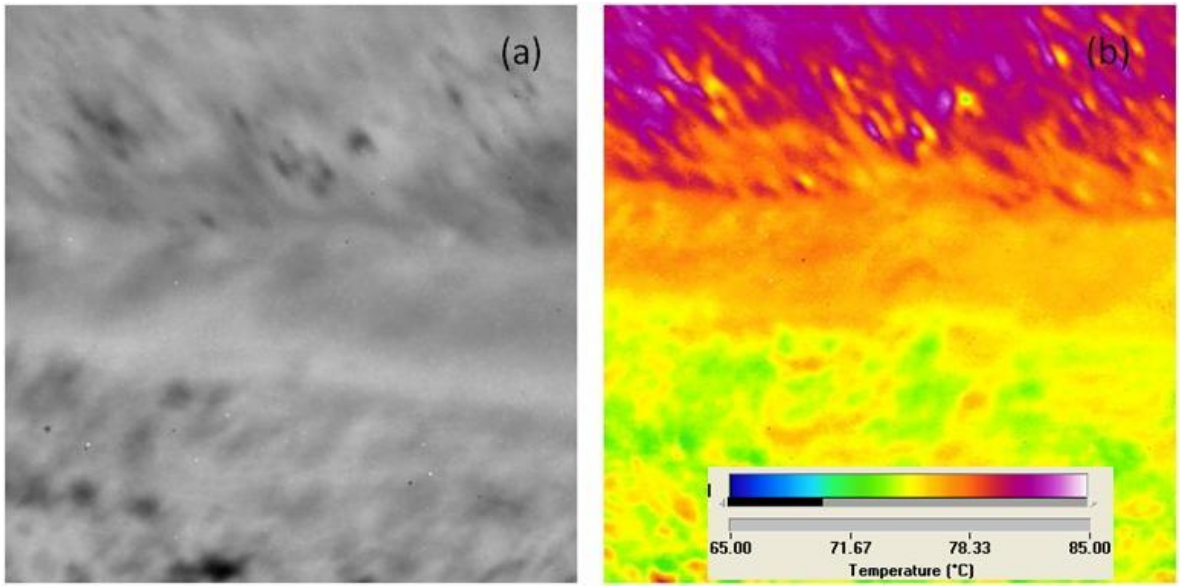

Figure 5.5 (a) Reference measurement of BeO-TIM-Cu interface (b) Corresponding steady-state image at 122.5 W cm^{-2}

For data extractions using the movie-mode averaged pixel temperatures of areas parallel to the interface were exported. Since the movie mode detector acquisition was not synced with the heat flux, the frame before the first notable increase in sample temperature was used as the initial temperature. A benefit of this method, as compared to the high-speed transient technique described earlier is that camera positioning and focus only had to be done a single time as compared to the other measurement.

Table 5.3 describes the extracted k, ρC, G_1 ,and G_2 values along with sum of the component resistances. Also shown is the R''_{tot} from the corresponding steady-state image in Fig. 5.5(b). Since a clear determination of interface thickness was not possible this was determined to be the most suitable comparison. As can be seen there is good agreement between the two R''_{tot} values for the movie-mode and steady-state measurements.

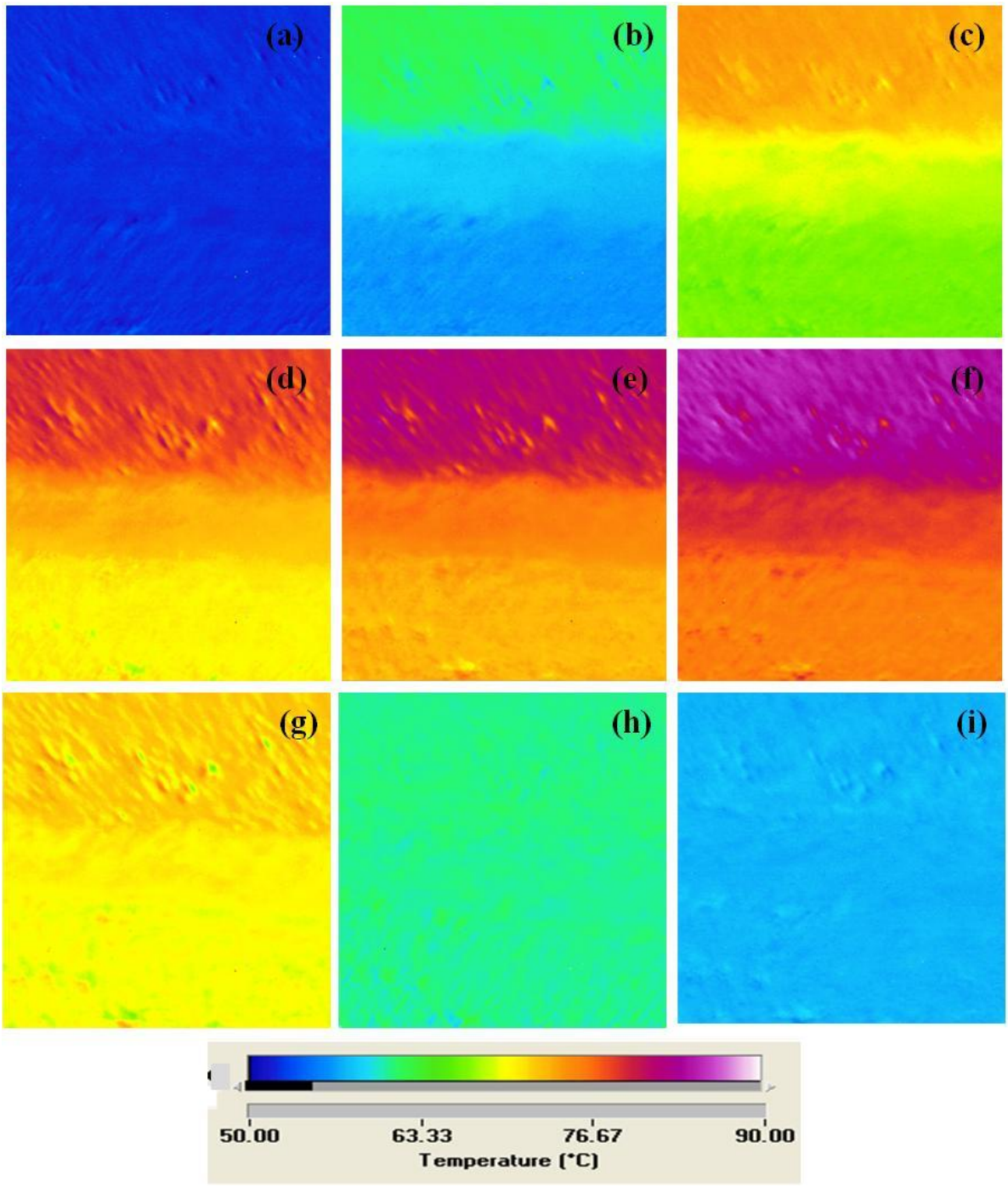

Figure 5.6 Thermal mapping of various times for the measurement of TIM sample. The shown times are at (a) $\theta = 0$ s, (b) $\theta = 0.15$ s, (c) $\theta = 0.67$ s, (d) $\theta = 1.72$ s, (e) $\theta = 4.34$ s (f) $\theta = 8.24$ s, (g) $\theta = 8.47$ s, (h) $\theta = 10.57$ s, (i) $\theta = 13.49$ s

Table 5.3 Measured TIM values using movie-mode transient method and steady-state imaging IR microscopy

	Measured Movie-Mode Values	**Steady-State IR Measured Value**
k ($W\,m^{-1}\,K^{-1}$)	18.5	-
ρC ($J\,m^{-3}\,K^{-1}$)	3.7×10^{6}	-
G_1 ($W\,m^{-2}\,K^{-1}$)	5.0×10^{6}	-
G_2 ($W\,m^{-2}\,K^{-1}$)	4.0×10^{6}	-
R''_{tot} ($mm^2\,K\,W^{-1}$)	6.214	6.5

5.4 Sensitivity Analysis

In order to determine the evaluate the sensitivity of the high-speed, and movie-mode transient measurements, a general set of parameters were adjusted in COMSOL by a percentage difference from their base values to assign a 0.5 ^{o}C window which could be resolved using the high-speed transient and steady-state detectors. Continued development in the sensitivity capabilities of IR detectors would be of great benefit to this method and provide more accurate results. In this sensitivity analysis, 3 layers of different materials were modeled and the parameters including k and ρC of each layer and the interlayer contact conductance were defined. The same layer thickness, amplitudes, and heat fluxes which were used in preliminary measurements described in Section 5.3 were used here for the respective sensitivity analysis. The measurement locations used in the sensitivity analysis were based on the high-speed transient detector spots. A significant benefit of the movie-mode is the full temperature mapping whose data extraction points can be assessed separately from the initial measurements. The base values used in the sensitivity analysis are shown in Table 5.4

Table 5.4 Materials base values used in transient IR microscopy sensitivity analysis

	k ($\mathrm{W\,m^{-1}\,K^{-1}}$)	ρC **x 10^6** ($\mathrm{J\,m^{-3}\,K^{-1}}$)
Layer 1	265	3.14
Layer 2	4.5	2.5
Layer 3	401	3.43
$G_1 = G_2 = 1\times10^6$ $\mathrm{W\,mm^2\,K^{-1}}$		

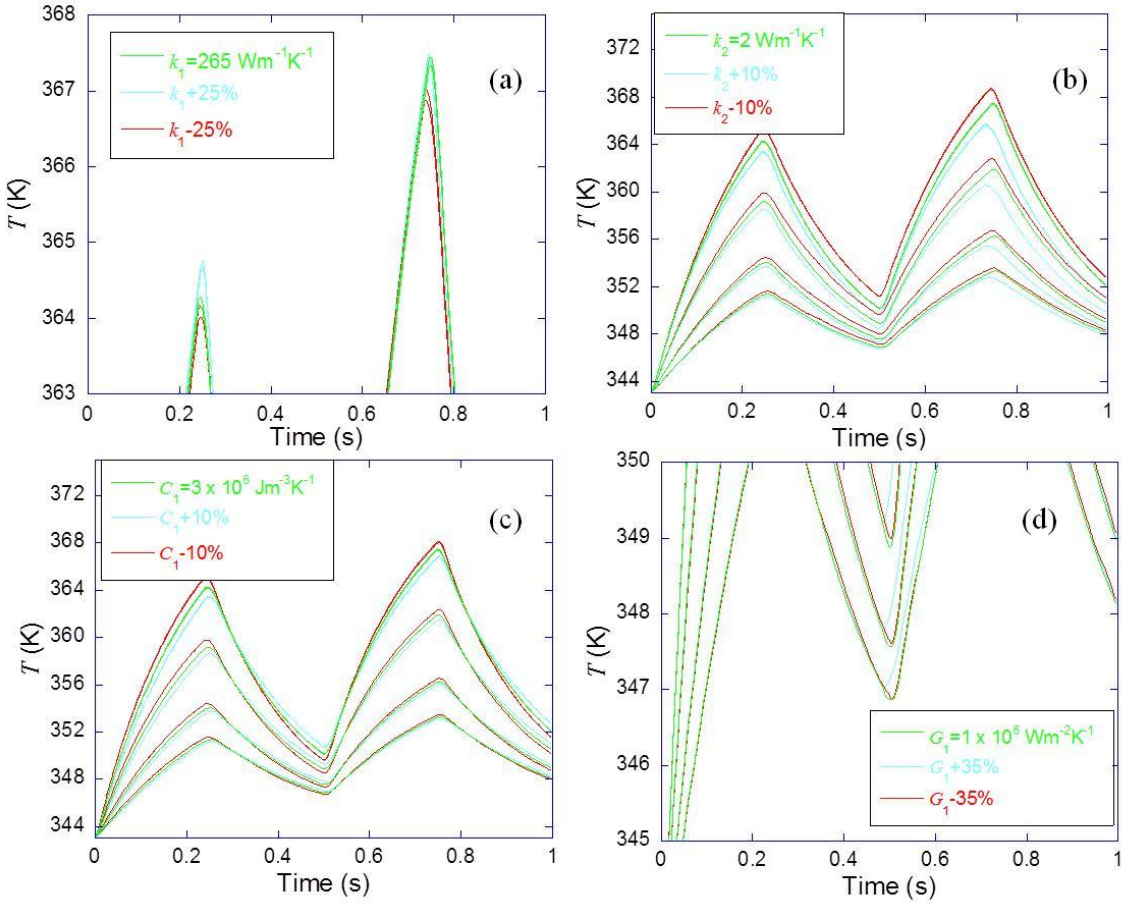

-

Figure 5.7 Sensitivity analysis of data collection using high-speed transient detector (a) Change in Layer 1 k (b) Change in Layer 2 k (c) Change in Layer 1 ρC (d) Change in interfacial resistance between Layers 1 and 2.

Figure 5.7 shows sensitivity analysis for the simulated high-speed measurements. Figure 5.7(a) shows that for a minimum temperature sensitivity of 0.5°C a *k* value of $265 \pm 25\%$ W m^{-1} K^{-1} would be assigned to the material in Layer 1 through the inverse heat transfer algorithm. The *k* resolution is greatly improved for lower base *k* values as seen in Fig. 5.7(b). This would make this measurement suitable for various TIM materials, including particle laden greases. Figure 5.7(c) shows that the ρC can be resolved with high sensitivity for the high-speed transient measurement by capturing the initial temperature rise and decay with the applied periodic heat flux. Accurate determination of interfacial conductance is difficult to ascertain using this measurement with the applied heat flux as shown in Fig 5.7(d).

The same sensitivity analysis is performed with the movie-mode measurement based on an 8 s measurement with a 122.5 W cm^{-2} heat flux amplitude. Figure 5.8(a) shows that the *k* for a highly conductive material as Layer 1 can be extracted to within 20% of the final value. With larger heat flux amplitude or with additional measurement distance separation this value may be lower but does demonstrate the benefit of increased time acquisition as compared to the high-speed detector which can only record within a 1 s interval. This method is particularly beneficial when there is a limit to the amplitude of the applied heat flux. The resolution is also better with materials which are less conducting as indicated in Fig. 5.8(b). However, the high-speed transient detector also effectively measures low conductive materials and may be preferable with a higher rate of acquisition leading to more data points to be fit and reducing uncertainty. The movie-mode can be used to extract ρC by fitting the initial temperature rise data as shown in Fig. 5.8(c). However, as stated previously, more data during this time period can be captured using the high-speed detector to reduce uncertainty. Additional heating periods can also be captured using the movie-mode to improve the accuracy of the extracted results. Figure 5.8(d) demonstrates that due to the increased heating period available

with the movie-mode, more accuracy can be provided on interfacial conductance than with the high-speed measurement. This is of great benefit in the continued assessment of VACNT interfaces which may be either bonded or non-bonded.

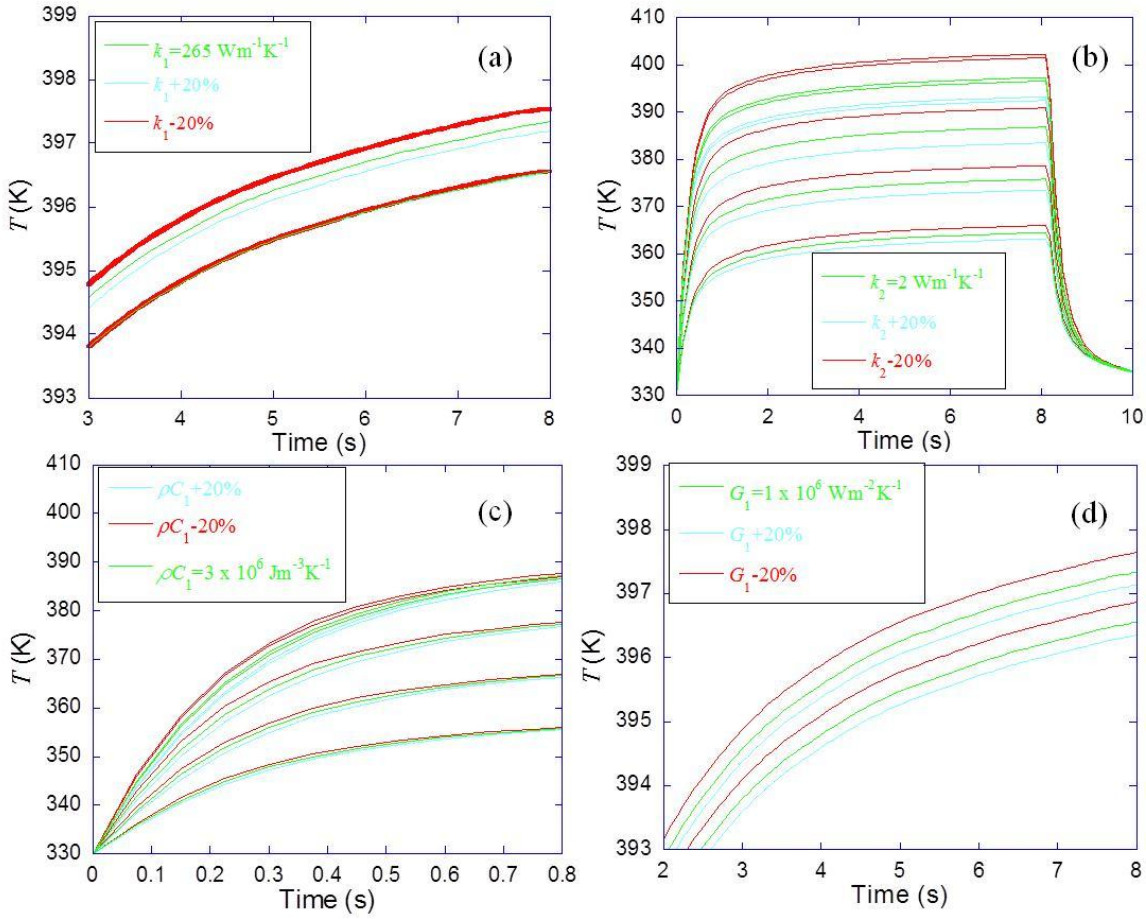

Figure 5.8 Sensitivity analysis of data collection movie-mode transient measurement detector (a) Change in Layer 1 k (b) Change in Layer 2 k (c) Change in Layer 1 ρC (d) Change in interfacial resistance between Layers 1 and 2.

5.5 Transient IR Measurements of VACNT TIM

A VACNT sample was imaged using the movie-mode to analyze the transient behavior through the VACNT array in order to determine the intrinsic conductivities of the effective VACNT layer and the interface resistance for the same samples that are previously described in Chapter 3. As discussed, it can be difficult to determine the precise location of the interface during measurement using this transient method. Before sample characterization, the total thickness of the VACNT interface was measured (157 μm) using an optical microscope. This total thickness includes the anchoring TCA layers. The nominal growth thickness of the VACNT array was 100 μm and was removed and attached using TCA adhesion layers as described earlier. The complete sandwich structure was Cu-TCA-CNT-TCA-Si.

A heat flux (122 $W\ m^{-2}$) was applied to the Cu side for 10.2 seconds while the IR microscope was capturing thermal mapping at a rate of 13 Hz. Figure 5.9 shows the reduced data and the set based on the extracted parameters with Fig. 5.9(b) showing a zoomed in time scale of the captured data. As shown qualitatively there is significant separation between the Cu and TCA-CNT interface indicating a large interfacial resistance at this point. For the ideal scenario as described in Chapter 4 where the array is in end contact with the substrates the *G* would be expected to be at least an order of lower at the Cu interface than the Si interface due necessary electron-phonon coupling within the metal. Also shown is the best-fit curve for the data. Table 5.5 shows the extracted data of the properties from the measurement. As expected the *G* between the Cu and TCA-VACNT is significantly lower than that for the Si interface.

Table 5.5 Extracted properties of VANCT based TIM using transient IR microscopy

	Measured Movie-Mode Values
k (W m^{-1} K^{-1})	35
ρC (J m^{-3} K^{-1})	9.8×10^{6}
G_1 (W m^{-2} K^{-1})	2.4×10^{5}
G_2 (W m^{-2} K^{-1})	8.9×10^{6}

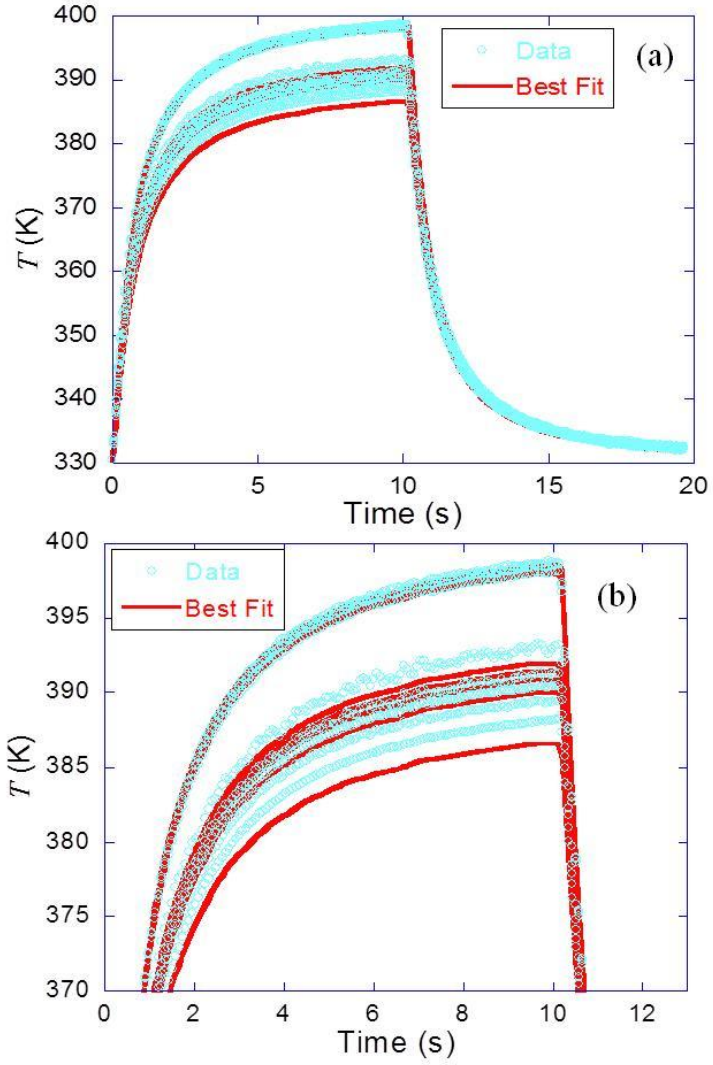

Figure 5.9 (a) Full Movie-mode measurement of a VACNT based TIM and the best-fit of the measurement. (b) The movie-mode data 1 and 11 s and the best-fit measurement

The extracted value of the k for the interface layer of $35\ \mathrm{W\,m^{-1}\,K^{-1}}$ is near the same value for solder based TIM materials. The R''_{tot} of the material based on the component resistance is $8.8\ \mathrm{mm^2\,K\,W^{-1}}$ with a large portion of that resistance being due to the boundary resistance at the Cu interface $4.1\ \mathrm{mm^2\,K\,W^{-1}}$.

5.6 Conclusion

This chapter has described the development of a novel TIM measurement system based on transient IR imaging. The development of the analytical model describing a multilayer heat conduction problem consisting of time dependent boundary conditions demonstrates that material properties including thermal conductivity and heat capacity of a material can be independently determined in addition to interfacial thermal resistances. These component resistances can be summed to determine total thermal resistance previously described. An inverse heat transfer algorithm, as the one described here, can then be used following data collection to determine material properties.

Two separate transient IR imaging techniques have been described here. One is through the use of a high-speed transient detector and the other is through a series of temperature mappings made through a lower speed detector. Both methods have benefits including precise thickness imaging of each layer through independent focusing using the high speed detector or preferential full field imaging with the ability to view transient behavior in real-time. Measurements have been presented on a commercial material with data agreeing with that of reported value for the high-speed measurement and component resistance as measured using the movie-mode imaging method consistent with the R''_{tot} made through IR steady-state microscopy.

The movie-mode transient IR measurement method has been further extended to analyze a VACNT based TIM with the array anchored using a TCA. Since it was unclear where the VACNT/TCA region or exposed VACNT regions where full structure was

group and the effective properties total layer was analyzed. The extracted thermal conductivity places the material on the same order of commercially available solder TIM attachments.

CHAPTER 6

CONCLUSIONS AND RECOMMENDATIONS

This thesis has described experimental and theoretical work as describing the thermal behavior of VACNT CNT based TIM. These CNT with high cross-plane thermal conductivity have great potential in future electronics cooling applications Due to their high growth temperatures VACNT arrays studied here have been removed from their growth substrates and anchored through thermal conductive adhesive attachments and solders. The thermal performance of the tubes as characterized through a steady-state IR measurement system is comparable and better than currently available TIM alternatives with measured thermal resistance being less than 4 mm^2 K W^{-1} . The steady-state IR measurement system described was validated by measuring commercial TIM products with measured resistance values being comparable to those reported by the vendor. Long term thermal resilience issues through cycling and aging tests of the VACNT based TIM demonstrates little deterioration when anchored used conductive adhesive.

A parametric study of one of the attractive VACNT anchoring techniques was conducted through the analysis of the TCA attachment. The control-volume model included parameters which can be adjusted in order to determine potential thermal performance. As explained in the model development there is further potential to reduce the overall thermal resistance below 1 mm^2 K W^{-1} which would be highly desirable for high-performance electronic packages. The initial framework presented here can be extended by designers in the development of future VACNT based TIMs.

Finally a novel transient measurement technique has been described here, which provides additional insight into the thermophysical properties as compared to steady-state measurement methods. Measurements presented demonstrate potential use with either a high-speed transient detector capability or a lower speed full-mapping capability. Finally

a transient measurement of a VANCT based TIM demonstrated high intrinsic thermal conductivity value which is of particular interest in future applications.

6.1 Original Contribution

The work has described the extension of a IR steady-state measurement beyond which has been previously reported in the analysis of VACNT based TIM. The approach has been further verified through the use of commercial samples. The meticulous material selection of appropriate anchoring materials in conjunction with VACNT arrays has lead to a novel TIM material has potential for future commercial application. The contributions will assist in the future development of VACNT TIM and TIM metrology.

The development of a new TIM model based on ideal interfaces whose interface conductance is due solely to acoustic mismatch or mismatched electronic properties can be used to assess the quality of TIM interfaces. The model described here further demonstrates that continued improvements using the VACNT are possible and are reason for continued research.

Additionally, the original transient IR imaging method presented here is new tool in thermal characterization. The system provides improved benefits over other methods including the ability to assess materials in a more timely fashion and with more detail. An optimized data reduction algorithm can provide real time analysis into TIM behavior.

6.2 Recommendations for Future Work

This work has demonstrated the potential use of VACNT arrays as TIM but significant research work beyond the scope presented here can still be accomplished. For VACNT TIM development, significant research can still focus on optimized anchoring materials. These materials would need to fully bond to the VACNT array and have similar vibration behavior with the mating array and substrate. It would also be critical that the anchoring materials themselves would not deteriorate after long term use.

Recently research into phonon coupling materials is of particular interest and should be further investigated. Additionally, once the correct material is presented precise control over anchoring material application including thickness and bonding strength can greatly improve thermal performance as shown here.

The design and assembly challenges for VACNT TIM are complemented by those in thermal characterization of these multi-scale materials. While the smallest sizes of interest are in the nm range, the layer thickness and other dimensions may be on the order of mm or cm. Continuum based modeling, coupled with underlying atomistic modeling will continue to be developed to provide insight into VACNT and other nanostructured TIM thermal properties. Further developments into atomistic modeling can be used to evaluate the boundary resistances of newer materials, which may be used to mate VACNT to other substrates. Modeling should also be extended to time dependent behavior to analyze performance degradation of TIM during harsh operating conditions.

Thermal characterization techniques will continue to be developed which can accurately and rapidly determine the total thermal resistance of these materials. Measurement standards for low thermal resistance samples, on the order of $1\ mm^2\ K\ W^{-1}$ would provide more confidence in interpreting results. Standards should include sample size, attachment pressure and measurement temperature, and repeatability. Furthermore, since the materials will be expected to withstand harsher operating conditions than current TIM, extensive experiments are needed that prove TIM reliability through their entire use.

Additional work into microscopic IR metrology improvements would be of great interest. These devices are of increased use in research and industry environments. Detectors with a well defined response to small temperature variations would be of benefit not only in TIM studies described here but in broader electronic cooling

applications. Improved spatial resolution capabilities would be of benefit in failure analysis and TIM reliability studies as a result of thermal stresses.

Development of the transient IR technique described would be well worth continuing. As presented, the multilayer thermal property extraction procedure is straight-forward and could be developed into a software script and a full automated system for real-time analysis. A precision controller for preset measurement locations would be recommended for a repeatable set of measurements. An auto-focusing enabled microscope would greatly reduce the time associated with the measurement. Both measurement techniques described previously show potential in fully characterizing multilayer materials. A hybrid-method which would provide significant amounts of reducible data in the early times as described in the high-speed transient method would give better resolution into materials heat capacity. A longer capturing period and higher applied heat flux as described would provide better insight into materials with large thermal conductivity. Furthermore, the ability to capture full-field images is recommended to ensure uniformity and would be of importance in assessing full TIM engagement in thermal transport.

REFERENCES

[1] "The International Technology Roadmap for Semiconductors," San Jose, CA: Semiconductor Industry Association, See Also URL http://www.itrs.net/.

[2] Prasher, R., 2006, "Thermal Interface Materials: Historical Perspective, Status, and Future Directions," Proceedings of the IEEE, **94**, pp. 1571-1586.

[3] McNamara, A. J., Joshi, Y., Zhang, Z. M., 2012, "Characterization of Nanostructured Thermal Interface Materials A Review," International Journal of Thermal Sciences, **62**, pp 2-11.

[4] Yang, J., Waltermire, S., Chen, Y., Zinn, A. A., Xu, T.T., Li, D., 2010 "Contact thermal Resistance Between Individual Multiwall Carbon Nanotubes," Applied Physics Letters, **96**, pp. 023109.

[5] Shenogin, S., Xue, L., Ozisik, R., Keblinski, P., and Cahill, D. G., 2004, "Role of Thermal Boundary Resistance on the Heat Flow in Carbon-Nanotube Composites," Journal of Applied Physics, **95**, pp. 8136-8144.

[6] Chung, D., 2001, "Thermal Interface Materials," Journal of Materials Engineering and Performance, **10**, pp. 56-59.

[7] Xu, J., and Fisher, T. S., 2006, "Enhancement of Thermal Interface Materials with Carbon Nanotube Arrays," International Journal of Heat and Mass Transfer, **49**, pp. 1658-1666.

[8] Samson, E.C., Machiroutu, S.V., Chang, J.Y., Santos, I., Hermerding, J., Dani, A., Prasher, R., Song, D.W., 2005, "Interface Material Selection and a Thermal Management Technique in Second-Generation Platforms Built on Intel Centrino Mobile Technology," Intel Technology Journal, **9**, pp. 75-86.

[9] Kim, P., Shi, L., Majumdar, A., and Mceuen, P., 2001, "Thermal Transport Measurements of Individual Multiwalled Nanotubes," Physical Review Letters, **87**, pp. 215502.

[10] Hu, X. J., Padilla, A. A., Xu, J., Fisher, T. S., and Goodson, K. E., 2006, "3-Omega Measurements of Vertically Oriented Carbon Nanotubes on Silicon," Journal of Heat Transfer, **128**, pp. 1109-1113.

[11] Zhou, W., Qi, S., Tu, C., Zhao, H., Wang, C., Kou, J., 2007, "Effect of the Particle Size of Al2O3 on the Properties of Filled Heat Conductive Silicone Rubber," Journal of Applied Polymer Science, **104**, pp. 1312-1318.

[12] Zhu, B., Ma, J., Wu, J., Yung, K., Xie, C., 2010, "Study on the Properties of the Epoxy Matrix Composites Filled with Thermally Conductive AlN and BN Ceramic Particles," Journal of Applied Polymer Science, **118**, pp. 2754-2764.

[13] Zhou, W., Qi, S., Zhao, H., Liu, N., 2007, "Thermally Conductive Silicone Rubber Reinforced with Boron Nitride Particle," Polymer Composites, **28**, pp. 23-28.

[14] Putnam, S., Cahill, D., Ash, B., Schadler, L., 2009, "High-Precision Thermal Conductivity Measurements as a Probe of Polymer/Nanoparticle Interfaces," Journal of Applied Physics, **94**, pp. 6785-6788.

[15] Kochetov, R., Andritsch, T., Lafont, U., Morshuis, P., Picken, S., Smit, J., 2009, "Thermal Behaviour of Epoxy Resin Filled with High Thermal Conductivity Nanopowders," IEEE Electrical Insulation Conferece, pp. 524-528.

[16] Tang, C., Bando, Y., Liu, C., Fan, S., Zhang, J., Ding, X., Golberg, D., 2006, "Thermal Conductivity of Nanostructured Boron Nitride Materials," Journal of Physical Chemistry B, **110**, pp. 10354-10357.

[17] Iijima, S., 1991, "Helical Microtubules of Ggraphitic Carbon," Nature, **354**, pp. 56-58.

[18] Wong, C.P., Moon, K.S., Li Y., Eds., 2009, *Nano-Bio Electronic, Photonic and MEMS Packaging*, Springer.

[19] Zhang, Z. M., 2007, *Nano/Microscale Heat Transfer*, McGraw-Hill, New York.

[20] Dresselhaus, M., Dresselhaus, G., Saito, R., 1995, "Physics of Carbon Nanotubes," Carbon, **33**, pp. 883-891.

[21] Treacy, M. M. J., Ebbesen, T. W., Gibson, J., 1996, "Exceptionally High Young's Modulus Observed for Individual Carbon Nanotubes," Nature, **381**, pp. 678-680.

[22] Krishnan, A., Dujardin, E., Ebbesen, T. W., Yianilos P., Treacy M. M. J., 1998, "Young's Modulus of Single-Walled Nanotubes," Physical Review B, **58**, pp 14013.

[23] Wong, E. W., Sheehan, P. E., Lieber, C. M., 1997, "Nanobeam Mechanics: Elasticity, Strength, and Toughness of Nanorods and Nanotubes, **277**, pp. 1971-1975.

[24] Yu, M. F., Lourie, O., Dyer, M. J., Moloni, K., Kelly, T. F., Ruoff, R. S., 2000, "Strength and Breaking Mechanism of Multiwalled Carbon Nanotubes Under Tensile Load, Science, **287**, pp. 637-640.

[25] Won, Y., Gao, Y., Panzer, M. A., Dogbe, S., Pan, L., Kenny, T. W., Goodson, K. E., 2012, "Mechanical Characterization of Aligned Multi-Walled Carbon Nanotube Films Using Microfabricated Resonators," Carbon, **50**, pp. 347-355.

[26] Ginga, N. J., Sitaraman, S. K., 2012, "The Experimental Measurement of Effective Compressive Modulus of Carbon Nanotube Forests and the Nature of Deformation," Carbon, **53**, pp. 237-244.

[27] Incropera, F. P., Dewitt, D. P., 2002, *Fundamentals of Heat and Mass Transfer*, 5th ed., John Wiley & Sons, Inc., Hoboken.

[28] Choi, T.-Y., Poulikakos, D., Tharian, J., Sennhauser, U., 2006, "Measurement of the Thermal Conductivity of Individual Carbon Nanotubes by the Four-Point Three-ω Method," Nano letters, **6**, pp. 1589-1593.

[29] Hone, J., Whitney, M., Piskoti, C., Zettl, A., 1999, "Thermal Conductivity of Single-Walled Carbon Nanotubes," Physical Review B, **59**, pp. R2514-R2516.

[30] Balandin, A. A., 2011, "Thermal Properties of Graphene and Nanostructured Carbon Materials," Nature Materials, **10**, pp. 569-581.

[31] Dresselhaus, M. S., and Eklund, P. C., 2000, "Phonons in Carbon Nanotubes," Advances in Physics, **49**, pp. 705-814.

[32] Mingo, N., and Broido, D., 2005, "Carbon Nanotube Ballistic Thermal Conductance and Its Limits," Physical Review Letters, **95**, pp. 096105.

[33] Marconnet, A. M., Panzer, M. A., Goodson, K. E., 2013, "Thermal Conduction Phenomena in Carbon Nanotubes and Related Nanostructured Materials," Reviews of Modern Physics, **85**, pp. 1295-1326.

[34] Prasher, R., 2008, "Thermal Boundary Resistance and Thermal Conductivity of Multiwalled Carbon Nanotubes," Physical Review B, **77**, pp. 075424.

[35] Prasher R., 2007, "Thermal Conductance of Single-Walled Carbon Nanotube Embedded in an Elastic Half-Space," Applied Physics Letters, **90**, pp. 143110.

[36] Yu, C., Shi, L., Yao, Z., Li, D., and Majumdar, A., 2005, "Thermal Conductance and Thermopower of an Individual Single-Wall Carbon Nanotube," Nano Letters, **5**, pp. 1842-1846.

[37] Pop, E., Mann, D., Wang, Q., Goodson, K. E., and Dai, H., 2006, "Thermal Conductance of an Individual Single-Wall Carbon Nanotube above Room Temperature," Nano Letters, **6**, pp. 96-100.

[38] Choi, T. Y., Poulikakos, D., Tharian, J., Sennhauser, U., 2005, "Measurement of Thermal Conductivity of Individual Multiwalled Carbon Nanotubes by the 3-ω Method," Applied Physics Letters, **87**, pp. 013108.

[39] Wang, Z. L., Tang, D. W., Li, X. B., Zheng, X. H., Zhang, W. G., Zheng, L. X., Zhu, Y. T., Jin, A. Z., Yang, H. F., Gu, C. Z., 2007, "Length-Dependent Thermal Conductivity of an Individual Single-Wall Carbon Nanotube, Applied Physics Letters, **91**, pp. 123119.

[40] Diao, J., Srivastava, D., and Menon, M., 2008, "Molecular Dynamics Simulations of Carbon Nanotube/Silicon Interfacial Thermal Conductance," The Journal of Chemical Physics, **128**, pp. 164708.

[41] Gao, F., Qu, J., and Yao, M., 2011, "Interfacial Thermal Resistance between Metallic Carbon Nanotube and Cu Substrate," Journal of Applied Physics, **110**, pp. 124314.

[42] Ebbesen T., Ajayan P., 1992, "Large-Scale Synthesis of Carbon Nanotubes," Nature, **358**, pp. 220-222.

[43] Bethune D., Klang C., De Vries M., Gorman G., Savoy R., Vazquez J., Beyers R., 1993, "Cobalt-Catalysed Growth of Carbon Nanotubes with Single-Atomic-Layer Walls," Nature, **363**, pp. 605-607.

[44] Thess, A., Lee, R., Nikolaev, P., Dai, H., Petit, P., Robert, J., Xu, C., Lee, Y. H., Kim, S. G., Rinzler, A. G., 1996, "Crystalline Ropes of Metallic Carbon Nanotubes," Science, **273**, pp 483-487.

[45] Hafner, J. H., Bronikowski, M. J., Azamian, B. R., Nikolaev, P., Rinzler, A. G., Colbert, D. T., Smith, K. A., Smalley, R. E., "Catalytic Growth of Single-Wall Carbon Nanotubes from Metal Particles," Chemical Physics Letters, **296**, pp. 195-202.

[46] Biercuk, M., Llaguno, M. C., Radosavljevic, M., Hyun, J., Johnson, A. T., and Fischer, J. E., 2002, "Carbon Nanotube Composites for Thermal Management," Applied Physics Letters, **80**, pp. 2767-2769.

[47] Huxtable, S. T., Cahill, D. G., Shenogin, S., Xue, L., Ozisik, R., Barone, P., Usrey, M., Strano, M. S., Siddons, G., and Shim, M., 2003, "Interfacial Heat Flow in Carbon Nanotube Suspensions," Nature Materials, **2**, pp. 731-734.

[48] Choi, E., Brooks, J., Eaton, D., Al-Haik, M., Hussaini, M., Garmestani, H., Li, D., and Dahmen, K., 2003, "Enhancement of Thermal and Electrical Properties of Carbon Nanotube Polymer Composites by Magnetic Field Processing," Journal of Applied Physics, **94**, pp. 6034-6039.

[49] Marconnet, A. M., Yamamoto, N., Panzer, M. A., Wardle, B. L., and Goodson, K. E., 2011, "Thermal Conduction in Aligned Carbon Nanotube-Polymer Nanocomposites with High Packing Density," ACS Nano, **5,** pp. 4818-4825.

[50] Lin, W., Moon, K. S., and Wong, C. P., 2009, "A Combined Process of in Situ Functionalization and Microwave Treatment to Achieve Ultrasmall Thermal Expansion of Aligned Carbon Nanotube–Polymer Nanocomposites: Toward Applications as Thermal Interface Materials," Advanced Materials, **21**, pp. 2421-2424.

[51] Cola, B. A., Xu, J., and Fisher, T. S., 2009, "Contact Mechanics and Thermal Conductance of Carbon Nanotube Array Interfaces," International Journal of Heat and Mass Transfer, **52**, pp. 3490-3503.

[52] Lin W., Xiu Y., Jiang H., Zhang R., Hildreth O., Moon K. S., Wong C. P., 2008, "Self-Assembled Monolayer-Assisted Chemical Transfer of In Situ Functionalized Carbon Nanotubes," Journal of the American Chemical Society, **130**, pp. 9636-9637.

[53] Lin, W., Zhang, R., Moon, K. S., Wong, C. P., 2010 "Molecular Phonon Couplers at Carbon Nanotube/Substrate Interface to Enhance Interfacial Thermal Transport, Carbon, **48**, pp. 107-113.

[54] Cross, R., Cola, B. A., Fisher, T., Xu, X., Gall, K., and Graham, S., 2010, "A Metallization and Bonding Approach for High Performance Carbon Nanotube Thermal Interface Materials," Nanotechnology, **21**, pp. 445705.

[55] Tong, T., Zhao, Y., Delzeit, L., Kashani, A., Meyyappan, M., and Majumdar, A., 2007, "Dense Vertically Aligned Multiwalled Carbon Nanotube Arrays as Thermal Interface Materials," IEEE Transactions on Components and Packaging Technologies, **30**, pp. 92-100.

[56] Cola, B. A., Xu, J., Cheng, C., Xu, X., Fisher, T. S., and Hu, H., 2007, "Photoacoustic Characterization of Carbon Nanotube Array Thermal Interfaces," Journal of Applied Physics, **101**, pp. 054313.

[57] Xu, Y., Zhang, Y., Suhir, E., Wang, X., 2006, "Thermal Properties of Carbon Nanotube Array Used for Integrated Circuit Cooling, Journal of Applied Physics, **100**, pp. 074302.

[58] Prasher R., 2005, "Predicting the Thermal Resistance of Nanosized Constrictions," Nano Letters, **5**, pp, 2155-2159.

[59] Swartz, E., and Pohl, R., 1989, "Thermal Boundary Resistance," Reviews of Modern Physics, **61**, pp. 605-668.

[60] Duda, J. C., Hopkins, P. E., Beechem, T. E., Smoyer, J. L., and Norris, P. M., 2010, "Inelastic Phonon Interactions at Solid-Graphite Interfaces," Superlattices and Microstructures, **47**, pp. 550-555.

[61] Panzer, M. A., Duong, H. M., Okawa, J., Shiomi, J., Wardle, B. L., Maruyama, S., Goodson, K. E., 2010, "Temperature-Dependent Phonon Conduction and Nanotube Engagement in Metalized Single Wall Carbon Nanotube Films," Nano Letters, **10**, pp. 2395-2400.

[62] Berber, S., Kwon, Y., Tomanek D., 2000, "Unusually High Thermal Conductivity of Carbon Nanotubes," Physical Review Letters, **84** pp. 4613-4616.

[63] Che, J., Cagin, T., William, III, A. G., "Thermal Conductivity of Carbon Nanotubes," Nanotechnology, **11**, pp. 65-69.

[64] Cao A., Qu J., Yao M., 2010, "Atomistic Simulations of Heat Transfer at Carbon Nanotube/Si interfaces, IEEE Electronics Componenets and Technology Conference, pp. 417-420.

[65] ASTM D5470-01: Standard Test Method for Thermal Transmission Properties of Thin Thermally Conductive Solid Electrical Insulation Materials, ASTM International, 2001, pp. 1-5.

[66] Zhang, K., Chai, Y., Yuen, M., Xiao, D., Chan, P., 2008, "Carbon Nanotube Thermal Interface Material for High-Brightness Light-Emitting-Diode Cooling," Nanotechnology, **19**, pp. 215706.

[67] Parker, W. J., Jenkins, R. J., Butler, C. P., Abbottm G. L., 1961, "Flash Method of Determining Thermal Diffusivity, Heat Capacity, and Thermal Conductivity," Journal of Applied Physics, **32**, pp. 1679-1685.

[68] Cape, J., and Lehman, G., 1963, "Temperature and Finite Pulse-Time Effects in the Flash Method for Measuring Thermal Diffusivity," Journal of Applied Physics, **34**, pp. 1909-1913.

[69] Lin, W., and Wong, C., 2010, "Vertically Aligned Carbon Nanotubes for Thermal Interface Materials: Quality Control, Alignment Improvement and Laser Flash Measurement," IEEE Electronics Componenets and Technology Conference, Las Vegas, 2010, pp. 967-972.

[70] Lin, W., Shang, J., Gu, W., Wong, C. P., 2012, "Parametric Study of Intrinsic Thermal Transport in Vertically Aligned Multi-Walled Carbon Nanotubes Using a Laser Flash Technique, Carbon, **50**, pp. 1591-1603.

[71] Amama, P. B., Cola, B. A., Sands, T. D., Xu, X., and Fisher, T. S., 2007, "Dendrimer-Assisted Controlled Growth of Carbon Nanotubes for Enhanced Thermal Interface Conductance," Nanotechnology, **18**, pp. 385303.

[72] Cola, B. A., Hodson, S. L., Xu, X., and Fisher, T. S., 2008, "Carbon Nanotube Array Thermal Interfaces Enhanced with Paraffin Wax," ASME 2008 Heat Transfer Summer Conference.

[73] Cahill, D. G., 1990, "Thermal Conductivity Measurement from 30 to 750 K: The 3ω Method," Review of Scientific Instruments, **61**, pp. 802-808.

[74] Qiu, T., Grigoropoulos, C., Tien, C., 1993, "Novel Technique for Noncontact and Microscale Temperature Measurements," Experimental Heat Transfer, **6**, pp 231-241.

[75] Lee A., Norris P., "A New Optical Method for Measuring Surface Temperature at Large Incident Probe Angles," Review of Scientific Instruments, **68**, pp. 1307-1311.

[76] Zhang Z. M., Tsai, B. K., Machin, G., Eds., 2009, *Radiometric Temperature Measurements: I. Fundamentals*, Academic Press.

[77] Panzer, M. A,, Zhang, G., Mann, D., Hu, X., Pop, E., Dai, H., Goodson, K. E., 2008, "Thermal Properties of Metal-Coated Vertically Aligned Single-Wall Nanotube Arrays," Journal of Heat Transfer, **130**, pp. 052401.

[78] Hu, X. J., Panzer, M. A., and Goodson, K. E., 2007, "Infrared Microscopy Thermal Characterization of Opposing Carbon Nanotube Arrays," Journal of Heat Transfer, **129**, pp. 91-93.

[79] Lin, Z., Yao, Y., McNamara, A. J., Moon, K. S., Wong C. P., 2012, Single/Few-Layer Boron Nitride-Based Nanocomposites for High Thermal Conductivity Underfills, IEEE Electronic Components and Technology Conference, pp. 1437-1441.

[80] Childs P. R., 2001, *Practical Temperature Measurement*, Butterworth-Heinemann.

[81] Modest M. F., 1993, *Radiative Heat Transfer*, McGraw-Hill, New York.

[82] Oxley C. H., Hopper R. H., Hill G., Evans G. A., 2010, "Improved Infrared (IR) Microscope Measurements and Theory for the Micro-Electronics Industry," Solid-State Electronics, **54**, pp. 63-66.

[83] InfraScope User's Manual, Quantum Focus Instruments Corp, Vista, Ca, 2005.

[84] Agilent Technologies, 2006, 6644A 200 Watt System Power Supply User Manual.

[85] The Bergquist Company, 2007, Hi-Flow 225UT Technical Data Sheet.

[86] Henkel Technologies, 2002, Loctite Silverstrate Technical Data Sheet.

[87] Ablestik, 2007, Abletherm 3188 Technical Data Sheet.

[88] Nan, C. W., Liu, G., Lin, Y., and Li, M., 2004, "Interface Effect on Thermal Conductivity of Carbon Nanotube Composites," Applied Physics Letters, **85**, pp. 3549-3551.

[89] Deng, F., Zheng, Q. S., Wang, L. F., and Nan, C. W., 2007, "Effects of Anisotropy, Aspect Ratio, and Nonstraightness of Carbon Nanotubes on Thermal Conductivity of Carbon Nanotube Composites," Applied Physics Letters, **90**, pp. 021914.

[90] Nan, C. W., Shi, Z., Lin, Y., 2003, "A Simple Model for Thermal Conductivity of Carbon Nanotube Based Composites," Chemical Physics Letters, **375** (2003) 666-669.

[91] Tao, T., Yang, Z., Delzeit, L., Kashani, A., Meyyappan, M., Majumdar, A., 2007, "Dense Vertically Aligned Multiwalled Carbon Nanotube Arrays as Thermal Interface Materials," IEEE Transactions on Components and Packaging Technologies, **30**, pp. 92-100.

[92] Too, S. S., Touzelbaev, M., Khan, M., Master, R., Diep, J., Kee-Hean, K., 2009 "Indium Thermal Interface Material Development for Microprocessors," IEEE Semiconductor Thermal Measurement and Management Symposium, pp. 186-192.

[93] Barako M. T., Yuan G., Marconnet A. M., Asheghi M., Goodson K. E., 2012, "Solder-Bonded Carbon Nanotube Thermal Interface Materials," IEEE Intersociety Conference on Thermal and Thermomechanical Phenomena in Electronic Systems, pp. 1225-1233.

[94] Jorio A., Saito R., Hafner J., Lieber C., Hunter M., McClure T., Dresselhaus G., Dresselhaus M., 2001, "Structural (n, m) Determination of Isolated Single-Wall Carbon Nanotubes by Resonant Raman Scattering," Physical Review Letters, **86**, pp. 1118-1121.

[95] Dresselhaus M. S., Jorio A., Hofmann M., Dresselhaus G., Saito R., 2010, "Perspectives on Carbon Nanotubes and Graphene Raman Spectroscopy," Nano letters, **10**, pp. 751-758.

[96] Yao Y., Tey J. N., Jun, W., Bennett, K., McNamara, A. J., Joshi, Y. K., Tan, R., Lin, S., Wong, C. P., 2013, "High Quality Vertically Aligned Carbon Nanotubes for Applications as Thermal Interface Materials," Submitted to Carbon..

[97] Lin W., Olivares R. V., Liang Q., Zhang R., Moon K. S., Wong C. P., 2009, "Vertically Aligned Carbon Nanotubes on Copper Substrates for Applications as Thermal Interface Materials: From Synthesis to Assembly, IEEE Electronic Components and Technology Conference, pp. 441-447.

[98] Xu J., Fisher T. S., 2006, "Enhanced Thermal Contact Conductance Using Carbon Nanotube Array Interfaces," IEEE Transactions on Components and Packaging Technologies, **29**, pp. 261-267.

[99] Xu Y., Zhang Y., Suhir E., Wang X., 2006, "Thermal Properties of Carbon Nanotube Array used for Integrated Circuit Cooling," Journal of Applied Physics, **100**, pp. 074302.

[100] Cola B. A., Amama P. B., Xu X., Fisher T. S., 2008, "Effects of Growth Temperature on Carbon Nanotube Array Thermal Interfaces," Journal of Heat Transfer, **130**, pp. 114503.

[101] Ivanov I., Puretzky A., Eres G., Wang H., Pan Z., Cui H., Jin R., Howe J., Geohegan D. B., 2006, "Fast and Highly Anisotropic Thermal Transport Through Vertically Aligned Carbon Nanotube Arrays," Applied Physics Letters, **89**, pp. 223110.

[102] Patankar, S., 1980, *Numerical Heat Transfer and Fluid Flow*, Taylor & Francis.

[103] Xue, Q. Z., 2006, "Model for the Effective Thermal Condcutivity of Carbon Nanotube Composites," Nanotechnology, **17**, pp. 1655-1660.

[104] Majumdar, A., Reddy, P., 2004, "Role of Electron–Phonon Coupling in Thermal Conductance of Metal–Nonmetal Interfaces," Applied Physics Letters, **84**, pp. 4768-4770.

[105] Nicklow, R., Wakabayashi, N., Smith, H. G., 1972, "Lattice Dynamics of Pyrolytic Graphite," Physical Review B, **5**, pp. 4951–4962.

[106] Gundrum, B. C., Cahill, D. G., Averback R. S., 2005, "Thermal Conductance of Metal-Metal Interfaces," Physical Review B, **72**, pp. 245426.

[107] Liu, X., Zhang, Y., Cassell, A. M., Cruden, B. A., 2008, "Implications of Catalyst Control for Carbon Nanotube Based Thermal Interface Materials, Journal of Applied Physics, **104**, pp. 084310.

[108] Pettes, M. T., Shi, L., 2009, "Thermal and Structural Characterizations of Individual Single-, Double-, and Multi-Walled Carbon Nanotubes," Advanced Functional Materials, **19**, pp. 3918-3925.

[109] Myers G.E., 1998, *Analytical Methods in Conduction Heat Transfer*, 2nd Ed., AMCHT Publications, Madison.